Fumed Silica Based Self-Propelling Anisometric Patchy Particles: Preparation, Modification and Motion Analyses

vorgelegt von

M. Sc.

Hatice Esra Oğuztürk

an der Fakultät II - Mathematik und Naturwissenschaften

der Technischen Universität Berlin

zur Erlangung des akademischen Grades

Doktor der Naturwissenschaften

- Dr. rer. nat. -

genehmigte Dissertation

Promotionsausschuss:

Vorsitzender: Prof. Dr. Reinhard Schomäcker
(Technische Universität Berlin)

Gutachter: Prof. Dr. Michael Gradzielski
(Technische Universität Berlin)

Gutachter: Prof. Dr. Joachim Koetz
(Universität Potsdam)

Gutachter: INVISTA-Prof. Dr. Orlin D. Velev
(North Carolina State University)

Tag der wissenschaftlichen Aussprache: 21. Januar 2021

Berlin 2021

To my beloved parents Emine & Mustafa Kemal Oğuztürk,

ACKNOWLEDGEMENTS

I would like to express my deepest gratitude to my supervisors Prof Dr Michael Gradzielski from Technishe Universität Berlin and Prof Dr Orlin D. Velev from North Carolina State University for their endless guidance, support and encouragement.

In addition to my supervisors, I have to thank to all members of Stranski Laboratorium at TU Berlin and Velev Group in NCSU. It was a great experience for me to take part in both groups and meeting these nice people during my PhD voyage. More specifically, I would like to thank to Petra Erdmann, Maria Blüth and Beatrix Thiele, Monika Noji, Dr. Rene Straßnick, Jana Lutzki and Michaela Dzionara for their helps and supports with smiling faces always. I wish to thank to NCSU University Program Associate Maria Moreno and NCSU MRSEC Business Services Coordinator Amy Alexander for being super helpful and kind during all my stays in NCSU.

I am deeply grateful to Astrid Müller-Klauke (Schomäcker Group TU Berlin) for ICP measurements; M.Sc. Leona Bauer and Dr. Ioanna Mantouvalou (Kanngießer Group TU Berlin) for their significant and valuable contributions to my PhD studies with countless CMXRF measurements and discussions.

I would like to thank my dear friends, Züleyha Yenice Campbell, Özge Azeri, Benjamin von Lospichl, Sabina Islam, Hakan Bildirir, Hakan Kaygusuz, Dikran Kesal, Ciğdem Yesildağ, Rahima Rahman, Onur Özdemir, Chunning Sun (special thanks for yummy Chinese meals you cooked for me and letting me to be auntie of your little princess) and Sangchul Roh who always helped me to improve myself, had time for a coffee break whenever I felt stuck and also shared their experiences. In addition to my dear friends, I am also grateful to Hasan Özmen and his family for their endless supports.

Dr Marius Rutkevicius, thank you for being not only a colleague but also a good friend. Thank you for caring about me both at work and outside during all my stays in NCSU.

I would like to acknowledge to Prof Dr Bhuvnesh Barthi from LSU for his suggestions and mentorship while I was struggling with the trajectories of the particles. His ideas were always lightening new bulbs in my mind.

I thank Tomas Omasta for performing supraparticle preparation on 90˚ bent superhydrophobic surfaces.

My precious thanks go to my dear family, my parents Emine & Mustafa Kemal Oğuztürk and my brother Murat Oğuztürk for their endless supports, love and understanding. I could not handle my last 5 years in abroad without their encouragements. Thanks to my dear husband Alper Çuhadar for being my biggest motivation while writing my thesis. Thank you for believing in me, encouraging always, not complaining about my bouncing between two countries and of course loving me as I am.

ABSTRACT

This work compromises the preparation of FS-based anisometric supraparticles, improvement and modification of these supraparticles to obtain patchy particles with the aim of producing self-propelling particles and the motion analysis of the self-propulsion studies.

The starting point was to obtain fumed silica (FS) based anisometric supraparticles. With the addition of electrolyte to the FS-based colloidal mixture it was possible to obtain anisometric supraparticles. To do that, FS dispersions were mixed with NaCl and 3µl droplets of the colloidal mixture were employed on superhydrophobic surfaces to produce anisometric supraparticles via EISA (Evaporation induced self-assembly) method. The effect of ionic strength was examined by varying the NaCl concentration and to see the effect of the specific surface area of the FS, 3 different FS types with 90, 200 and 300 m^2 / g were used.

In addition to NaCl, other electrolytes / additives and their influence on the drying kinetics of the FS-based particles were also examined. NaF, PEG and spermine were the additives used here.

In the second part of this work, Fe_3O_4@Pt catalyst was incorporated into the anisometric supraparticles to obtain patchy particles. By knowing the fact that H_2O_2 decomposition is a metal catalyzed reaction, our goal was to obtain a system in which particles are self-propelling via bubble propulsion mechanism. Pt catalyst embedded patchy particles worked as microswimmers in the presence of the fuel, H_2O_2. The main obstacle here was the mechanical stability of the particles. Therefore, with different modification techniques including hydrophobization agent, heat treatment and additives; 4 classes of particles were produced.

Third part consists of the detailed analysis of the outcome obtained from self-propulsion studies. Trajectories of the particles were analyzed and correlated with the composition of the relevant supraparticles.

Zusammenfassung

Diese Studie befasst sich mit der Herstellung von FS-basierten anisometrischen Suprapartikeln, der Verbesserung und Modifikation solcher anisometrischer Suprapartikel mit dem Ziel der Herstellung von Partikeln mit Domänen sowie der autonomen Bewegung solcher Partikel und der Analyse dieser Bewegungsprozesse.

Der Ausgangspunkt hier war die Herstellung von anisometrischen Suprapartikeln auf der Basis von Fumed Silica (FS). Durch den Zusatz von Elektrolyt zur FS-basierten kolloidalen Mischung war es möglich anisometrische Suprapartikel zu erhalten. Für diesen Zweck wurden FS Dispersionen mit NaCl versetzt und 3 µl Tropfen der kolloidalen Mischung wurden auf superhydrophoben Oberflächen durch Eintrocknung in Suprapartikel überführt (EISA: Evaporation induced self-assembly). Der Effekt der Ionenstärke wurde durch Variation der NaCl Konzentration untersucht und auch der Effekt der spezifischen Oberfläches des FS, wobei hier 3 unterschiedliche FS Typen mit 90, 200 und 300 m^2/g untersucht wurden.

Neben NaCl, wurden auch andere Elektrolyte/Additive und ihr Einfluss auf die Trocknungskinetik der FS-basierten Partikel untersucht. Hier wurden NaF, PEG und Spermine untersucht.

Im zweiten Teil dieser Arbeit wurde Fe_3O_4@Pt Katalysatornanopartikel in anisometrische Suprapartikel eingebaut mit dem Ziel, hier „patchy particles“ zu erhalten. Der Pt-katalysierte H_2O_2 Zerfall und die daraus resultierende Bildung von Sauerstoffblasen ist eine Möglichkeit autonome Bewegung bei Suprapartiklen zu initiieren. Dabei wurde H_2O_2 als Treibstoff gewählt und Suprapartikel mit integriertem Pt Katalysator wurden als Mikroschwimmer untersucht. Geeignete Suprapartikel wurden hergestellt, hatten aber das Problem limitierter mechanischer Stabilität. Aus diesem Grunde wurden 4 Klassen von modifizierten Partikeln hergestellt, bei denen Hydrophobisierungsagens, Heizbehandlung und Additive systematisch variiert wurden.

Im dritten Teil wurde eine detaillierte Analyse der autonomen Bewegung der unterschiedliche Suprapartikel durchgeführt. Die Bewegungsgmuster wurden analysiert und mit der Zusammensetzung der betreffenden Suprapartikel korreliert.

List of Abbreviations

IUPAC:	International Union of Pure and Applied Chemistry
DLVO:	Derjaguin, Landau, Verwey, and Overbeek
UV-VIS:	Ultraviolet-Visible Spectroscopy
JP:	Janus Particles
SEP:	Seeded Emulsion Polymerization
OM:	Optical Microscopy
NA:	Numerical Aperture
EM:	Electron Microscopy
SEM:	Scanning Electron Microscopy
EDS:	Energy Dispersive Spectroscopy
TEM:	Transmission electron Microscopy
XRF:	X-Ray Fluorescence Spectroscopy
CMXRF:	Confocal Micro X-Ray Fluorescence Spectroscopy
CA:	Contact Angle
ECD:	Electrochemical Deposition
FS:	Fumed Silica
EISA:	Evaporation Induced Self Assembly
MFC:	Microfibrillated Cellulose
PS:	Polystyrene
ICP-OES:	Inductively Coupled Plasma Optical Emission Spectrometry

SAED: Selected Area Electron Diffraction

CVD: Chemical Vapor Deposition

Table of Contents

CHAPTER 1: GENERAL INTRODUCTION

1.1 Colloids

The word colloid originally comes from the Greek word "kolla" meaning glue. Colloid systems have been existing since centuries but the first observations were made by Juncher and Macquer in 1774 by defining colloidal systems of gold particles as 'extremely finely divided gold in a fluid'[1]; and continued with Selmi who spent the first sentences in 1845 by describing pseudosolutions[2]. Faraday followed him by investigating the optical properties of gold sol having ~3nm radius in 1857[3]. In 1861, Thomas Graham took part in the field by conducting the rate of diffusion experiments and he was the first person using the word "colloid" to define Selmi's pseudosolution[4]. Graham divided the solutions into two kinds: solutions in which dissolved species can diffuse through the membrane and solutions without and diffusion observed. Graham mentioned that colloids do not diffuse as dissolved species are larger than the pores of the membrane[1].

Then, based on IUPAC definitions, the term colloid was defined as a dispersion composed of molecules or particles having at least one dimension between 1 nm and 100 µm[5]. Based on the size scale of colloids, microscopic methods are suitable for investigations of the colloidal systems. A size scale is drawn in the figure below with some examples from nature to clarify where the colloids stand among other structures in the universe (Figure 1.1).

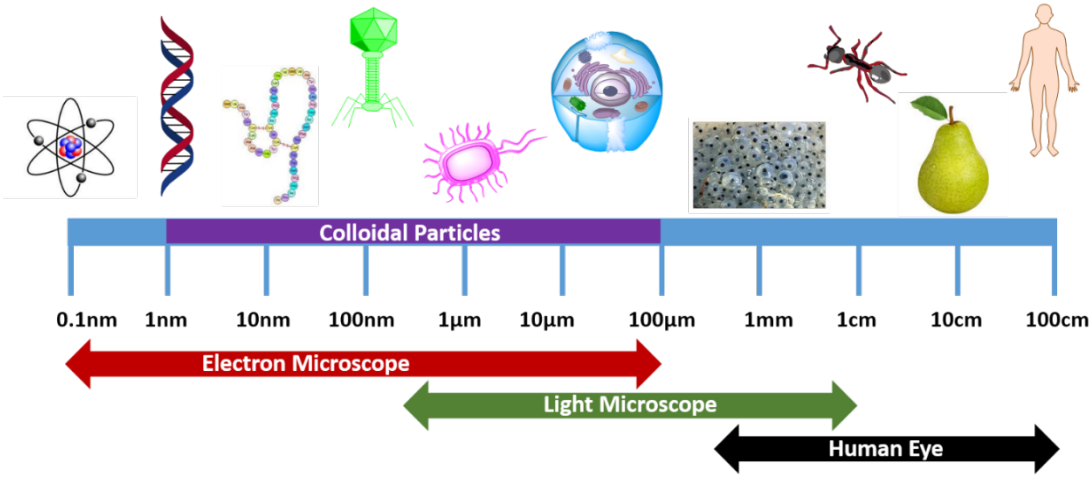

Figure 1.1: Sizes and characterization methods at all scales-from atom to human

Colloidal systems “an intermediate class of materials between bulk and molecularly dispersed systems”[6] consist of two phases, called dispersed (internal) phase and continuous (external) phase. The system is named based on the states of matter used as internal and external phases; however, the most common combinations are composed of solid or liquid particles dispersed in a liquid medium[7] (see Figure 1.2).

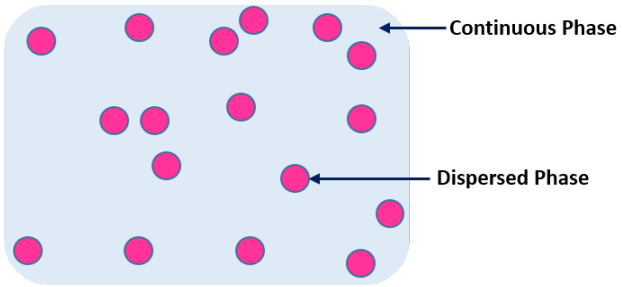

Figure 1.2: Schematic illustration of a colloidal system

Colloidal systems are homogeneous mixtures but not solutions; therefore, they are not stable in time[8]. The stability of the colloids depends on both nature of the dispersion medium and nature of the colloid. For a colloidal system to be stable, electrical properties and sizes of colloids, play the most important role. By characterizing the stability with the interaction energy of the particles, DLVO theory well-defines the stability of colloidal systems[7–9]. Gravitational effects are negligible for colloidal particles as they are so small and light particles. Due to very small size, colloidal particles have high surface areas, which enables them to be used in many application areas (see Table 1.1).

Table 1.1: Nomenclature and some examples of different type of colloidal systems

Internal Phase	External Phase	Name of the System	Examples
Solid	Solid	Solid Sol	Porcelain, Alloy
Solid	Liquid	Sol	Ink, Toothpaste, Starch
Solid	Gas	Solid Aerosol	Inhalers
Liquid	Solid	Gel	Cheese, Pearl, Opal
Liquid	Liquid	Emulsion	Milk, Cream
Liquid	Gas	Liquid Aerosol	Fog, Spray, Mist
Gas	Solid	Solid Foam	Styrofoam
Gas	Liquid	Foam	Fire extinguisher
Gas	Gas	Unknown	-

1.2 Colloidal Stability

In general, a stable colloidal system is desirable for many applications. However, in some cases, such as waste-water treatment, flocculation-opposite of stability- could be very useful. For the potential application areas of the colloidal system, determination of the stability/flocculating properties of the system has the key responsibility and the most common techniques for determination could be listed as UV-VIS spectroscopy, turbidimetry, dynamic light scattering, zeta potential and density measurements. Talking about the stability, 4 main types could be named for the colloidal systems: kinetic, thermodynamic, electrostatic and steric (depletion). Controlling the stability or flocculation properties is ensured with the addition of surfactants or polymers by changing the interphase properties (see Figure 1.3 & 1.4)[12].

DLVO theory[9,10] mentioned in the previous section, defines the stability with the interaction energies of the particles in the system[11]. Stabilization methods compromise steric, electrostatic and depletion stabilization. In steric and electrostatic stabilization, polymer is attached to the surface of the particle, whereas, in depletion stabilization, polymer is not adsorbed on the solid particles. In electrostatic stabilization, an ionic polymer is used, while in steric stabilization the polymer adsorbed on the surface does not carry any electrostatic charge[12]. Additionally, depletion stabilization is achieved with free polymer chains by decreasing the attraction between the particles as a result of their placement between the solid particles[13].

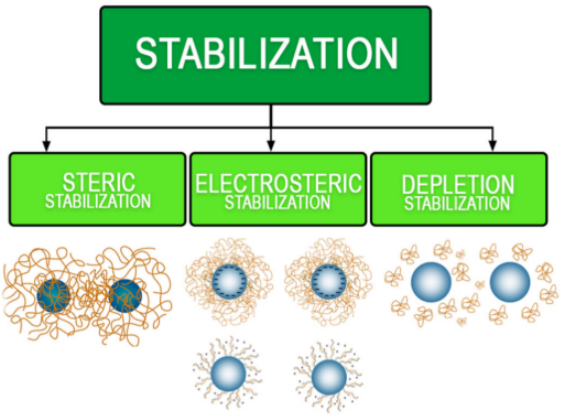

Figure 1.3: Stabilization mechanisms with the addition of polymer. Reproduced from ref [12].

As mentioned before, addition of macromolecules may stabilize or destabilize/flocculate the system. Two main mechanisms of flocculation occur with the polymer addition to the colloidal systems: bridging flocculation and depletion flocculation. Bridging flocculation is observed when two or more colloidal particles are linked with the polymer chains adsorbed on the solid surface. Depletion flocculation occurs with the aggregation of solid particles due to the unadsorbed macromolecules surrounding[13].

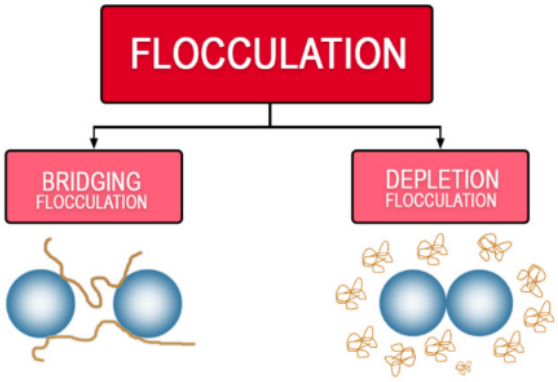

Figure 1.4: Flocculation mechanisms with the addition of polymer. Reproduced from ref [12]

1.3 Janus Particles

Janus particles, in other words patchy particles, is a hot topic for the last few decades. The interest on Janus particles has been increasing year by year (see Figure 1.6). The word "Janus" stems from an ancient Roman God-Janus. This God has two faces one looking at past and one looking at the future at the same time. Janus particles are named after The Roman God; as both the particles and the God represent a unique structure having two opposite sides. In principle, Janus particles are anisotropic colloids containing two incompatible parts in the same structure[14,15]. This incompatibility could be obtained by either giving them shape-wise or composition-wise asymmetry. In the figure below, there are some schematically drawn particles to show different types of asymmetry as examples in the figure below.

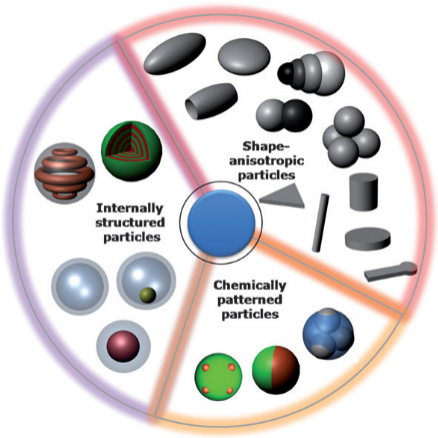

Figure 1.5: Schematic diagram of shape-asymmetric and composition-asymmetric colloidal particles. Reproduced from ref [16]

As it is seen in the Figure 1.5 and mentioned before, Janus particles could be either shape, or composition-wise anisometric. Additionally, hybrid particles in which both shape and composition anisometry are shown, have been attracting the interest of scientists.

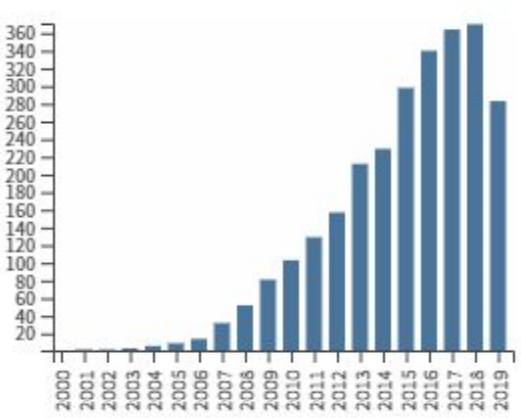

Figure 1.6: Statistics of published items on "Janus Particles" between 2000-2019 (access: 08.10.2019) [retrieved from web of knowledge[17]]

"Janus particle" as a term, universalized by de Gennes[18] after the study "Janus Beads"[19]: Realization and Behavior at Water/Oil Interfaces was published from his research group.

Janus particles can be classified with respect to different parameters like content, shape etc. They could be composed of polymeric, inorganic, organic-inorganic, and polymeric-inorganic materials[20–22]. Based on the morphology, Janus particles may be sphere, rod, cylindrical, disk-like, dumbbell-like, snowman-like, acorn-like, and raspberry-like[21,23].

Janus particles have wide variety of application areas including biologic[24] (sensing and isolation, drug delivery, nano surgery, imaging), nano- / micro-motors[24,25] and catalysis[25] etc.

1.3.1 Janus Particle Synthesis Methods

There are several methods used to synthesize or prepare Janus particles reported in literature. Depending on the purpose of usage, materials and procedure limitations, different methods could be used. The main 3 methods can be named as self-assembly, masking and phase separation of a heterogeneous mixture (see Figure 1.7)[26,27]. In addition to these 3 main methods, seeded polymerization (nucleation process) and emulsion solvent evaporation method (pickering emulsion) are the other preferred techniques depending on the system.

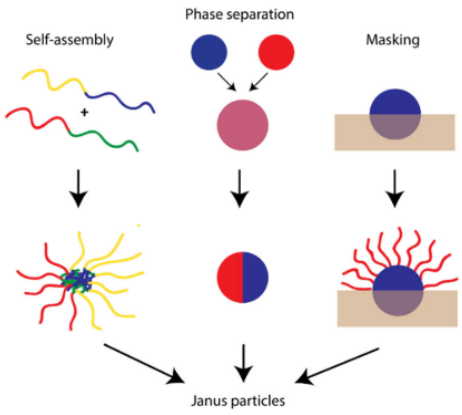

Figure 1.7: Schematic illustration of three main pathways for Janus particle preparation. Reproduced from ref [27]

1.3.1.1 Self-Assembly of Block copolymers[28]

Janus particle synthesis via self-assembling of block copolymers is based on crosslinking of AB and BC copolymers. A and C are compatible with B copolymer; however, incompatible with each other. Additionally, A and C should be both soluble in a suitable solvent. To combine

them, AB and BC blocks are prepared separately and by crosslinking two blocks, ABC type block copolymer is obtained. This procedure is followed by precipitation during solvent evaporation. For the particle morphology, one should carefully adjust the weight fraction of B.

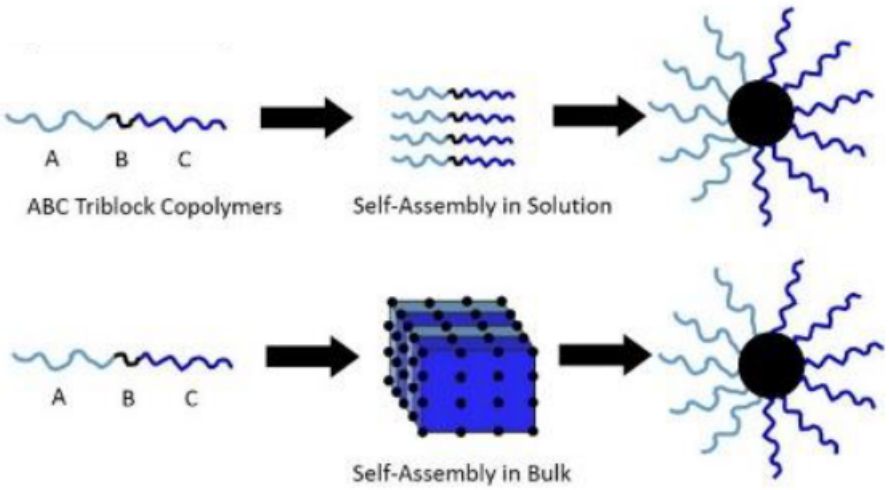

Figure 1.8: Janus particle synthesis via self-assembly. Reproduced from ref [28]

1.3.1.2 Masking

This method is simply surface modification of one portion of the particle while immobilization of the other part. Immobilization is achieved by entrapping the particles at a solid or in a liquid interface via pickering emulsion, planar solid substrate or wax[28,29]. To functionalize the particles, ligands, antibodies, small molecules, functional moieties, metallic coatings and superparamagnetic nanoparticles are some potential candidates to be used[30].

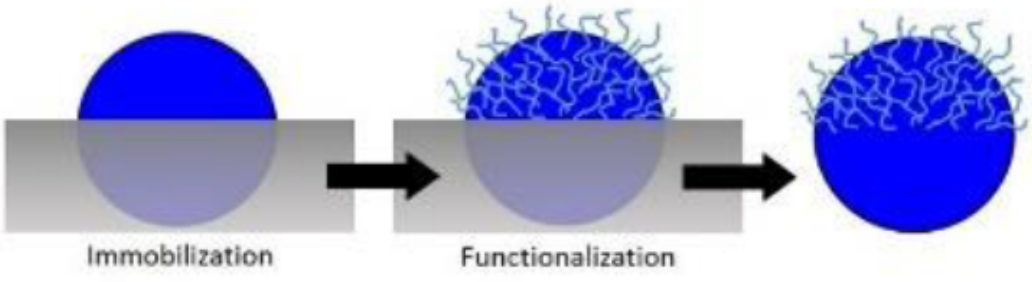

Figure 1.9: Janus particle synthesis via masking by using wax. Reproduced from ref [28]

1.3.1.3 Droplet Based Phase Separation

In droplet-based phase separation method, droplet formation occurs on the tip of a nozzle fed by two side-by-side channels merging into a single channel. Droplet-based phase separation procedure could be either microfluidics or electrohydrodynamic co-jetting, these two methods are commonly used in biodegradable Janus particles[31–33]. In former case, microfluidic devices work as templates for Janus particle synthesis via single emulsion, oil-water-oil double emulsion, or polymerization of monomers in aqueous solution[32,33] while in latter case, aqueous solutions of polymers are used[28].

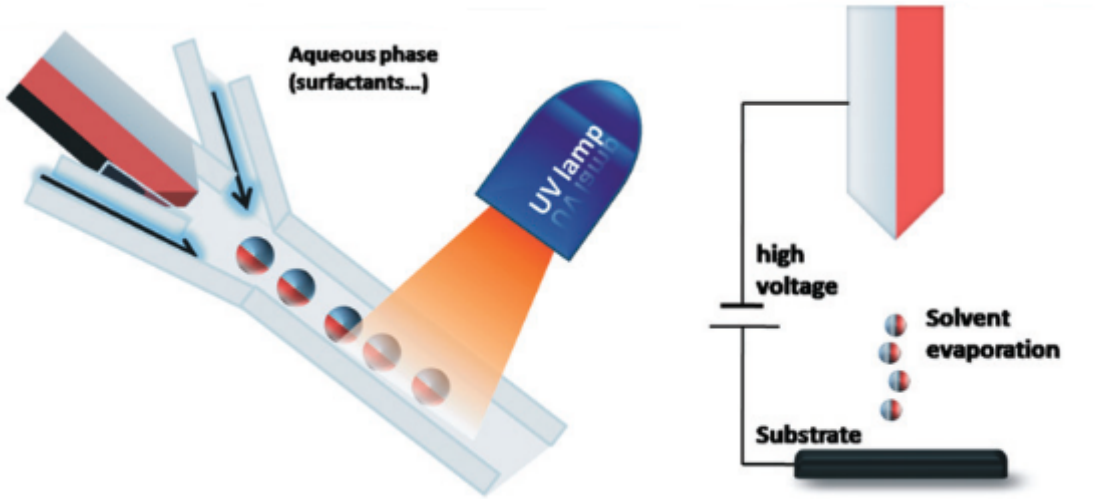

Figure 1.10: Left: Microfluidic photopolymerization system Right: Electrospinning using a bi-phasic nozzle. Reproduced from ref [29]

1.3.1.3.1 Microfluidics

Microfluidics is a very common method to fabricate not only Janus particles but also homogeneous particles. To fabricate Janus particles, there should always be two separate streams flowing parallel, instead of one stream. Additionally, the interface between two fluids should be stable. To successfully prepare desired Janus particles, two channels coordinatively working and a stable interface should be ensured. Janus geometry in microfluidic method could be achieved via UV-radiation (see Figure 1.10-left), heat or chemical treatment[33].

1.3.1.3.2 Electrohydrodynamic Co-Jetting

Electrospinning technology has been used to obtain nanofiber/nanoparticles for a decade. However, since 1990`s there was not a real interest on this technique except filter industry[34]. This technique is based on a system with two channels filled with polymers (see Figure 1.11), and when exposed to an applied voltage, the bipolar liquid is formed between the tip and the substrate (collector screen). The nanocolloids fabricated with this process, could take place in many application areas like drug delivery, molecular imaging or guided self-assembly[35].

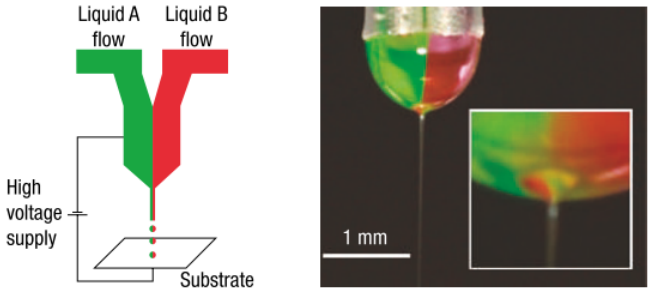

Figure 1.11: Biphasic electrified jetting using side-by-side dual capillaries. Reproduced from ref [35]

1.3.1.4 Seeded Polymerization

Seeded polymerization or so-called seeded emulsion polymerization (SEP) is a suitable technique to obtain dumbbell, acorn-like and snowman-like morphologies[23,36]. This technique comprises controlled nucleation and growth of two immiscible or incompatible polymers or a polymer and an inorganic material[28]. Crosslinked polymer seed particles are swollen with polymerizable monomer. Polymerization starts in the aqueous phase upon heating with the formation of free radicals and the addition of the first monomer units[23,28].

Temperature, monomer/polymer swelling ratio, affinity of monomer to polymer, crosslinking density, interfacial tension, monomer concentration, hydrophilicity of the cross-linked particle surface, and the size of the seeds are the important parameters affecting the final morphology of the synthesized particles[37–39]. SEP is a useful technique to be scaled up for industrial applications and it has advantages of high monodispersity, low cost and versatility[37].

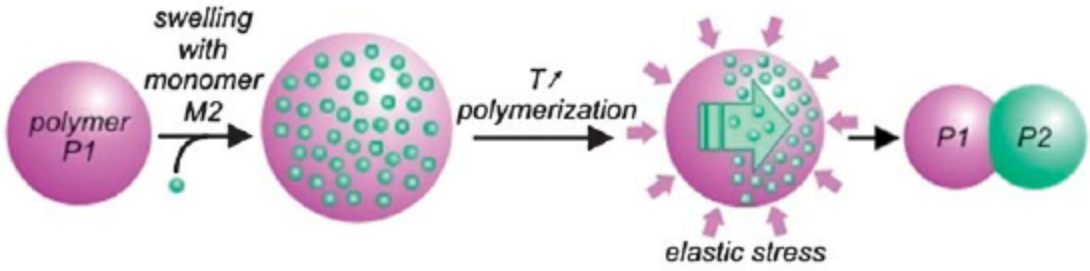

Figure 1.12: Schematic illustration of seeded polymerization technique to synthesize Janus particles. Reproduced from ref [36]

1.3.1.5 Emulsion Solvent Evaporation Method

This method has been used to obtain polymeric micro- and nanoparticles by using oil-in-water emulsion within the last 40 years. Emulsion solvent evaporation method comprised of an oil phase with a binary mixture of two incompatible polymers dissolved in a common solvent; and an aqueous phase consists of water and a surfactant. The oil phase is added to the aqueous phase and with the help of shear, oil-in-water emulsion is obtained[28].

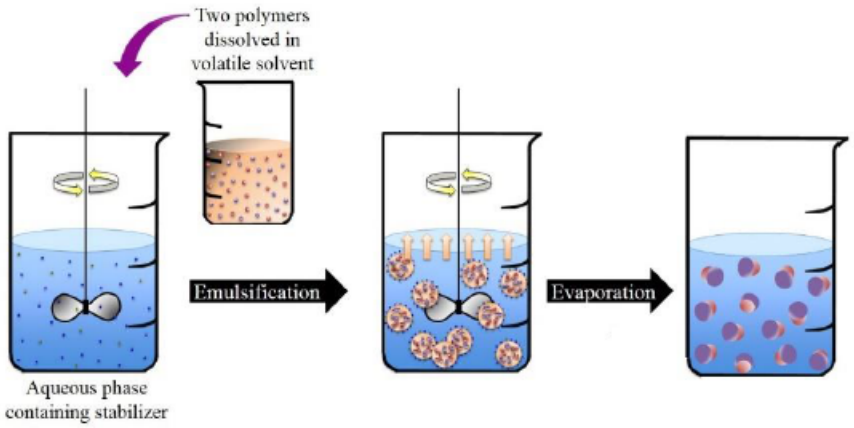

Figure 1.13: Schematic illustration of emulsion solvent evaporation method to synthesize Janus particles. Reproduced from ref [28]

1.4 Self-Propulsion

Self-propulsion, as a term, was first used in 1874 meaning propulsion by one's own power. In science, this phrase is defined as the ability to convert chemical or external energy into

mechanical motion for the structures mentioned as micro- and nano-motors referring to both natural and artificial motors[24,40].

Janus particles or in other words Micro-and Nano-motors could have variety of possibilities for self-propulsion. Abdelmohsen et. al. made a simple and useful frame regarding fuel dependencies and self-propulsion mechanisms of Micro- and Nano-Motors[24]. These tiny motors could be either fuel powered (H_2O_2, glucose, water, acid, base); or fuel free (Magnetically, electrically, light, ultrasound, living organisms driven) or a hybrid system[24,41,42].

Propulsion mechanisms of these tiny motors could be investigated under 2 main titles with respect to the direction of motion: Towards the catalyst or Away from the catalyst[24]. For Janus particles, there are simply 4 propulsion mechanisms[24,25,41]: Self-Diffusiophoresis, Bubble Propulsion, Self-electrophoresis and Interfacial Tension Motion Induced Propulsion, the direction of motion in self-diffusiophoresis and bubble propulsion is away from the catalyst while it is towards the catalyst in Self-electrophoresis and interfacial tension motion induced propulsion[24,25]. When spherical Janus particles are handled, 3 main propulsion mechanisms are mentioned: Self-Diffusiophoresis, Bubble Propulsion and Self-electrophoresis; in all of these mechanisms, particle motion is observed in the opposite direction of the catalyst[25] (see Figure 1.14).

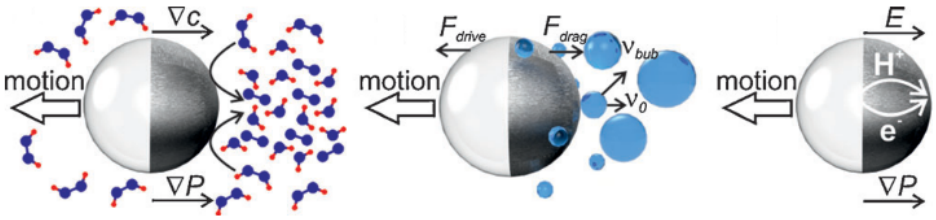

Figure 1.14: Different propulsion mechanisms for spherical Janus particles: A: Self Diffusiophoresis, B: Bubble-Propulsion, and C: Self-Electrophoresis. Reproduced from ref [25]

1.4.1 Self-Propulsion Mechanisms

1.4.1.1 Away from the Catalyst

In bubble propulsion mechanism, a fuel is decomposed by a catalyst. Decomposition of the

fuel results in micron sized gas bubble formation and when the bubbles burst, the particles start to move in the opposite direction of catalytic side as in the previous mechanism[43] (see Fig. 15-a). The most common system studied related with bubble propulsion mechanism is with platinum as a catalyst and H_2O_2 as a fuel[24]. In these systems H_2O_2 is decomposed into H_2O (aq) and O_2(g).

Self-diffusiophoresis is based on concentration gradient of the decomposition products in the system. In general, asymmetric catalytic motors show self-diffusiophoretic motion. Catalyst is positioned with the motor to accumulate the decomposition product of the fuel. When the accumulated decomposition products reach to a critical level, decomposition products start to decompose due to the high local concentration and this generates the motion of the motor in the opposite direction of the catalyst[42] (see Figure 1.15-right).

Figure 1.15: Schematic illustration of propulsion mechanisms in the opposite direction of the catalyst: Left: Bubble propulsion, Right: Self-diffusiophoresis. Reproduced from ref [41]

1.4.1.2 Towards the Catalyst

Interfacial tension motion induced propulsion is defined for the systems in which a large quantity of product is generated near or at the catalytic site[42]. The motor here has two parts of Au and Pt. Generated oxygen as a result of the decomposition of H_2O_2 at Pt side produces large bubbles at the gold interface. These large bubbles form a hydrophobic layer on Au side and interfacial tension at that end becomes lower than the Pt end inducing the motor to propel in the direction of Pt (see Figure 1.16-left).

Self-electrophoresis propulsion mechanism is based on an electric gradient generated inside asymmetric conductive bimetallic rods. The rod could be matched with an electrochemical

cell since one metallic end acts as the anode and the other as the cathode. Pt (as anode) end is the location for H_2O_2 to be oxidized by forming protons and electrons, the generated protons and electrons are used by the Au (cathode) end for the reduction of H_2O_2 into H_2O and O_2[44]. There is a flow of electrons from Pt to Au, and a flow of protons in the opposite direction. The motion of the resultant negatively charged microrod is observed through the proton rich environment, Pt end of the microrod[42] (see Figure 16-right).

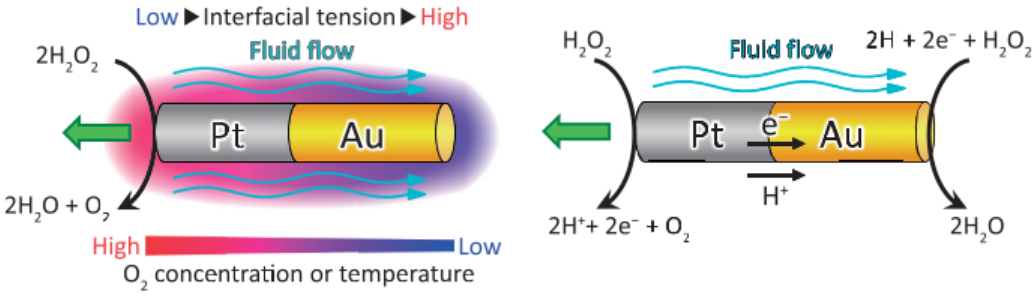

Figure 1.16: Schematic illustration of propulsion mechanisms in the opposite direction of the catalyst: Left: Interfacial tension gradient, Right: Self-electrophoresis. Reproduced from ref [41]

1.5 References

(1) Dhont, J. K. G. *An Introduction to Dynamics of Colloids*; Elsevier B.V., 1996.

(2) Selmi, F. Studies on the Demulsion of Silver Chloride. *Nouvi. Ann. Sci. Nat. Bol.* **1845**, *2* (4), 146.

(3) Faraday, M. On the Experimental Relations of Gold (and Other Metals) to Light. *Philos. Trans. R. Soc. London* **1857**, *147*, 145.

(4) Graham, T. Liquid Diffusion Applied to Analysis. *Philos. Trans. R. Soc. London* **1861**, *151*, 183–224.

(5) Currie, L. A. Nomenclature in Evaluation of Analytical Methods Including Detection and Quantification Capabilities (IUPAC Recommendations 1995). *Pure Appl. Chem.* **1995**, *67* (10), 1699–1723. https://doi.org/10.1351/pac199567101699.

(6) Doug H. Everett. *Basic Principles of Colloid Science*; RSC Paperbacks; Royal Society of Chemistry, 1988. https://doi.org/10.1002/jctb.280450412.

(7) Ostwald, C. W. W. *A Handbook of Colloid-Chemistry. The Recognition of Colloids, the Theory of Colloids and Their General Physico-Chemical Properties.*; 1916; Vol. LXVI. https://doi.org/10.1001/jama.1916.02580330065035.

(8) Uskoković, V. Dynamic Light Scattering Based Microelectrophoresis: Main Prospects and Limitations. *J. Dispers. Sci. Technol.* **2012**, *33* (12), 1762–1786. https://doi.org/10.1080/01932691.2011.625523.

(9) Derjaguin, B.; Landau, L. Theory of the Stability of Strongly Charged Lyophobic Sols and of the Adhesion of Strongly Charged Particles in Solutions of Electrolytes. *Acta Physicochim. U.R.S.S.* **1941**, *14*, 633–662.

(10) Verwey, E.J.W. and Overbeek, J. T. G. Theory of Stability of Lyophobic Colloids. *Elsevier, Amsterdam* **1948**, 631–636.

(11) Ortega-Vinuesa, J. L.; Martín-Rodríguez, A.; Hidalgo-Álvarez, R. Colloidal Stability of Polymer Colloids with Different Interfacial Properties: Mechanisms. *J. Colloid Interface Sci.* **1996**, *184* (1), 259–267. https://doi.org/10.1006/jcis.1996.0619.

(12) Matusiak, J.; Grzadka, E. Stability of Colloidal Systems-a Review of the Stability Measurements Methods. *Ann. Univ. Mariae Curie-Sklodowska* **2017**, *LXXII* (1), 33–45. https://doi.org/10.17951/aa.2017.72.1.33.

(13) Semenov, A. N.; Shvets, A. A. Theory of Colloid Depletion Stabilization by Unattached and Adsorbed Polymers. *Soft Matter* **2015**, *11* (45), 8863–8878. https://doi.org/10.1039/c5sm01365h.

(14) Granick, S.; Jiang, S.; Chen, Q. Janus Particles. *Phys. Today* **2009**, *62* (7), 68–69. https://doi.org/10.1063/1.3177238.

(15) Zhang, J.; Luijten, E.; Granick, S. Toward Design Rules of Directional Janus Colloidal Assembly. *Annu. Rev. Phys. Chem.* **2015**, *66* (1), 581–600.

https://doi.org/10.1146/annurev-physchem-040214-121241.

(16) Yang, S. M.; Kim, S. H.; Lim, J. M.; Yi, G. R. Synthesis and Assembly of Structured Colloidal Particles. *J. Mater. Chem.* **2008**, *18* (19), 2177–2190. https://doi.org/10.1039/b716393b.

(17) Retrieved from: https://apps.webofknowledge.com/CitationReport.do?action=home&product=WOS&search_mode=CitationReport&cr_pqid=2&qid=2&isCRHidden=&SID=F3UnhRHdJqSmmzN4xik.

(18) de Gennes, P.-G. Soft Matter (Nobel Lecture). *Angew. Chemie Int. Ed. English* **1992**, *31* (7), 842–845. https://doi.org/10.1002/anie.199208421.

(19) Casagrande, C.; Fabre, P.; Raphaël, E.; Veyssié, M. "Janus Beads": Realization and Behaviour at Water/Oil Interfaces. *Europhys. Lett.* **1989**, *9* (3), 251–255. https://doi.org/10.1209/0295-5075/9/3/011.

(20) Liu, B.; Zhang, W.; Zhang, D.; Yang, X. Facile Method for Large Scale Synthesis of Magnetic Inorganic-Organic Hybrid Anisotropic Janus Particles. *J. Colloid Interface Sci.* **2012**, *385* (1), 34–40. https://doi.org/10.1016/j.jcis.2012.06.032.

(21) Hu, J.; Zhou, S.; Sun, Y.; Fang, X.; Wu, L. Fabrication, Properties and Applications of Janus Particles. *Chem. Soc. Rev.* **2012**, *41* (11), 4356. https://doi.org/10.1039/c2cs35032g.

(22) Wang, F. Development of Janus Nanocomposites as a Multifunctional Nanocarrier for Cancer Therapy, 2013.

(23) Perro, A.; Reculusa, S.; Ravaine, S.; Bourgeat-Lami, E.; Duguet, E. Design and Synthesis of Janus Micro- and Nanoparticles. *J. Mater. Chem.* **2005**, *15* (35–36), 3745–3760. https://doi.org/10.1039/b505099e.

(24) Abdelmohsen, L. K. E. A.; Peng, F.; Tu, Y.; Wilson, D. A. Micro- and Nano-Motors for Biomedical Applications. *J. Mater. Chem. B* **2014**, *2* (17), 2395–2408.

https://doi.org/10.1039/c3tb21451f.

(25) Sanchez, S.; Soler, L.; Katuri, J. Chemically Powered Micro- and Nanomotors. *Angew. Chemie - Int. Ed.* **2015**, *54* (5), 1414–1444. https://doi.org/10.1002/anie.201406096.

(26) Kaewsaneha, C.; Tangboriboonrat, P.; Polpanich, D.; Eissa, M.; Elaissari, A. Preparation of Janus Colloidal Particles via Pickering Emulsion: An Overview. *Colloids Surfaces A Physicochem. Eng. Asp.* **2013**, *439*, 35–42. https://doi.org/10.1016/j.colsurfa.2013.01.004.

(27) Poggi, E.; Gohy, J. F. Janus Particles: From Synthesis to Application. *Colloid Polym. Sci.* **2017**, *295* (11), 2083–2108. https://doi.org/10.1007/s00396-017-4192-8.

(28) Winkler, J. S. Emulsion-Based Synthesis and Characterization of Biphasic Janus Particles for Dual Drug Delivery, 2016.

(29) Walther, A.; Müller, A. H. E. Janus Particles. *Soft Matter* **2008**, *4* (4), 663–668. https://doi.org/10.1039/b718131k.

(30) Turcheniuk, K.; Tarasevych, A. V.; Kukhar, V. P.; Boukherroub, R.; Szunerits, S. Recent Advances in Surface Chemistry Strategies for the Fabrication of Functional Iron Oxide Based Magnetic Nanoparticles. *Nanoscale* **2013**, *5* (22), 10729–10752. https://doi.org/10.1039/c3nr04131j.

(31) Misra, A. C.; Bhaskar, S.; Clay, N.; Lahann, J. Multicompartmental Particles for Combined Imaging and SiRNA Delivery. *Adv. Mater.* **2012**, *24* (28), 3850–3856. https://doi.org/10.1002/adma.201200372.

(32) Yang, S.; Guo, F.; Kiraly, B.; Mao, X.; Lu, M.; Leong, K. W.; Huang, T. J. Microfluidic Synthesis of Multifunctional Janus Particles for Biomedical Applications. *Lab Chip* **2012**, *12* (12), 2097–2102. https://doi.org/10.1039/c2lc90046g.

(33) Chen, C. H.; Shah, R. K.; Abate, A. R.; Weitz, D. A. Janus Particles Templated from Double Emulsion Droplets Generated Using Microfluidics. *Langmuir* **2009**, *25* (8), 4320–4323. https://doi.org/10.1021/la900240y.

(34) Reneker, D. H.; Chun, I. Nanometre Diameter Fibres of Polymer, Produced by Electrospinning. *Nanotechnology* **1996**, *7* (3), 216–223. https://doi.org/10.1088/0957-4484/7/3/009.

(35) Roh, K.; Martin, D. C.; Lahann, J. Biphasic Janus Particles with Nanoscale Anisotropy. *Nat. Mater.* **2005**, *4* (10), 759–763. https://doi.org/10.1038/nmat1486.

(36) Loget, G.; Kuhn, A. Bulk Synthesis of Janus Objects and Asymmetric Patchy Particles. *J. Mater. Chem.* **2012**, *22* (31), 15457–15474. https://doi.org/10.1039/c2jm31740k.

(37) Sijia, W. Synthesis and Applications of Anisotropic Colloidal Dimers, 2015.

(38) Saito, N.; Kagari, Y.; Okubo, M. Revisiting the Morphology Development of Solvent-Swollen Composite Polymer Particles at Thermodynamic Equilibrium. *Langmuir* **2007**, *23* (11), 5914–5919. https://doi.org/10.1021/la063653n.

(39) Saito, N.; Nakatsuru, R.; Kagari, Y.; Okubo, M. Formation of "Snowmanlike" Polystyrene/Poly(Methyl Methacrylate)/Toluene Droplets Dispersed in an Aqueous Solution of a Nonionic Surfactant at Thermodynamic Equilibrium. *Langmuir* **2007**, *23* (23), 11506–11512. https://doi.org/10.1021/la701388w.

(40) Schliwa, M.; Woehlke, G. Molecular Motors. *Nature* **2003**, *422* (April), 759–765. https://doi.org/10.1038_nature01601.

(41) Yamamoto, D.; Shioi, A. Self-Propelled Nano/Micromotors with a Chemical Reaction: Underlying Physics and Strategies of Motion Control. *KONA Powder Part. J.* **2015**, *32* (32), 2–22. https://doi.org/10.14356/kona.2015005.

(42) Gibbs, J.; Zhao, Y. Catalytic Nanomotors: Fabrication, Mechanism, and Applications. *Front. Mater. Sci. China* **2011**, *5* (1), 25–39. https://doi.org/10.1007/s11706-011-0120-x.

(43) Gibbs, J. G.; Zhao, Y. P. Autonomously Motile Catalytic Nanomotors by Bubble Propulsion. *Appl. Phys. Lett.* **2009**, *94* (16). https://doi.org/10.1063/1.3122346.

(44) Paxton, W. F.; Baker, P. T.; Kline, T. R.; Wang, Y.; Mallouk, T. E.; Sen, A. Catalytically Induced Electrokinetics for Motors and Micropumps. *J. Am. Chem. Soc.* **2006**, *128* (46), 14881–14888. https://doi.org/10.1021/ja0643164.

CHAPTER 2: INSTRUMENTATION TECHNIQUES

For the studies based on colloids, there are several instrumentation techniques that quantify our observations. These techniques can give information on microstructure, stability, determination of the factors (addition of components like polymers, surfactants) influencing the system etc. These techniques mainly include light scattering, optical microscopy, electron microscopy, UV-VIS spectrometry, turbidimetry, zeta potential and density measurements.

In this study, our main concern was characterization of the particles obtained from the colloidal mixtures and we focused on the methods to characterize the supra-particles. Therefore, in this work, optical microscopy and electron microscopy techniques were the techniques mostly used.

2.1 Optical Microscopy (OM)[1]

Optical microscopy is one of the most common methods for bulk and surface characterization on larger length scales. With the help of an optical microscope, it is possible to get information about surface topology, structure and chemistry of the materials.

The purpose of the production and design of the optical microscopes stems from the necessity to create magnified visual or photographic images of small objects. To obtain these images, there are simply two ways based on the way how the light is projected on the sample: transmission and reflection. Transmission is used for very thin specimens; reflection is used for thicker or nontransparent material.

The main components of a standard optical microscope could be counted as: Lenses, eyepieces (oculars), and light source (see Figure 2.1). The location of the light source and ocular could differ in different types of optical microscopes.

Figure 2.1: Main components of a compound light microscope. Reproduced from ref [2]

Resolution and poor contrast are the main limitations of optical microscopy. Poor contrast occurs when the light is passed through very thin samples or reflected from surfaces with a high degree of reflectivity. Resolution could be adjusted by diffraction (d) which is dependent on the numerical aperture (NA) of the optical system and the optical wavelength (λ) of the light used. The relation is given by the equation: $= \frac{\lambda}{\mathrm{NA}}$. To talk about an optical micrograph with desired resolution, one should consider two terms: Magnification and Numerical Aperture.

Magnification[3]**:** The magnification of an image is the size of that image at the detector. For the simple ordinary lenses, the magnification is given by the negative ratio of the distance between the image and the object: $M_T=-d_i/d_o$. The reason for the negative sign arises from the inversion of the image by a simple lens. Magnification in axial direction is calculated by taking the square of the transverse magnification: $M_L= - M^2_T$. The total magnification, M_r of an image is the product of the objective and the eyepiece magnifications, M_E. M_E is given by 250 mm/f, where f is the focal length of the eyepiece lens. By knowing M_E and M_T, the total magnification M_r is calculated by multiplying them, $M_r = M_T.M_E$.

Numerical Aperture: To catch a clear image in an optical microscope, resolution is very important; however, to talk about a good resolution, magnification is not enough, the numerical aperture (NA) of the object is also necessary to be known. Numerical aperture is defined with the formula: NA = n.sinα. The term 'n' refers to the refractive index of the medium between the lens and the sample, α refers to the half angle subtended by the lens at its focus (Figure

2.2). As the angle gets greater, more light could be collected; therefore, numerical aperture is a measure not only for the resolution but also for the light gathering ability of the lens[3].

As soon as the medium between the specimen and the lens is kept as air, NA could not be greater than 1. To obtain the values greater than 1, one should choose a medium with a refractive index larger than air[4].

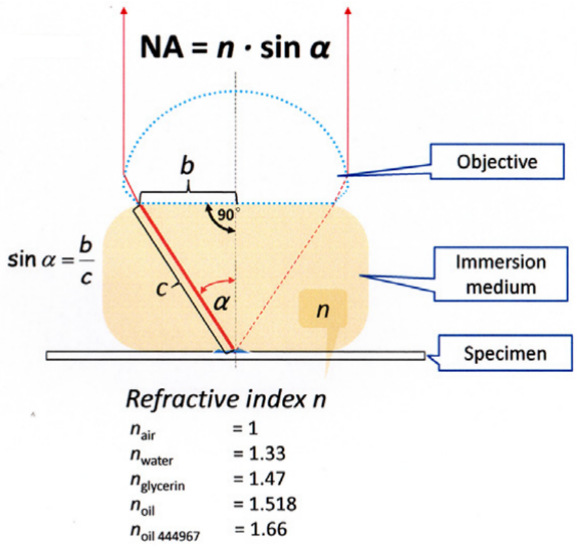

Figure 2.2: Numerical aperture and the angle of coming light. Reproduced from ref [4]

2.2 Electron Microscopy (EM)[5]

Light microscopy is a very convenient and common method for surface characterization; however, it has a very important limitation, resolution. The maximum resolving power of optical microscopes is about 200 nm due to the fixed minimum wavelength of visible light. Electron microscopy methods have much better resolution compared to the optical microscopy as EM methods use beam of electrons instead of beam of photons to visualize the sample.

In EM, the major limitation is that it could not be applied to living specimen, even it is applied, one may encounter with artifacts that does not exist previously. To eliminate/reduce these artifacts, samples can be exposed to rapid freezing.

2.2.1 Scanning Electron Microscope (SEM)[1]

SEM is more informative compared to the previous imaging techniques. This technique uses electrons instead of light to visualize an image, which provides a larger depth of field. Having a larger depth of field compared to other methods, enables us to focus on a larger amount of sample at once. By using SEM, it is possible to reach resolution values better than 1nm[6]. Additionally, it is very common to couple SEM with energy dispersive spectroscopy (EDS) X-ray diffraction[1,6], this coupling provides both high magnification on characterizing the surfaces and elemental compositional analysis at the same time. Sample preparation for SEM measurement is easy as soon as samples are conductive. For the nonconductive samples, like polymers, coating them with gold works properly. SEM gives opportunity to researchers to observe their systems in high vacuum, in low vacuum or in wet conditions[6].

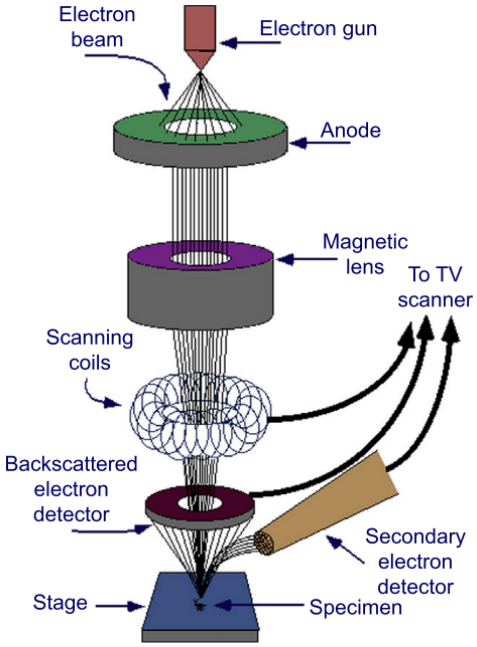

Figure 2.3: Schematic diagram of a Scanning Electron Microscope. Reproduced from ref [6]

2.2.2 Transmission Electron Microscope (TEM)

Transmission electron microscopy (TEM), produces 2-D images by using a beam of electrons passing through a thin section of specimen. Extremely thin (<100 nm) sections are stained with atoms of electron dense heavy metals and when the beam hits the heavy metal atoms in the

sample, the electrons are either absorbed or scattered forming electron-dense areas appear dark. Magnification and focusing of the image occur via bending charged electron trajectories. As electrons are not visible by naked eye, electron intensity variations are converted into photons by projecting the electrons into a special detector or onto a screen (fluorescent screen, a layer of photographic film[6]) that fluoresces at intensities relative to the amount of hit beam electrons.[5]

TEM technique provides higher magnification than SEM and it is widely preferred in materials science by being applicable to crystalline materials. TEM has simply two main limitations: test specimen is needed to be foiled and it should be resistant against high vacuum inside. Due to that limitations, inorganic and nonbiological samples are suitable for TEM measurements[1].

In the figure below, there are schematic diagrams of light/optical microscopy, scanning electron microscopy and transmission electron microscopy showing the differences in design of the instruments given for comparison (Figure 2.4).

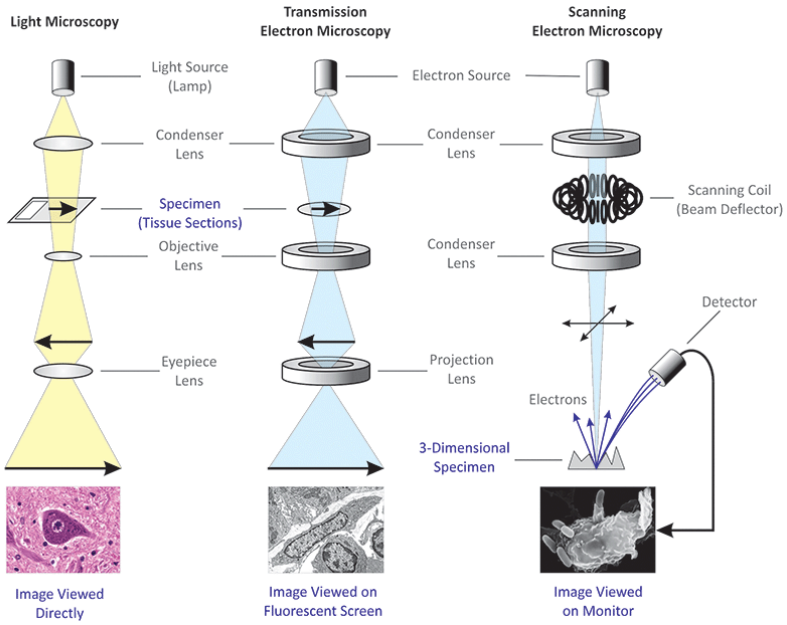

Figure 2.4: Differences between OM, SEM and TEM in instrumentation design. Reproduced from ref [7]

2.3 Confocal Micro X-Ray Fluorescence Spectroscopy (CMXRF)

The Optical Principle of Confocal Imaging

A confocal microscope is an integrated system of a microscope, multiple laser light sources, a confocal scan head (consisting of: inputs from one or more external laser light sources, fluorescence filter sets, a galvanometer-based raster scanning mechanism, one or more variable pinhole apertures for generating the confocal image and photomultiplier tube detectors for different fluorescent wavelengths) with optical and electronic equipment, a computer and monitor for display and software for acquiring, processing and analyzing images[2].

Micro X-ray Fluorescence Spectroscopy

'Micro' XRF involves imaging of the localized regions of a sample with spatial resolution in micrometer scale. This technique enables to obtain information on both the elemental composition of the sample and their related spatial distribution[8].

XRF imaging in micrometer scale is a very powerful technique for the observation of elemental distributions within a sample. The size of the X-ray beam determines the minimal spatial resolution of an obtained image. With the improvements during the last decade, micro/nano X-ray fluorescence spectroscopy has become a very promising non-invasive method to analyze the samples qualitatively and quantitively[9].

Confocal Micro X-ray Fluorescence Spectroscopy

In Micro X-ray fluorescence spectroscopy, atoms in the samples are excited with a microfocus X-ray tube. To concentrate the polychromatic radiation of the X-ray tube, a polycapillary (full-) lens is used. With the radiation impinging on the sample, atoms are ionized resulting in fluorescence photons characteristic to the atomic number. Fluorescence photons are collected with the help of a second polycapillary optic in front of an energy dispersive silicon drift detector (SDD) spatially and by moving the sample stepwise in three dimensions 3D images of the fluorescence intensities of different elements is obtained[10]. A basis model for advanced quantification procedures for 3-D micro-XRF spectroscopy was proposed in 2005 by Malzer and Kanngieβer[11].

The schematic illustration of the confocal set-up for confocal micro-XRF-spectroscopy is shown in the figure below (Figure 2.5)

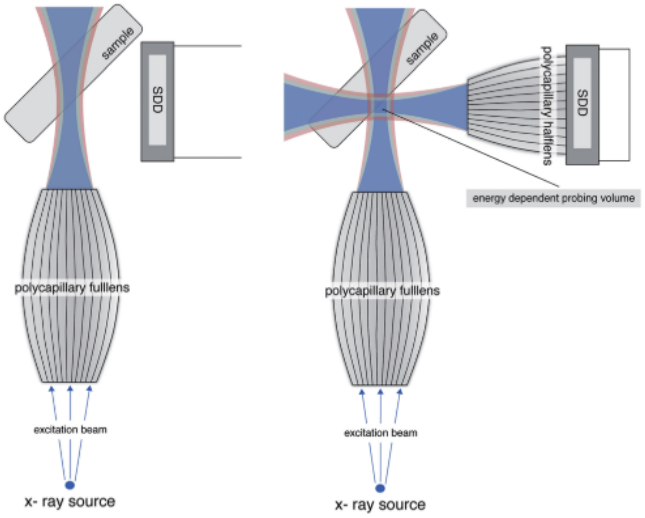

Figure 2.5: Schematic illustration of micro-XRF and 3-D micro-XRF spectroscopy. Reproduced from ref [10]

2.4 Dynamic/Static Light Scattering (DLS/SLS)

Static and Dynamic Light Scattering are optical methods commonly used for characterization of dispersed systems. It is a technique to quantify the Brownian Motion of individual particles in liquid systems for the evaluation of particle sizes[12]. DLS is a non-invasive and well-established technique to obtain the size of the molecules and particles in submicron range. With the Stokes-Einstein relationship, size of the particles is evaluated[13]:

$$d_H = \frac{kT}{3\pi\eta D} \qquad \text{Eqn. 2.1}$$

where d_H is hydrodynamic diameter, k is Boltzman`s constant, T is the absolute temperature, η is the viscosity of the solvent and D is the diffusion coefficient.

DLS measures the time dependence of the fluctuating intensity[14]. The sample is illuminated by being placed in the patch of a laser beam and a photomultiplier detects the scattered light by the particles. At the hearth of the instrument, there is a device called correlator which measures

the degree of similarity of a specific signal over a period of time[13]. The main components of a typical experimental set-up for dynamic light scattering is shown in the figure below.

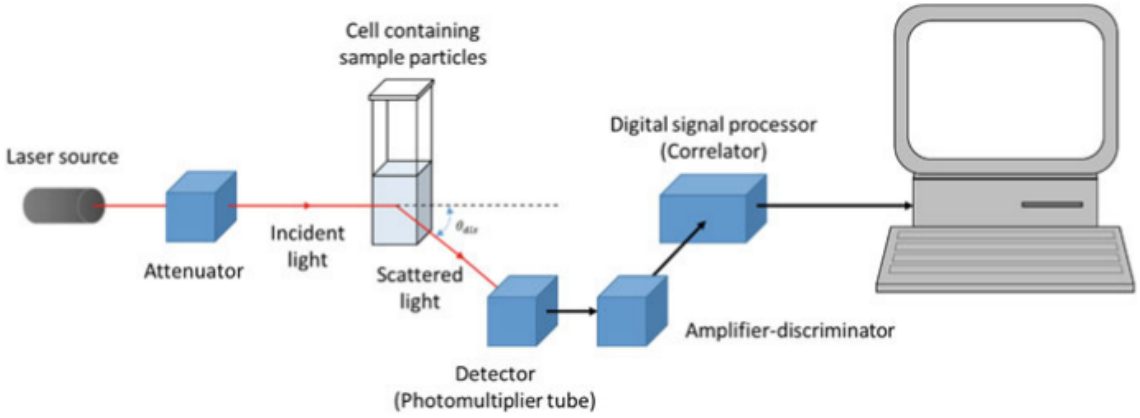

Figure 2.6: Components of a typical experimental set-up for DLS. Reproduced from ref [15]

In Static Light Scattering (SLS), the mean intensity is measured as a function of the scattering angle at fixed wavelengths. Different from DLS which is based on the intensity fluctuations, SLS does not have a correlator in the set-up and the amplifier is directly connected to the monitor. In addition to the absence of the correlator, SLS has multiple detectors fixed at different angles.

2.5 Inductively Coupled Plasma Optical Emission Spectroscopy (ICP-OES)

ICP-OES is one of the most powerful method for the detection of trace elements in the samples (agricultural, biological, geological, organic, metallic compounds etc.) containing a wide variety of elements[16,17]. The modern instrumentation of this technique was first explored by Velmer Fassel and Stanley Greenfield with low power system (1-2 kW) in 1962[17]. ICP-OES is a type of emission spectroscopy using inductively coupled plasma (sustaining a temperature of approximately 6000-10000 K[16,17]) to excite the atoms and ions instead of flame as in (Atomic Absorption Spectroscopy) AAS and (Atomic Emission Spectroscopy) AES. ICP-OES set-up consists of an argon plasma torch, mono/polychromator or echelle optical system, detector(s) and a computer[18]. The main advantages of ICP-OES compared to AAS and AES are the capability of multielement detection, being more sensitive and being less prone to

matrix interferences[17]. There is a schematic illustration of an ICP-OES instrument in the figure below.

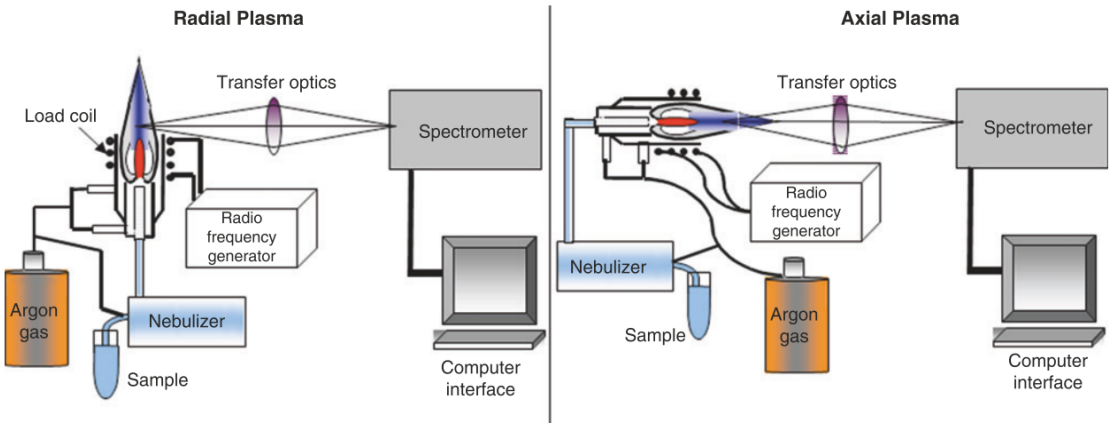

Figure 2.7: Major components of Left: radially viewed, Right: axially viewed ICP-OES instrument. Reproduced from ref [17]

For ICP-OES measurement, the sample is converted to an aerosol through nebulization and transported to the plasma to be desolvated, vaporized, atomized and excited and/or ionized by the plasma. Excited atoms or ions emit electromagnetic radiation characteristic to each atom. The radiation is then collected and sorted by wavelength[19].

2.6 References

(1) Bergström, J. Experimental Characterization Techniques. In *Mechanics of Solid Polymers*; Elsevier, 2015; pp 19–114. https://doi.org/10.1016/B978-0-323-31150-2.00002-9.

(2) Murphy, D. B.; Davidson, M. W. *Fundamentals of Light Microscopy and Electronic Imaging*; John Wiley & Sons, Inc.: Hoboken, NJ, USA, 2012. https://doi.org/10.1002/9781118382905.

(3) Corle, T. R.; Kino, G. S. *Confocal Scanning Optical Microscopy and Related Imaging Systems*; Academic Press: San Diego, 1996. https://doi.org/10.1016/B978-0-12-408750-7.X5008-3.

(4) Rottenfusser, R. *Proper Alignment of the Microscope*, 4th ed.; Elsevier Inc., 2013; Vol. 114. https://doi.org/10.1016/B978-0-12-407761-4.00003-8.

(5) Carter, M.; Shieh, J. Microscopy. In *Guide to Research Techniques in Neuroscience*; Elsevier, 2015; pp 117–144. https://doi.org/10.1016/B978-0-12-800511-8.00005-8.

(6) Di Gianfrancesco, A. *Technologies for Chemical Analyses, Microstructural and Inspection Investigations*; Elsevier Ltd, 2017. https://doi.org/10.1016/B978-0-08-100552-1.00008-7.

(7) Differences between Light Microscope and Electron Microscope https://microbiologyinfo.com/differences-between-light-microscope-and-electron-microscope/.

(8) Wolff, N. L. R. W. H. *Handbook of Practical X-Ray Fluorescence Analysis*; Beckhoff, B., Kanngießer, B., Langhoff, N., Wedell, R., Wolff, H., Eds.; Springer-Verlag: Berlin, Heidelberg, 2006. https://doi.org/10.1007/978-3-540-36722-2.

(9) Tsuji, K.; Nakano, K.; Takahashi, Y.; Hayashi, K.; Ro, C. X-Ray Spectrometry. *Anal. Chem.* **2012**, *84* (2), 636–668. https://doi.org/10.1021/ac202871b.

(10) Seim, C.; Laurenze-Landsberg, C.; Schröder-Smeibidl, B.; Mantouvalou, I.; de Boer, C.; Kanngießer, B. Old Traces, Read Anew – 'The Reading Hermit' Painting in the Light of X-Ray Fluorescence. *J. Anal. At. Spectrom.* **2014**, *29* (8), 1354. https://doi.org/10.1039/C3JA50301A.

(11) Malzer, W.; Kanngieβer, B. A Model for the Confocal Volume of 3D Micro X-Ray Fluorescence Spectrometer. *Spectrochim. Acta Part B At. Spectrosc.* **2005**, *60* (9–10), 1334–1341. https://doi.org/10.1016/j.sab.2005.07.006.

(12) Babick, F. Dynamic Light Scattering (DLS). In *Characterization of Nanoparticles*; Elsevier, 2020; pp 137–172. https://doi.org/10.1016/B978-0-12-814182-3.00010-9.

(13) Williams, P. M.; Oatley-Radcliffe, D. L.; Hilal, N. Feed Solution Characterization. In *Membrane Characterization*; Elsevier: Swansea, 2017; pp 379–404.

https://doi.org/10.1016/B978-0-444-63776-5.00017-6.

(14) Dhont, J. K. G. *An Introduction to Dynamics of Colloids*; Elsevier B.V.: Amsterdam, 1996.

(15) Sharma, S. K.; Verma, D. S.; Khan, L. U.; Kumar, S.; Khan, S. B. *Handbook of Materials Characterization*; Springer International Publishing, 2018. https://doi.org/10.1007/978-3-319-92955-2.

(16) Ho, X.; Jones, B. T. Inductively Coupled Plasma-Optical Emission Spectroscopy. In *Encyclopedia ofAnalytical Chemistry*; Meyers, R. A., Ed.; John Wiley & Sons, Ltd, 2001; pp 9468–9485. https://doi.org/10.1021/ac60349a722.

(17) *Encyclopedia of Geochemistry*; White, W. M., Ed.; Encyclopedia of Earth Sciences Series; Springer International Publishing: Cham, 2018. https://doi.org/10.1007/978-3-319-39312-4.

(18) Baker, K.; Flatman, S. *Food Analysis*, 4th ed.; Nielsen, S. S., Ed.; Food Science Texts Series; Springer US: Boston, MA, 2010. https://doi.org/10.1007/978-1-4419-1478-1.

(19) Boss, C. B.; Fredeen, K. J. *Concepts, Instrumentation and Techniques in Inductively Coupled Plasma Optical Emission Spectrometry*; The Perkin-Elmer Corporation, 1999.

CHAPTER 3: SUPER-HYDROPHOBIC SURFACES

3.1 Introduction

3.1.1 Contact Angle and Wetting

3.1.1.1 Contact Angle

Contact angle is simply defined as the angle at the intersection of liquid-vapor and liquid-solid interface. Steady forces at the intersection line of solid, liquid and vapor determine the magnitude of contact angle[1]. The quantification of wettability of the surfaces was first defined by Thomas Young with Young`s equation in 1805[2]. In his paper, he stated that contact angle is formed in case of wetting of a solid surface by a liquid and based on his equation, contact angle/or static contact angle depends on three forces: surface tension of the solid surface (Υ_{SV}), surface tension of the liquid (Υ_{LV}), and surface tension of the solid-liquid interface (Υ_{SL}). $\Upsilon_{SV} = \Upsilon_{LV}.cos\theta + \Upsilon_{SL}$ As a term 'dynamic' is used for contact angle in case of the three-phase boundary is in actual motion[3,4].

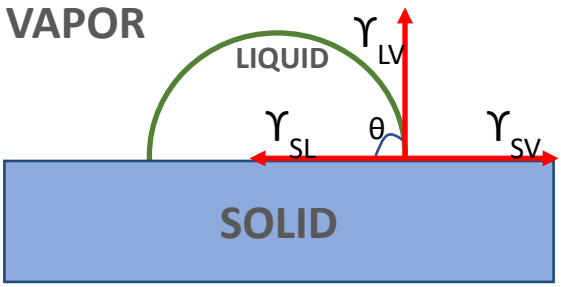

$$cos\theta = \frac{\gamma_{SV} - \gamma_{SL}}{\gamma_{LV}}$$

Eqn. 3.1

Figure 3.1: Vector representation of the forces forming contact angle.

3.1.1.2 Contact Angle Hysteresis

Young's equation is applicable for ideal surfaces like rigid, flat, nonreactive, inert, homogeneous, insoluble, smooth and nonporous[1]. However, real surfaces are not ideal so the parameters applied for ideal surfaces are not applicable for real surfaces[5,6]. As a result of having non-ideal systems, contact angle may differ from one spot to another due to interfacial tensions[1].

In non-ideal systems, there may be many metastable intermediates of a droplet on a surface which results in getting more than one contact angle value for a single system; therefore, one cannot talk about just one static state[1]. At this point, contact angle hysteresis is needed to be involved. Contact angle hysteresis is the difference of advancing contact angle, θ_A and receding contact angle, θ_R. The former is the angle formed while a droplet is slowly expanding over a surface, and the latter is the angle formed while the droplet is contracting along its previous path[7] (see Figure 3.2). The related equation is given below:

$$H = \theta_A - \theta_R \qquad \text{Eqn. 3.2}$$

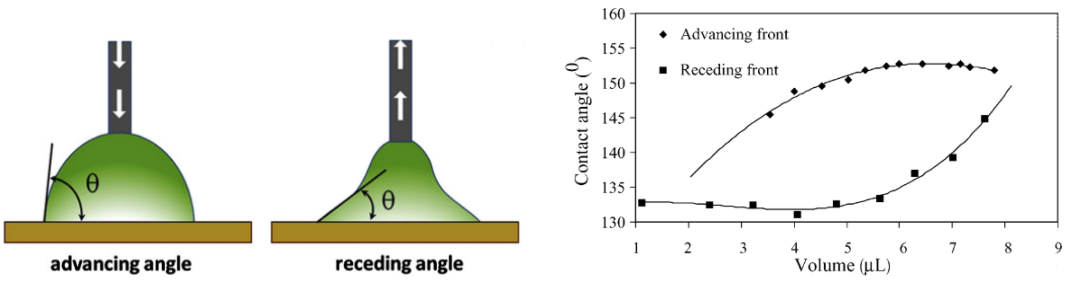

Figure 3.2: Left: Schematic illustration of advancing and receding angle. Reproduced from ref [1] and Right: graphical representation of advancing and receding contact angle. Reproduced from ref [8]

3.1.1.3 Coffee Stain Effect

Contact angle hysteresis affects some pattern formations on the surfaces. Coffee stain/ ring is one of the specific examples of the patterns caused by contact angle hysteresis. Coffee particles which are dispersed homogeneously in the initial case, become contracted during evaporation of the solute[9]. This phenomenon is observed not only for coffee but also for other systems including solids dispersed in an evaporating droplet. Deegan et. Al. defines this phenomenon as the migration of the solid particles in a drying drop to the edge of the drop and form a solid ring[10] (Figure 3.3).

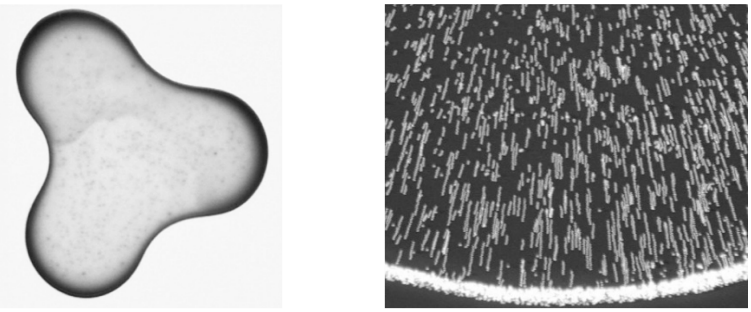

Figure 3.3: Left: Dried image of a 2-cm diameter drop of coffee containing 1 wt% solids; Right: Spheres in water during evaporation. Reproduced from ref [9]

"The rougher the surface, the easier the drop will pin" was mentioned by Eral et Al.[4] to clarify contact angle hysteresis and coffee stain effect. This relation could be explained with thinking about a droplet sliding on a tilted window. If the surface is smooth, drop slides down slowly, if the surface is rough the droplet sticks because of pinning of the contact line. The drop and/or the contact line stays stable depending on the roughness degree of the surface. When a sessile droplet starts to evaporate, the contact line has the tendency to move inwards over the cracks and dents on the surface; therefore, the rougher the surface, the easier the drop will pin. During evaporation in case of existence of non-volatile components in a volatile solvent, coffee ring effect is observed. In addition, as non-volatile components confined at the three-phase contact line, they contribute the pinning formed due to surface roughness. A droplet on a rough surface forms a wedge-like shape as illustrated in the figure below. When evaporation starts, the local evaporation rate (J) increases towards the edges due to the shape of the drop. One would expect all the liquid could be removed at the perimeter; however, as the contact line of the drying drop is pinned, the radius of the drop cannot shrink ensuring the liquid evaporation occurs from the edge replaced by the liquid from the interior[9]. The reason of this capillary flow from center to the edges is the larger free space of an evaporating molecule available at the rim compared to the center of the drop. As a result of the higher evaporation rate at the periphery of the drop, evaporation rate becomes diffusion limited. In the figure below on the left, the schematic illustration of coffee stain formation and on the right a microscope image of a fluorescently labeled coffee stain are presented.

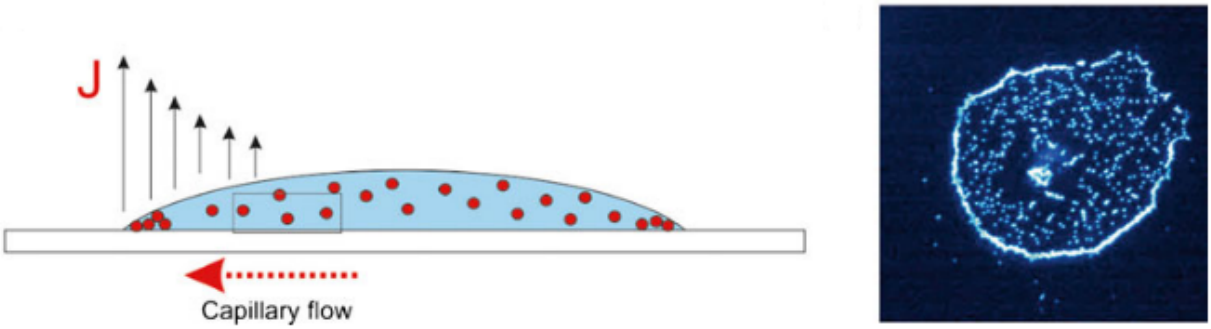

Figure 3.4: Left: Illustration of coffee stain formation; Right: A microscope image of a coffee stain formed by fluorescently labeled 5 µm particles. Reproduced from ref [4]

3.1.1.4 Wetting

The term 'wettability' arises from the concept of contact angle. In nature we observe partial wetting in most cases. Therefore, we must define the mid-cases well to clarify wetting or wettability. Zisman[11] made the definition of two terms: spreading and wetting. Spreading occurs when a liquid wets the solid surface completely, $\theta=0$; wetting occurs when a liquid wets a solid surface to some extent, $\theta\neq180$. In other words, 'there is always some adhesion of any liquid to any solid'[11].

When contact angle (CA) of a liquid drop with a solid surface is lower than 90°, high wettability occurs and; in the reverse case with the angles higher than 90°, low wettability occurs. In other words, with CA values lower than 90°, we observe fluid's spreading over completely or a large area; however, with the values higher than 90°, we observe that fluid tries to keep its contact with the surface minimum by lying more compact. With CA values higher than 150°, high repellency between the droplet and the surface is seen and this phenomenon is called as lotus effect and the surfaces are called as super-repellent or for hydrophilic liquids, super-hydrophobic[12]. The main principles of partial wetting were first stated by Wenzel[13] in 1936 and then by Cassie and Baxter[14] in 1944. Wetting state models are schematized in the figure below.

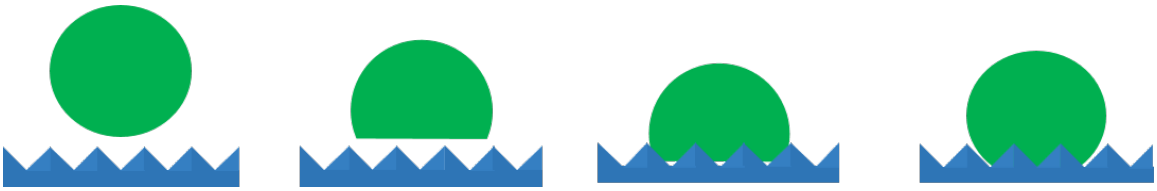

Figure 3.5: Schematic representation of the wetting state models a) the nonwetting; b) the Cassie-Baxter; c) the mixed wetting, and d) the Wenzel

For mid-states, equation 3.1 may not be enough to well-define the cases. Lafuma and Quéré explained all cases in detail in 'Superhydrophobic States'[12].

In Cassie-Baxter Model, drop sits partially on air and partially on the surface letting air can be trapped in between[14]. As the contact angle in this model is average between the value on air and the solid, we must take 'the fraction of solid in contact with the liquid' ($\emptyset_s$) into consideration to calculate the apparent contact angle (θ^*)[12].

$$\cos\theta^* = -1 + \emptyset_s (1+\cos\theta) \qquad \text{Eqn. 3.3}$$

In Wenzel Model, as the droplet is in contact with the surface, the surface roughness *r*, should be included into the calculation to reach apparent contact angle[12].

$$\cos\theta^* = r\cos\theta \qquad \text{Eqn. 3.4}$$

3.1.1.5 Determination of Contact Angle

Contact angle measurement may be a bit tricky due to the effects on the lying drops. As it was mentioned before, contact angle hysteresis causes inaccuracies in the calculations based on Young's equation. Therefore, for an accurate calculation one should take advancing and receding angles into consideration. There are four measurable contact angles one can calculate: θ (Young's equilibrium contact angle), θ_A (Advancing angle), θ_R (Receding angle) θ_{Eq} (Equilibrium contact angle)[15] (Figure 3.6).

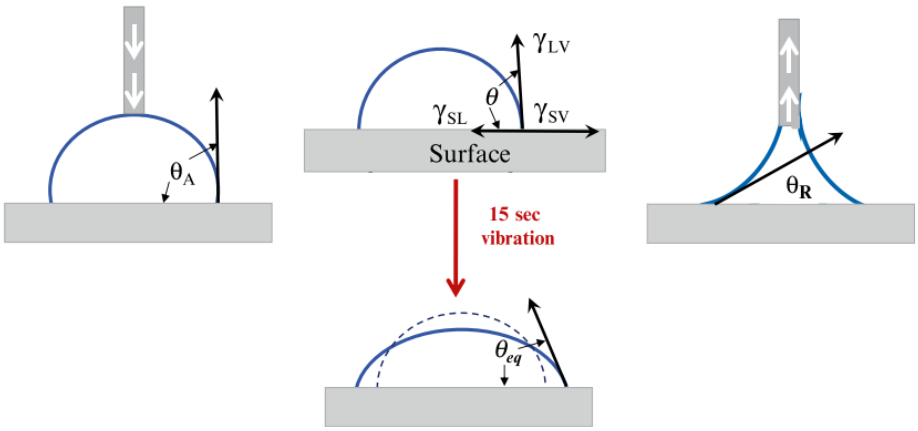

Figure 3.6: Schematic illustration of the four measurable contact angles for a given sessile droplet. Reproduced from ref [15]

θ, θ_A and θ_R were already explained in the previous parts. θ_{Eq}, equilibrium contact angle, was additionally needed to be defined after the observation of the effect of external noise or energy on the contact angle. The change in water contact angles on different surfaces due to the acoustic energy from a loud speaker was observed by Smith and Lindberg[16] in 1978. Their study showed that there are many metastable states between the advancing and the receding angles by observing that the contact angle of water decreases as the input energy increases. 16 years after Smith and Lindberg, Andrieu et. Al.[17] reported de-pinning of the contact angle of water and diiodomethane droplets on different surfaces in the presence of a vertical vibration (50 Hz at variable amplitudes). In 1996, Decker and Gareff shared their observation on probing the energy barrier between the wetting states of advancing and receding angles with vibration[18]. The outcome of their study on the capillary rise of the liquid showed that advancing angle decreases and receding angle increases with increasing input energy. In 2002 Volpe et. Al.[19] studied the relation between the contact angle hysteresis and the input energy by using a microbalance in a Wilhelmy plate set-up. The quantitative definition of the equilibrium contact angle, θ_{Eq} was stated with the contributions of Decker & Gareff[18] and Volpe & coworkers[19] as :

$$\cos \theta_{Eq} = (0.5 \cos \theta_A + 0.5 \cos \theta_R) \qquad \text{Eqn. 3.5}$$

There are several techniques for determination of contact angle including: direct measurement by telescope-goniometer, captive bubble method, tilting plate method, Wilhelmy balance method, capillary rise at a vertical plate, individual fiber, capillary tube, capillary penetration method for powders and granules, capillary bridge method[1,3,15,20].

In general, static contact angle measurement is performed in open lab atmosphere by forming a sessile drop with a micro syringe onto a horizontal solid surface[15] (Figure 3.7).

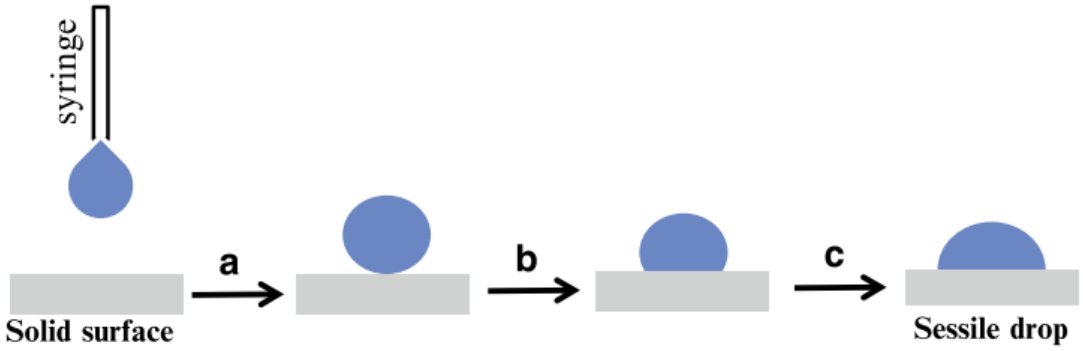

Figure 3.7: Schematic drawing of the formation of a sessile drop during static contact angle measurement a refers to wetting, b and c refer to spreading. Reproduced from ref [15]

3.1.2 Superhydrophobic Surfaces

Superhydrophobic surfaces have gaining more and more interest for the last few decades due to the potential application areas like self-cleaning, nanofluidic, and electrowetting.[3]

3.2 Experimental Preparation

3.2.1 Materials

3.2.2 Preparation of Superhydrophobic Surfaces via Electrochemical Deposition (ECD) Method

90° bent copper surfaces (wxl:1 cmx8 cm) were taken to be used as templates for drying droplet experiments. As the components in the droplets are hydrophobic, to obtain successful lying drops without spreading on the surface, a type of hydrophobic coating was needed to be applied. To do that, the procedure reported by Gu et. Al.[21] was applied with some changes. Copper surfaces were cleaned with steel wool gently. 10mM $AgNO_3$ (~85 mg in 50 ml)

solution was prepared and copper surfaces were immersed into centrifuge tubes separately for 25 minutes at room temperature. The next step was to take the surfaces from $AgNO_3$ solution and let them dry for few minutes, gently washed with dI water to eliminate the residue. To stabilize the Ag coating, 1 mM dodecanethiol (~ 10mg in 50 ml) solution was prepared in toluene for 20 hours. The related reaction of electrochemical deposition of Ag on copper surfaces is given below:

$$Cu + 2\ Ag^{+} \rightarrow 2Ag + Cu^{2+} \qquad \text{Eqn. 3.6}$$

3.2.3 Contact Angle Measurement on the Silver Coated Copper Surfaces

Contact angle measurements were conducted for the investigation of the hydrophobicity of the surfaces. Measurements were done with a Dataphysics OCA 20 at TU Berlin. We chose 3 µl dosing volume and dosing rate as 5.0 µl per second, for dispensing the droplet a Braun 1 ml disposable syringe was used. The images were visualized and analyzed with the software SCA 20. As we used 90° bent surfaces in this study, we took contact angle measurements on bent surfaces. Contact angle was measured as 120±1.4°.

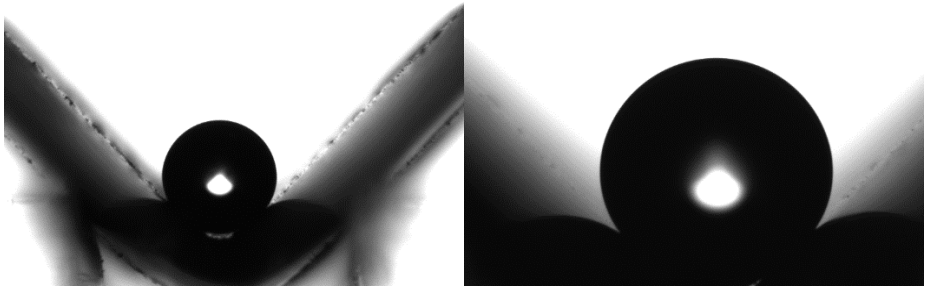

Figure 3.8: Side view of a 3µl water droplet on 90° bent superhydrophobic surface.

As it is seen in the contact angle images taken, water droplet lies on the surface without wetting the surface. It keeps its contact with the surface in minimum.

3.3 Results and Discussion

Preparation of the superhydrophobic surfaces was the very first step of this study. That's why they were the highest importance in this study. These surfaces were used in the following

chapters to prepare the anisometric particles and patchy particles which were the core of this study overall.

By using the method reported by Gu et. Al.[21], we achieved to prepare Ag coating on Cu surfaces with 120° contact angle via CVD method. Surfaces may be damaged after some time (see Figure 3.9) and this could be easily observed while preparing the supraparticles on them. As soon as they were damaged, with the same method surfaces were renewed and used for multiple experiments.

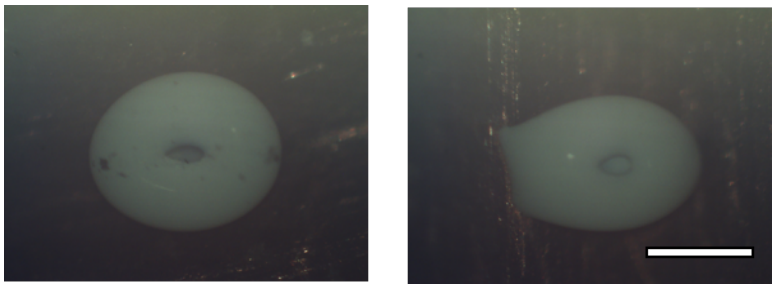

Figure 3.9: Optical microscope images of Fumed Silica based particles (4x) on Left: undamaged and Right: damaged superhydrophobic bent surfaces (Scale bar is 0.5 mm and same for both images)

3.4 References

(1) Hebbar, R. S.; Isloor, A. M.; Ismail, A. F. Contact Angle Measurements. In *Membrane Characterization*; Elsevier B.V., 2017; pp 219–255. https://doi.org/10.1016/B978-0-444-63776-5.00012-7.

(2) Young, T. III. An Essay on the Cohesion of Fluids. *Philos. Trans. R. Soc. London* **1805**, *95* (1), 65–87. https://doi.org/10.1098/rstl.1805.0005.

(3) Yuan, Y.; Lee, T. R. Surface Science Techniques. In *Springer Series in Surface Sciences*; Bracco, G., Holst, B., Eds.; Springer Series in Surface Sciences; Springer Berlin Heidelberg: Berlin, Heidelberg, 2013; Vol. 51. https://doi.org/10.1007/978-3-642-34243-1.

(4) Eral, H. B.; 't Mannetje, D. J. C. M.; Oh, J. M. Contact Angle Hysteresis: A Review of

Fundamentals and Applications. *Colloid Polym. Sci.* **2013**, *291* (2), 247–260. https://doi.org/10.1007/s00396-012-2796-6.

(5) Kwok, D. Y.; Lam, C. N. C.; Li, A.; Leung, A.; Wu, R.; Mok, E.; Neumann, A. W. Measuring and Interpreting Contact Angles: A Complex Issue. *Colloids Surfaces A Physicochem. Eng. Asp.* **1998**, *142* (2–3), 219–235. https://doi.org/10.1016/S0927-7757(98)00354-9.

(6) Tavana, H.; Lam, C. N. C.; Grundke, K.; Friedel, P.; Kwok, D. Y.; Hair, M. L.; Neumann, A. W. Contact Angle Measurements with Liquids Consisting of Bulky Molecules. *J. Colloid Interface Sci.* **2004**, *279* (2), 493–502. https://doi.org/10.1016/j.jcis.2004.06.090.

(7) De Souza, E. J.; Gao, L.; McCarthy, T. J.; Arzt, E.; Crosby, A. J. Effect of Contact Angle Hysteresis on the Measurement of Capillary Forces. *Langmuir* **2008**, *24* (4), 1391–1396. https://doi.org/10.1021/la702188t.

(8) He, B.; Lee, J.; Patankar, N. A. Contact Angle Hysteresis on Rough Hydrophobic Surfaces. *Colloids Surfaces A Physicochem. Eng. Asp.* **2004**, *248* (1–3), 101–104. https://doi.org/10.1016/j.colsurfa.2004.09.006.

(9) Deegan, R. D.; Bakajin, O.; Dupont, T. F.; Huber, G.; Nagel, S. R.; Witten, T. A. Capillary Flow as the Cause of Ring Stains from Dried Liquid Drops. *Nature* **1997**, *389* (6653), 827–829. https://doi.org/10.1038/39827.

(10) Deegan, R. D.; Bakajin, O.; Dupont, T. F.; Huber, G.; Nagel, S. R.; Witten, T. A. Contact Line Deposits in an Evaporating Drop. *Phys. Rev. E* **2000**, *62* (1), 756–765. https://doi.org/10.1103/PhysRevE.62.756.

(11) ZISMAN, W. A. Relation of the Equilibrium Contact Angle to Liquid and Solid Constitution. In *Contact Angle, Wettability, and Adhesion*; American Chemical Society: Washington, DC, 1964; pp 1–51. https://doi.org/10.1021/ba-1964-0043.ch001.

(12) Lafuma, A.; Quéré, D. Superhydrophobic States. *Nat. Mater.* **2003**, *2* (7), 457–460.

https://doi.org/10.1038/nmat924.

(13) Wenzel, R. N. Resistance of Solid Surfaces to Wetting by Water. *Ind. Eng. Chem.* **1936**, *28* (8), 988–994. https://doi.org/10.1021/ie50320a024.

(14) Cassie, A. B. D.; Baxter, S. Of Porous Surfaces,. *Trans. Faraday Soc* **1944**, No. 5, 546–551. https://doi.org/10.1103/PhysRevE.64.021514.

(15) Law, K. Y.; Zhao, H. *Surface Wetting: Characterization, Contact Angle, and Fundamentals*; Springer, 2015. https://doi.org/10.1007/978-3-319-25214-8.

(16) Smith, T.; Lindberg, G. Effect of Acoustic Energy on Contact Angle Measurements. *J. Colloid Interface Sci.* **1978**, *66* (2), 363–366. https://doi.org/10.1016/0021-9797(78)90318-1.

(17) Andrieu, C.; Sykes, C.; Brochard, F. Average Spreading Parameter on Heterogeneous Surfaces. *Langmuir* **1994**, *10* (7), 2077–2080. https://doi.org/10.1021/la00019a010.

(18) Decker, E. L.; Garoff, S. Using Vibrational Noise to Probe Energy Barriers Producing Contact Angle Hysteresis. *Langmuir* **1996**, *12* (8), 2100–2110. https://doi.org/10.1021/la951021n.

(19) Volpe, C. Della; Maniglio, D.; Morra, M.; Siboni, S. The Determination of a "stable-Equilibrium" Contact Angle on Heterogeneous and Rough Surfaces. *Colloids Surfaces A Physicochem. Eng. Asp.* **2002**, *206* (1–3), 47–67. https://doi.org/10.1016/S0927-7757(02)00072-9.

(20) Erbil, H. Y. *Surface Chemistry of Solid and Liquid Interfaces*; Blackwell Publishing, 2006; Vol. 9. https://doi.org/10.1002/cphc.200700726.

(21) Gu, C.; Ren, H.; Tu, J.; Zhang, T. Y. Micro/Nanobinary Structure of Silver Films on Copper Alloys with Stable Water-Repellent Property under Dynamic Conditions. *Langmuir* **2009**, *25* (20), 12299–12307. https://doi.org/10.1021/la902936u.

CHAPTER 4: ANISOMETRIC FS-BASED PARTICLES

Scope of the Chapter:

In this chapter, we present a system to prepare sub-millimeter sized anisometric supraparticles. These particles that contain as structural main component fumed silica (FS), are prepared on superhydrophobic surfaces. By using the idea of controlling the anisometry of the particles in a systematic fashion via ionic strength of the FS solutions, we established a system with FS and different electrolytes NaCl, NaF and Spermine. In addition to different electrolytes, PEG was another additive used here to investigate the effect of PEG with different chain length/molecular weight on the physical properties of the dry particles and mechanical stability which would be necessary in the next steps. In this study, both the effect of electrolyte and the surface area of FS on anisometry of the dried particles were investigated. Having particles with tunable anisometry, our aim was to go one-step further, which is the application of these anisometric supraparticles for self-propulsion. Next steps will be discussed in Chapter 5 and Chapter 6 in detail.

4.1 Introduction

Colloidal building blocks based mesoscopic structure formation has been gaining more interest in the last decades due to various potential advanced applications.[1] With this approach, a new perspective appeared: fabrication of new materials like well-defined hierarchically structured supraparticles.[2] These well-defined hierarchically structured supraparticles, with the possibility of tunable composition and structure, could be used as smart and functional materials.[1–6] Various potential application areas of these supraparticles include catalysis,[7,8] thermo- or magneto-sensitive materials,[9–11] lithography,[12,13] microfluidics,[14,15] photonics[9,16–19] or sensing.[20,21]

To synthesize such colloidal assemblies, the main techniques widely used in literature are microfluidics,[16,22,23] spray-drying,[17,18] or evaporation induced self-assembly (EISA).[24,25] Self-assembly or self-organization, is a reversible process of a spontaneous arrangement of initially disordered distinct components into ordered structures[26] through noncovalent interactions[27]. The EISA method is based on self-assembling of the structures during evaporation and it enables formation of spherical particles as a result of droplet templating on superhydrophobic

surfaces with contact angles greater than 150°.[3] When colloidal mixtures go through an evaporation procedure, the colloids in the mixture become assembled under the control of the interaction between colloids. As an internal structure of the supraparticles is formed during the process of colloidal assembly, this method allows to produce 3D-colloidal assemblies of supraparticles with well-defined structues.[28–31] With this approach it is possible to obtain not only symmetric spherical supraparticles[3] but also "doughnut" particles[30,32] by taking the advantage of the coffee-ring effect on suspension drying.[33,34] Doughnut particle formation was achieved with silica microspheres having different concentrations.[30] The hole size of the doughnut particles is inversely proportional to the initial colloidal concentration. In fact, it is not easy to control the shape of supraparticles. However, there is a simple way to obtain anisometric particles with lower but controlled symmetry achieved by Sperling et. al.[31] For the case of fumed silica as dispersed colloid they reported the method of controlling the shape of the evaporating droplets via ionic strength, and observed that anisometry of the particles increases with increasing electrolyte concentration.

4.2 Experimental

4.2.1 Materials

Materials	Specifications	Supplier
Fumed silica (FS) AEROSIL® 90	surface area=90 ± 15 m^2/g	Evonik
Fumed silica (FS) AEROSIL® 200	surface area=200 ± 25 m^2/g	Evonik
Fumed silica (FS) AEROSIL® 300	surface area=300 ± 30 m^2/g	Evonik
NaCl	synthesis-grade, ≥ 99.9%	ChemSolute
NaF	99.99%	Sigma-Aldrich
(3-Aminopropyl)triethoxysilane	99%	Sigma-Aldrich
Acetic Acid	≥99.5%	Sigma-Aldrich
Polyethylene Glycol 400	synthesis grade	Merck
Polyethylene Glycol 6000	synthesis grade	Merck
Spermine	≥99.0%	Sigma-Aldrich
MiliQ water	≥ 18 MΩ/cm	

4.2.2 Preparation of Fumed Silica Suspensions

Fumed silica (FS) powders with different surface areas (S.A.: 90, 200, 300 m^2/g) were provided from Evonik. To investigate other properties like radius and diffusion coefficients of the samples, DLS [ALV/CGS-3 Compact Goniometer (with ALV/LSE 5004 Correlator) with a He-Ne laser; for details see Chapter 2.3] was used. Measurements were taken at room temperature and λ=633 nm. 0.035 %w/v of FS dispersions were used to conduct DLS measurements and cumulant hydrodynamic radii of the FS samples were found in between 118, 127 and 138 nm for FS_90, FS_200 and FS_300, respectively. With the intensity data obtained from SLS measurement, we were able to calculate molecular weight and by using the Guinier approximation, I_0 and R_g were calculated. [Data treatment was performed by MSc physicist Benjamin von Lospichl with a script he developed himself[35]]. Detailed outcome of DLS&SLS measurement was given in the table below.

Table 4.1: Results from SLS and DLS for 0.035 % w/v FS suspensions.

Sample	D_{coll} ($\mu m^2/s$)	R_h (nm)	R_g (nm)	PDI	M_{Wt} (g/mol)	I_0 (cm^{-1})
FS_90	2.08	118.11±0.70	118.77±4.02	0.193	2.04 x	0.117±0.007
FS_200	1.92	127.51±0.88	124.88±2.40	0.246	1.38 x	0.079±0.003
FS_300	1.78	138.02±0.84	120.95±4.24	0.301	8.88 x	0.051±0.003

Molecular weight of the samples was calculated by using the formula given below:

$$M_{w,eff} = \frac{N_{Av}.\lambda^4.R_{\theta=0}}{2.\pi^2.c_g.n^2.(dn/dc_g)^2} \qquad \text{Eqn. 4.1}$$

where $R_{\theta=0}$ is the Rayleigh Ratio, dn/dc is the refractive index increment, which is estimated as 0.15 here, N_{Av} is the Avogadro constant, λ the wavelength of the laser, n is the refractive index of the solvent and c_g is the mass concentration of the solute.

Preparation of FS suspensions was simply done by preparing dispersions of FS in deionized water and dilution to the desired concentration. To do that, first a concentrated stock solution of fumed silica (FS) (~0.3 g FS in 75 ml deionized water) was prepared by dispersing FS powders in deionized water. The suspensions were stirred for 3 hours at 1200 rpm with a

centrifuge [Hettich Universal 320 R] at room temperature. Then, the suspensions were centrifuged (20 minutes at 5000 rpm) to obtain a concentrated solution (concentration ~10-15 % wt/v), which then was diluted to 7% wt/v. The resultant solution was slightly acidic with pH 5.7 and milky looking.

4.2.3 Amine Functionalization of FS_90 Powder: Synthesis of FS_90@NH_2

0.5 g of Acetic acid and 0.5 g of APTS were mixed and dropwise added in 10 min to 2 ml of 7% wt/v FS_90 suspension in 2 ml of miliQ water. Then the reaction mixture was let stirring for overnight at 70 ˚C with 550 rpm on a magnetic stirrer. FS_90@NH_2 dispersion was then purified via dialysis in a 1 L beaker with MiliQ water (pH value was adjusted with AA to 3-4 for stability of the dispersion) and the dialysis system was renewed daily for a total of five times.

4.2.4 Preparation of FS-based Supraparticles

FS suspensions were 50:50 mixed with electrolyte solutions and templated on superhydrophobic surfaces. 3 µl droplets of 50:50 FS & electrolyte mixtures were templated on 90˚ bent superhydrophobic surfaces (see Figure 4.1) in a closed chamber and they were let dry for around 30-40 minutes at room temperature under 5% humidity. By using bent surface, we were able to control the direction of anisometry of the dried supraparticles.

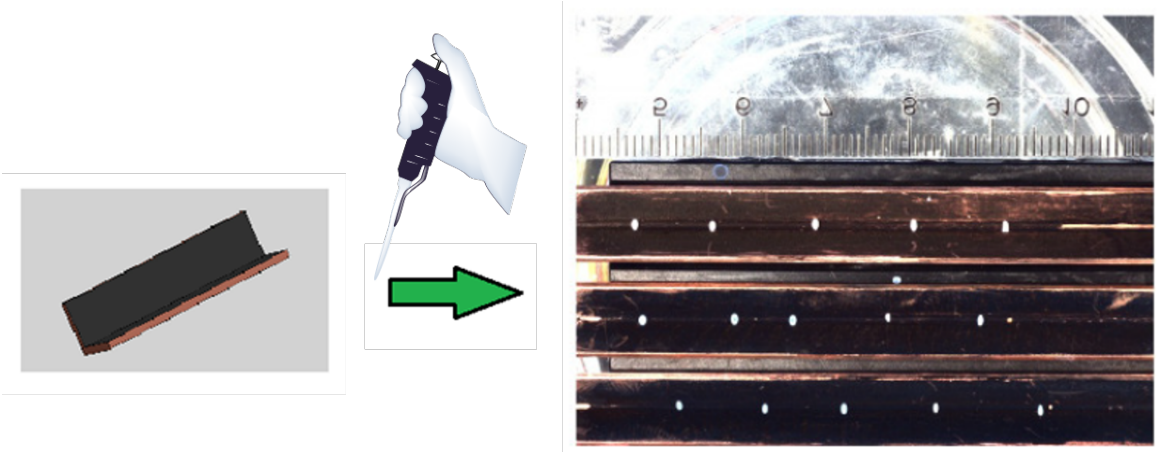

Figure 4.1: Schematic illustration of droplet templating on superhydrophobic surfaces

Dried FS particles were analyzed with an optical microscope to calculate anisometry and to do that we used an USB-cam DFK 72AUC02 connected Carl Zeiss Jenapol Optical Microscope using a Planchromat LD 4x objective at the TU Berlin. To record the images and calculate the anisometry of the particles IC-Capture Software and Fiji/Image J Software was used respectively[36]. For optical measurements conducted in NCSU, a BX61 Olympus Optical Microscope was used.

Anisometry could be simply defined as the ratio of the long (D_l) to short (D_w) diameters of an object. By using this definition, anisometry calculations were done (see Figure 4.2) by using the equation:

$$A = \frac{D_l}{D_w} \qquad \text{Equation 4.2}$$

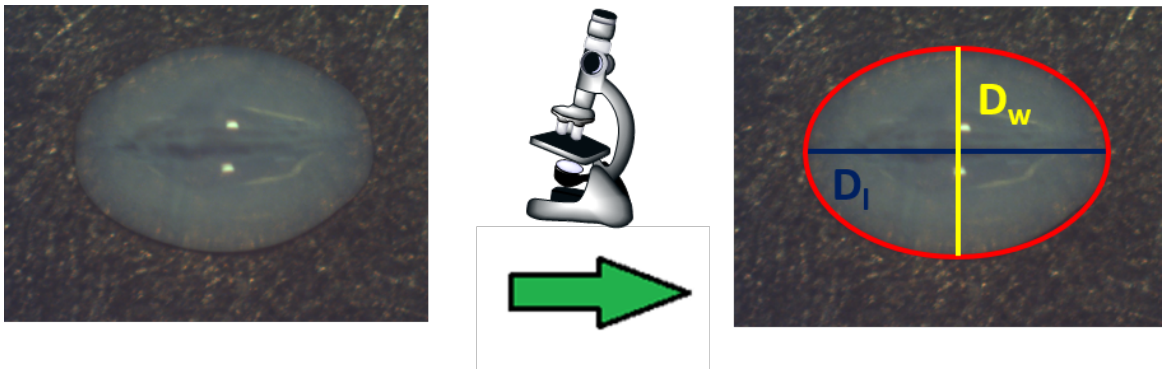

Figure 4.2: Illustration of anisometry calculation

4.3 Results and Discussion

As it was previously explained, obtaining FS-based particles with tunable anisometry in a systematic fashion was the aim of the section in this study. By knowing that NaCl has a systematic effect on the anisometry of sub-mm FS-based particles for FS_400, we would like to see its effect on the particles prepared with different fumed silica suspensions (Surface Areas: 90, 200 and 300 m^2/g) and we established a system with NaCl and FS (4.3.1). In addition to NaCl, by being a monovalent salt NaF was also tried to see the difference between salts (4.3.2). After performing monovalent electrolytes, we decided to investigate the effect of a multivalent electrolyte on the anisometry of the dry particles, therefore we conducted same experiments under same conditions with spermine (4.3.5). By thinking about the following

steps of this study, in addition to different electrolytes, PEG was added to FS suspension in absence and presence of NaCl to observe its effect on both physical and mechanical properties of the dry particles (4.3.3 & 4.3.4)

4.3.1 Effect of NaCl on Anisometry of FS-based Supraparticles

In this sub-section, FS-NaCl based particles prepared with 3 different FS suspensions having surface areas 90,200 and 300 m^2/g. Besides the effect of NaCl, the effect of surface area of FS on the anisometry of the particles was also investigated by using FS_90, FS_200 and FS_300. For this sake, prepared FS-NaCl based particles were analyzed under an optical microscope with 4x magnification to calculate anisometry. For NaCl we scan the range 0.02 mM- 50 mM, and for FS, as it was mentioned before, concentration was fixed to 7% w/v. Microscope images of dried particles were given in the figure below. For each FS type (90,200 and 300), we scanned the range 0.02 mM-50mM NaCl. To make the calculations, 15-20 particles of each combination (i.e. FS_90 & 1.0 mM NaCl) were prepared and analyzed under optical microscope. The anisometry of all particles were calculated and average value was taken to be reported in Figure 4.4.

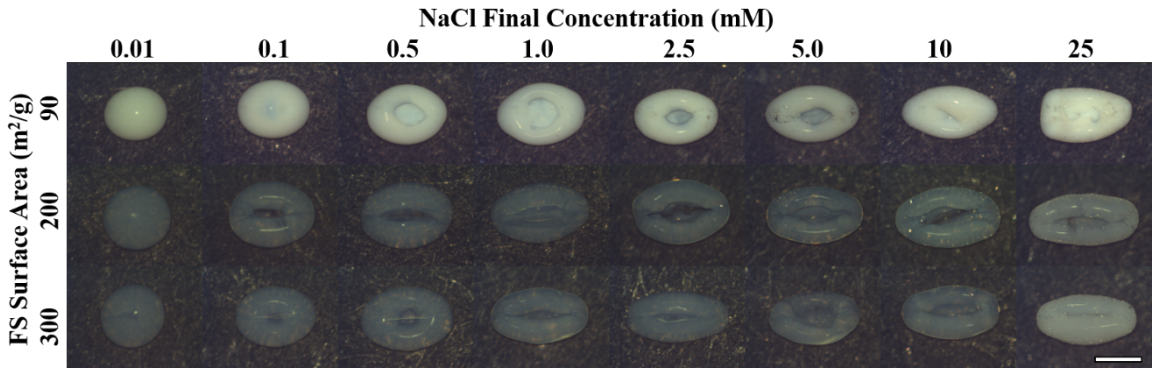

Figure 4.3: Microscope images of dried particles (row: Final concentrations of the silica suspension and NaCl solution mixture / Column: Surface area of the particles; scale bar: 1mm)

As clearly seen in the Figure 4.3 above, the anisometry increases with the increase in NaCl concentration. When the FS suspension is mixed with 0.02 mM NaCl solution (0.01 mM final concentration in the particle), dried particles are nearly spherical; however, at 50 mM NaCl concentration (25 mM final concentration in the particle), supraparticles show high anisometric

tendency during drying. Additionally, it was observed that the anisometry increases with increasing surface area of FS. Qualitative data is shown in the graph below, anisometry vs NaCl % wt/v in the colloidal mixture.

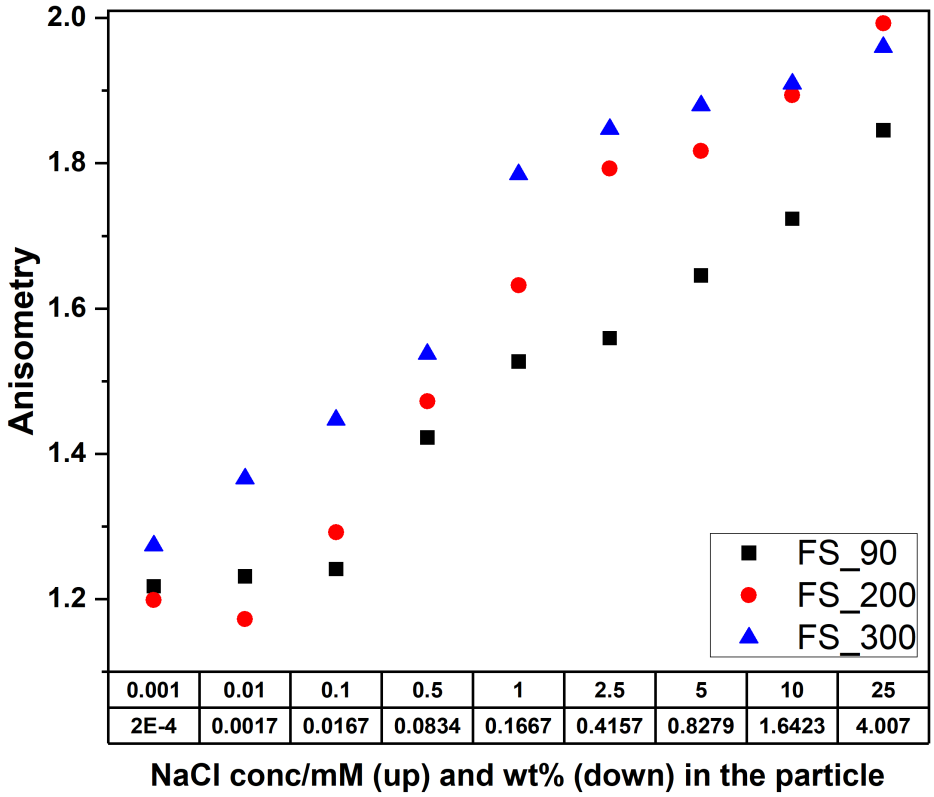

Figure 4.4: Anisometry of the particles with respect to NaCl concentration and % wt/v in the particles

The anisometry values for FS_90 based particles (FSP1) were calculated to be between 1.20 to 1.84, for FS_200 based particles (FSP2) between 1.20-1.90 and for FS_300 based particles (FSP3) between 1.30-1.90. For the same type of FS, anisometry is prone to increase with increasing electrolyte concentration. Previously in Sperling et. al.[31], the effect of electrolyte on anisometry of FS-NaCl supra-particles was investigated. In the study, three FS_400 dispersions (PDI: 0.2-0.4 and r: 150 nm) with 3.5, 7 and 10.5 % wt/v were mixed with NaCl solutions with concentration changing between 0.001 and 100mM. It was observed that up to 25 mM (Average anisometry at 25 mM: 1.6), particles` anisometry increases linearly, with

NaCl solutions having concentration above 25 mM, the degree of anisometry either does not show any increase or even decreases for some particles. Here in our study, we investigated both the effect of electrolyte concentration and of the surface area of the Fumed Silica. The results of these studies were found as qualitatively parallel with respect to anisometry increase with the increase in electrolyte concentration. Maximum anisometry values reached in our study were around 1.8-1.9 and observed at 25 mM. Above 25 mM, dried particles showed anisometry increasing linearly different from the previous studies, however particles became more fragile due to the high salt content (see Figure 4.5). As a summary for this subsection; by playing with the concentration of electrolyte, one can be able to obtain FS particles with desired shape, either spherical or elliptic. The droplets prepared with NaCl concentration lower than 0.1 mM or without NaCl, they end up with spherical particles when they dry. Besides that, droplets prepared with NaCl concentration higher than 0.1 mM, elliptic particles are formed. Talking about the surface area of FS suspensions we could conclude that at the same electrolyte concentration, anisometry is increasing with increasing surface area of FS; however, this change is not as significant as the one caused by electrolyte concentration.

4.3.1.1 Control of Electrolyte Concentration

Obtaining controllable FS-based anisometric particles was the base study for the next step, which is achieving stable anisometric patchy supraparticles to be used for self-propulsion. The concentration of electrolyte to obtain tunable anisometric compact supraparticles is a crucial parameter to be considered.

As it was stated before, the effect of NaCl at 0.002 mM on anisometry is nearly invisible as the shape of dried supraparticles is always spherical. On the other hand, when the final NaCl concentration in the particle is higher than 100 mM, a non-controllable tendency for anisometry occurs and particles become more fragile due to increase in salt crystals inside the particles (see Figure 4.5).

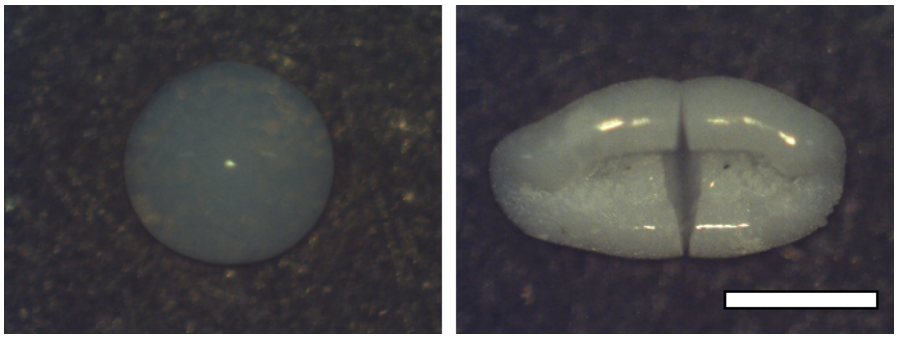

Figure 4.5: Examples of FS_200-NaCl particles with Left: 0.001 and Right: 100 mM final NaCl concentration (scale bar: 1 mm)

FS-NaCl based controllable anisometric particles were successfully obtained and it was observed that they are good candidates for patchy anisometric supraparticles. The first important parameter is electrolyte concentration. For self-propulsion purposes, particles should be anisometric and stable. Therefore, we preferred to keep electrolyte concentration between 0.1 and 25 mM for patchy anisometric particle preparation, which will be explained in detail in the following chapter.

4.3.2 Effect of NaF on Anisometry of FS-based Supraparticles

To investigate the effect of other electrolytes on the anisometry of the FS-based particles, FS-NaF based particles were prepared by following the same steps as in the NaCl case in the previous section. Obtained particles were analyzed with an optical microscope with 4x magnification and anisometry values of the particles were calculated by analyzing images with the software Image J. We scanned the range 0.02 mM-200 mM NaF (initial concentration) and concentration of FS was fixed to 7% wt/v and FS-NaF based supraparticles (see Figure 4.6) were prepared with NaF and FS_90, FS_200 and FS_300 and as in NaCl case, NaF and FS were mixed 1:1 with respect to volume. Anisometry values of all particles (FS-90/200/300 and 0.002-0.02-0.2-1.0-2.0-5.0-10.0-50.0-100.0-200.0 mM NaF) were calculated and the average value was taken to be reported.

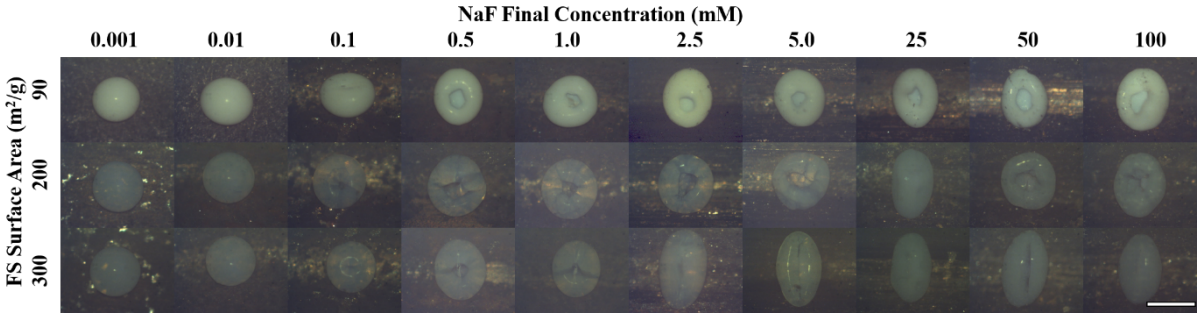

Figure 4.6: Microscope images of dried particles (row: Final concentrations of the silica suspension and NaF solution mixture / Column: Surface area of the particles; scale bar: 1mm)

Particles based on fumed silica and NaF did not show a regular change in anisometry with increasing NaF concentration. Anisometry values of FS_90 and FS_200 particles were low and close together. In contrast, FS_300 particles showed a very dramatic increase at 2.5 mM NaF (final concentration-0.3 wt%) and kept high anisometry at all NaF concentrations above 2.5 mM (see Figure 4.7).

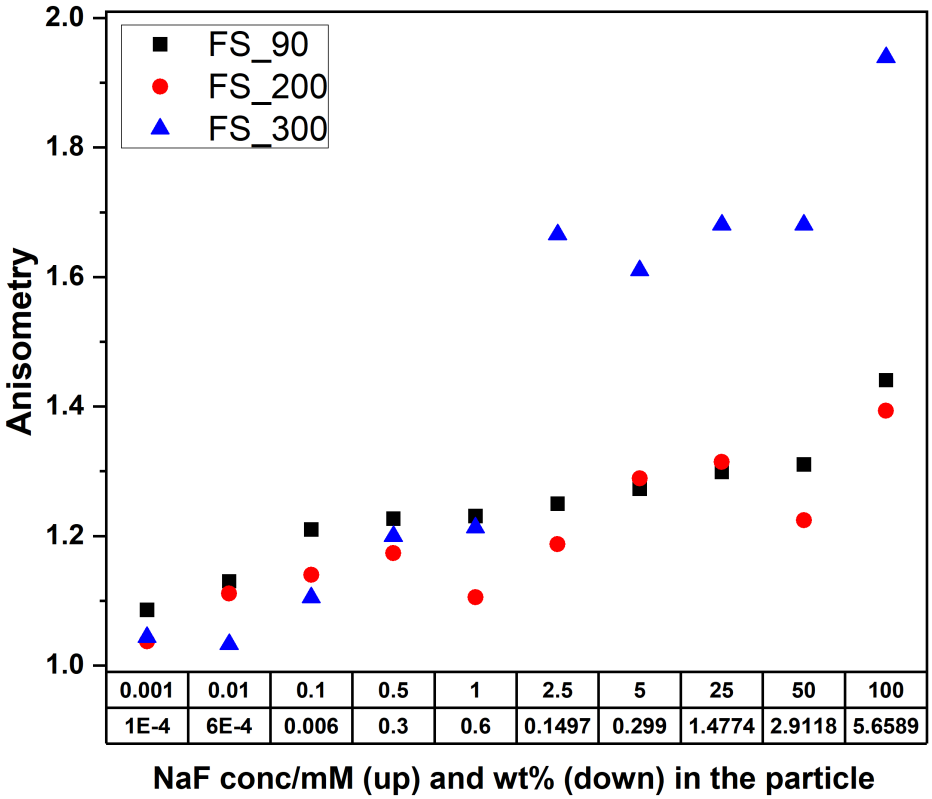

Figure 4.7: Anisometry vs concentration and % wt/v of NaF in the particles

Anisometry values were calculated in between 1.0-1.4 for FS_90 and FS_200 particles, whereas in between 1.0-2.0 for FS_300 particles. Different from NaCl based particles, NaF based particles did not show a FS surface area dependent behavior. NaF-FS_300 particles showed very high anisometry values by rising to 1.9 compared to FS_90 and FS_200 as it was observed that being very close, FS_90 and FS_200 based particles reached 1.4 at highest NaF concentrations. The particles prepared with NaF do not show a regular trend with respect to the electrolyte concentration as in NaCl case. Therefore, FS-NaF particles were not thought as good candidates for self-propelling patchy particles and they were not used for further improvement.

4.3.3 Effect of Polyethylene Glycol on Anisometry of FS-based Supraparticles

In addition to electrolytes, NaCl and NaF, some preliminary research was conducted with polyethylene glycol (polyethylene oxide) (PEG) to investigate the effect of PEG on FS-based

particles. By having various PEG samples with average molecular weight (M_n) changing from 400 to $2x10^6$ units, we prepared 0.35% wt, 0.035% wt and 0.0035% wt solutions of all PEG samples available. However, the samples with molecular weight higher than 6000 were quite difficult to mix with FS suspensions as PEG solutions were not easily drawn with a pipette. For that purpose, we prepared 0.35%, 0.035% and 0.0035% wt PEG 400 and PEG 6000 solutions. Prepared polymer solutions were added to previously prepared 7% wt/v FS colloidal mixtures (1:1) and 3 µl droplets of 1:1 FS&PEG were templated on superhydrophobic surfaces in a closed chamber for evaporation. Dry particles then were taken to be analyzed under optical microscope to calculate anisometry of the particles. For each combination of FS&PEG, 15-20 particles were prepared as in previous sections and the average values were taken to be reported. The outcome of the anisometry calculations were drawn and illustrated below.

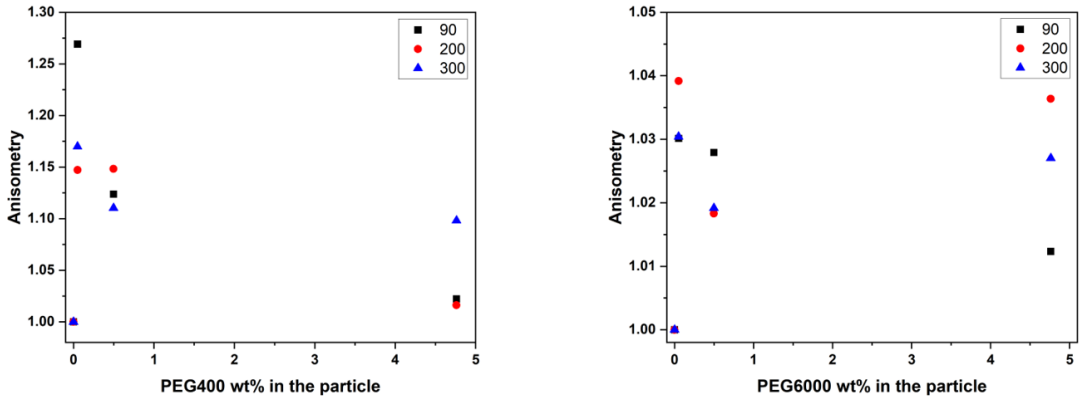

Figure 4.8: Left: Anisometry vs PEG400 wt% (in the particle) and Right: Anisometry vs PEG6000 wt% (in the particle) for FS_90, FS_200 and FS_300 based particles.

As it is seen in the graphs above, there is not any pronounced effect of PEG on the anisometry of the particles. For the particles, in which PEG400 was used, anisometry values were calculated in between 1.0-1.30; whereas for the particles prepared with PEG6000, anisometry values were calculated in between 1.0-1.04. The outcome does not show any regular effect of PEG 400 and PEG6000 on the anisometry of FS-based particles. However specifically, the particles with PEG400 showed more anisometry when compared to the particles with PEG6000 (see Figure 4.9). This may be caused by the molecular weight of PEG samples. By having lower molecular weight, PEG400 has higher mobility and lower viscosity compared to

PEG6000. Therefore, PEG6000 forms bigger agglomerates during evaporation leading to fast contraction of the particle. When looking at the same sample with different concentrations, similar effect of molecular weight is seen, in other words, particles with higher PEG concentration have lower tendency to elongate while drying, compared to the particles with lower PEG concentration.

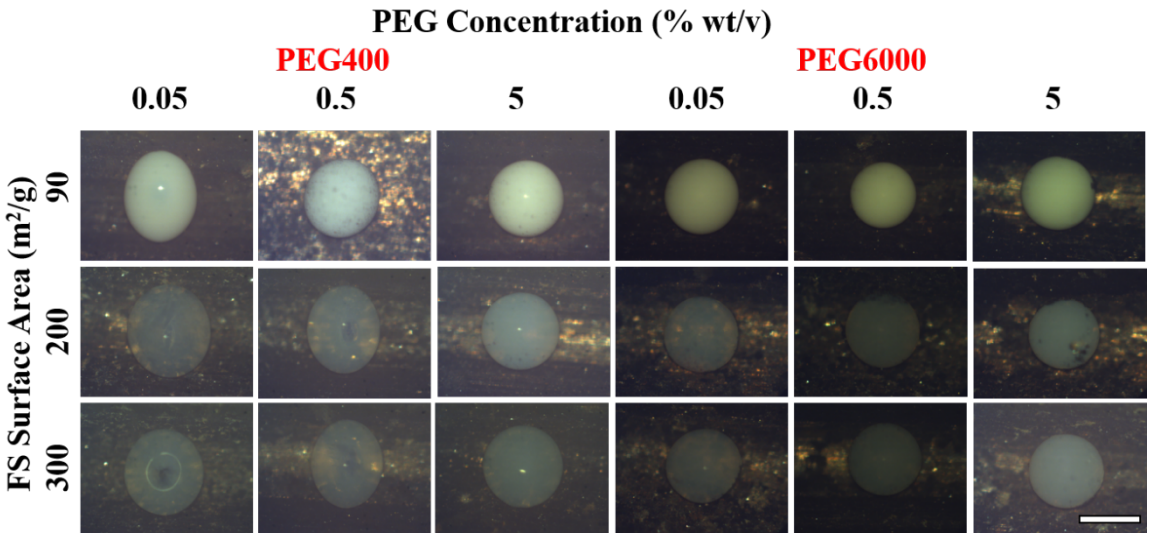

Figure 4.9: Microscope images of FS-PEG based dried particles (scale bar: 1mm)

As seen in the Figure above, PEG600 based particles dries as spheres regardless of PEG concentration. For PEG400 based particles, we observed some anisometry while PEG concentration decreases. With the anisometry, doughnut particle formation was also seen for PEG400 based particles. Doughnut formation is more visible for the particles with higher surface area of fumed silica due to the transparency of FS_200 and FS_300 based dried supraparticles.

4.3.4 Investigation of the Effect of Combination of Polyethylene Glycol 400 and NaCl on Anisometry of FS-based Supraparticles

By knowing that NaCl has a distinct effect on the anisometry of the particles, we decided to add NaCl and PEG400 together in the colloidal mixture. Independent of the concentration of PEG, dried particles always appeared as spheres with higher molecular weight of PEG (PEG6000). That's why we chose PEG400 for the investigation of the effect of PEG when used with electrolyte on FS-based system. In order to observe any interesting morphological

property, we decided to keep NaCl concentration as 100 mM. As in the previous sections, three types of FS were used, FS_90, FS_200 and FS_300. Four PEG400 solutions were prepared with 0.02%, 0.04%, 1.4% and 2.8% wt/v and added into the colloidal mixture. The volume of FS was fixed to 50% in the colloidal mixture as in previous cases and the volume was kept 25% for NaCl and PEG. As observed in the previous section, the higher the concentration of PEG, the more contraction observed during evaporation. For the particles prepared here the same phenomenon was observed, at high PEG concentrations, particles dry as compact nice spheres and at low PEG concentrations, they dry as nice elliptical particles. As observed in section 4.3.1, the opacity of the FS-based particles decreases as surface area of the FS samples increases, in other words FS_300 based particles are more transparent when compared to FS_200 and FS_90 based particles are opaque (see Figure 4.3). By using the advantage of different optical properties of FS samples, we obtained nice mottled FS_300-PEG400 particles (see Figure 4.10).

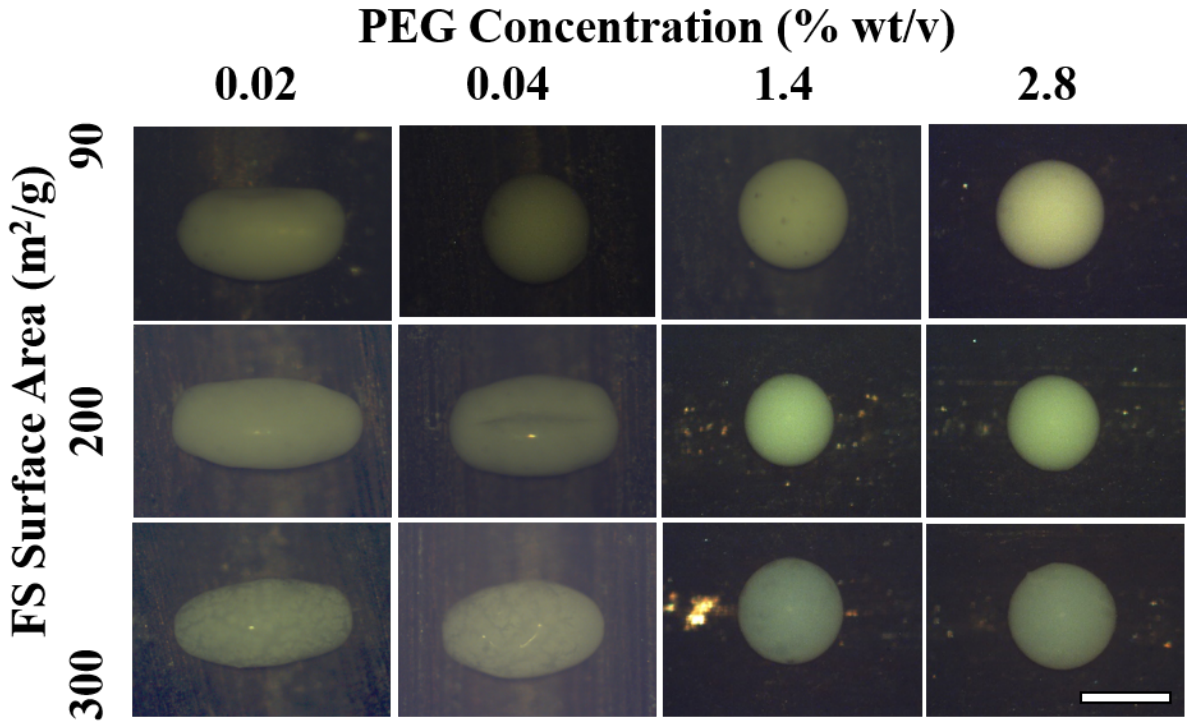

Figure 4.10: Microscope images of FS-NaCl-PEG400 based dried particles (scale bar: 1mm)

FS-PEG based particles showed anisometry at low PEG concentrations and they dried as homogeneous spheres at high PEG concentrations. This phenomenon was observed in the previous section with different types of PEG in the absence of electrolyte. Here, for the particles prepared with PEG and electrolyte at low PEG concentrations, dried particles show anisometry and the trend is same as in NaCl case, anisometry increases with increase in surface area of the FS. However, it was observed that anisometry decreases with increasing surface area of FS at high PEG concentrations. The outcome is illustrated in the figure below.

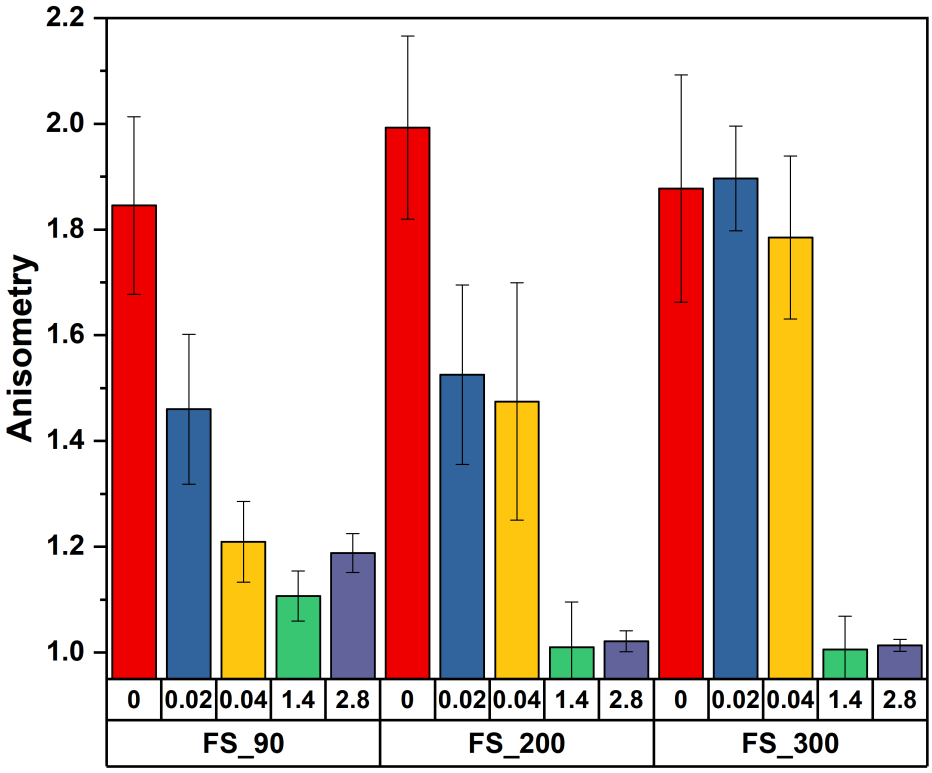

Figure 4.11: Anisometry bars of the FS-PEG particles prepared with NaCl.

In the Figure 4.11, the outcome of anisometry calculations was drawn. Gray, red, green and blue columns represent 0.02% PEG (0.14% wt in dried particle), 0.04% PEG (0.27% wt in dried particle), 1.4% PEG (8.76% wt in dried particle) and 2.8% PEG (16.11% wt in dried particle) respectively. Anisometry values were calculated as 1.46 and 1.19 for FS_90, 1.53 and 1.02 for FS_200, 1.89 and 1.01 for FS_300 particles. As it was mentioned before, anisometry

of the particles increase with increasing surface area at low PEG concentration, whereas anisometry decreases with decreasing surface area at high PEG concentration but this decrease is not very significant compared to the increase.

4.3.5 Investigation of the Effect of Spermine as an Electrolyte on Anisometry of FS-Based Particles

In addition to the monovalent NaCl and NaF, as a multivalent electrolyte, the effect of spermine (1,12-diamino-4,9-diazadodecane) on the anisometry of FS-based particles was investigated. Spermine, being a tetravalent electrolyte, could be a good candidate for the observation of multivalent electrolyte on the anisometry of the fumed silica-based particles. Spermine and spermidine are naturally occurring polyamines bearing nucleic acid binding and transfection activity[37,38]. By knowing that spermine stays as tetravalent cation at basic pH values to physiological conditions due to its strongly basic character[37,38], we ensured that anisometry of the particles in our system would be affected by a tetravalent electrolyte. pH values of the spermine solutions prepared were measured (Mettler Toledo FP20 FiveEasy™ Plus pH / mV bench meter) and tabulated with FS and FS@NH_2 below (see Table 4.2). The colloidal mixture of FS/FS@NH_2 with spermine was not appropriate for pH measurement due to its turbidity. However, one could clearly mention that the pH of the colloidal mixtures could not decrease below to physiological pH even at the lowest concentration of spermine as spermine is a strong base whereas fumed silica would act as a weak base.

Table 4.2: pH values of Spermine solutions and FS&Spermine mixtures used in this section

Spermine		FS&Spermine (10x diluted)
Conc mM	**pH**	**pH**
0.4	8.07	7.43
1.0	8.12	7.48
50	11.73	10.59
100	11.83	10.92
200	11.95	11.18
400	12.09	11.46

The same procedure was applied for spermine as in NaCl and NaF cases, i.e. 0.4 mM to 400 mM solutions of spermine were prepared and added to 7% w/v FS_90 suspensions with the ratio of 50:50. Then 3 µl droplets of the colloidal mixture were templated on superhydrophobic surfaces. After around 40 mins dried particles were investigated under optical microscope. We had chosen the same conditions in order to compare the data and to see the differences of the effect of different electrolytes on the anisometry of the FS-based particles.

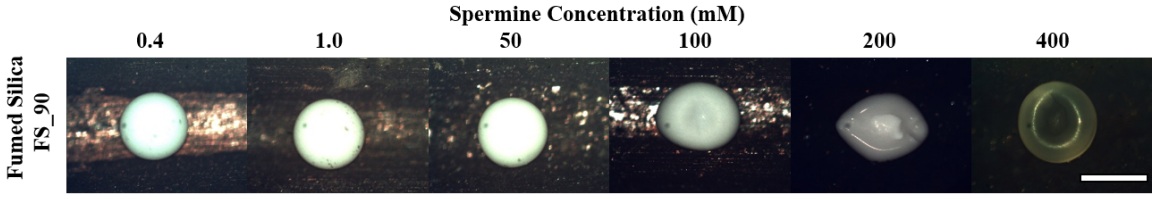

Figure 4.12: Microscope images of FS_90-Spermine based dried particles (scale bar: 1mm)

Dried FS_90-Spermine particles were analyzed by optical microscopy (Figure 4.12). Interestingly, there was not any pronounced effect of spermine observed on anisometry of the particles in the range of 0.4 mM – 50 mM, and the particles prepared with 100, 200 and 400 mM solutions showed some anisometry, but the shapes and the colors of the particles look different. On the other hand, the particles prepared with 400 mM spermine solution showed very interesting results. The particles prepared with 400 mM spermine solutions were dried as

doughnuts having yellowish transparent or bluish transparent colors (see Figures 4.12 and 4.14). The time spent for the particles to dry completely reached around 2 hours, while it was around 40 min for the supraparticles prepared in previous sections with NaCl or NaF. Additionally, it was observed that some of the obtained dried particles were sticky like slime which also affects the morphology of the supraparticles. To obtain well-defined supraparticles with spermine, we decided to use more concentrated spermine solutions and meanwhile we tried amine functionalized FS. For that purpose, we chose FS_90 only for a preliminary study and 200 mM and 400 mM (100 and 200 mM in the final colloidal mixture of FS-Spermine) spermine solutions were mixed with both FS_90 and FS_90@NH_2 in 50:50 ratio. [The synthesis method for FS_90@NH_2 was previously explained in the section 4.2.3.]

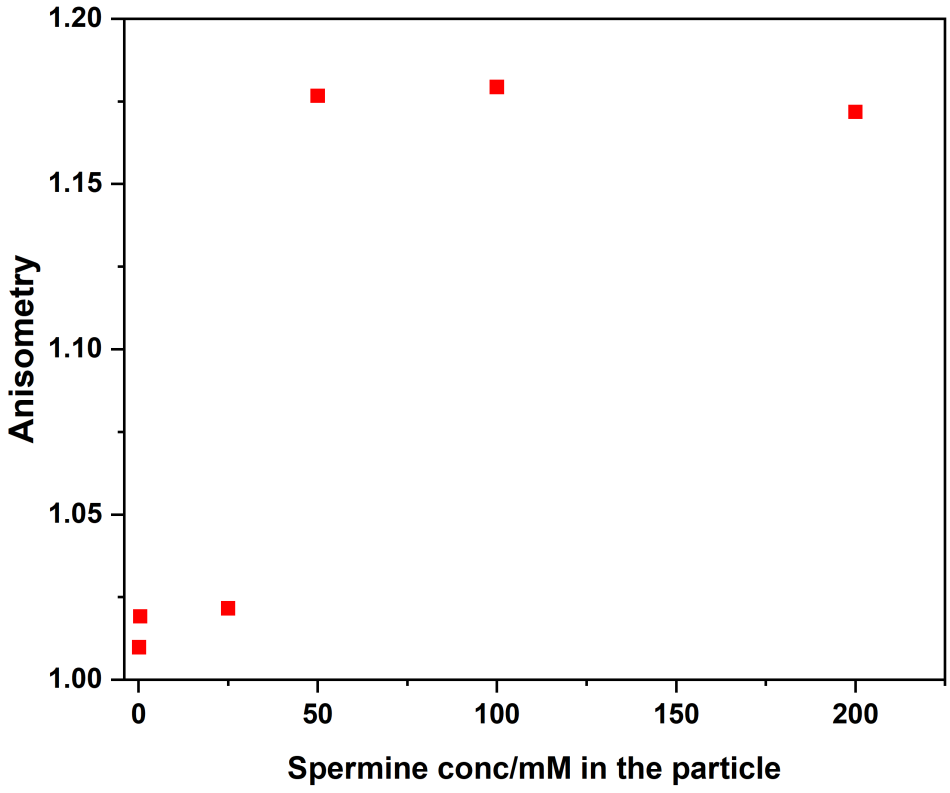

Figure 4.13: Anisometry vs final concentration of spermine in FS_90 based particles

Anisometry values of FS_90-Spermine based particles shown in Figure 4.12 were calculated and drawn in the Figure 4.13 above. Anisometry values were found as 1.01, 1.02, 1.02, 1.18,

1.18 and 1.17 for the particles prepared with 0.4, 1.0, 50, 100, 200 and 400 mM (initial concentrations) spermine solutions respectively. As mentioned previously, up to 50 mM spermine, the particles show very little anisometry and after 50 mM anisometry values show a sharp increase at 1.18 and stays there for the following two concentrations which are twice and three times of 50 mM. This was interesting as we expect to see an increase in anisometry with increasing concentration as in NaCl and NaF cases, however here anisometry values of 3 different concentrations were found same.

After observing formation of anisometric particles at high concentrations, we decided to make FS-Spermine based particles with both FS_90 and FS_90@NH_2. Obtained FS_90-Spermine based particles look white opaque doughnut particles at 200 mM and transparent/bluish doughnut at 400 mM. With FS_90@NH_2, yellowish white opaque doughnut resembling supraparticles are formed (see Figure 4.14).

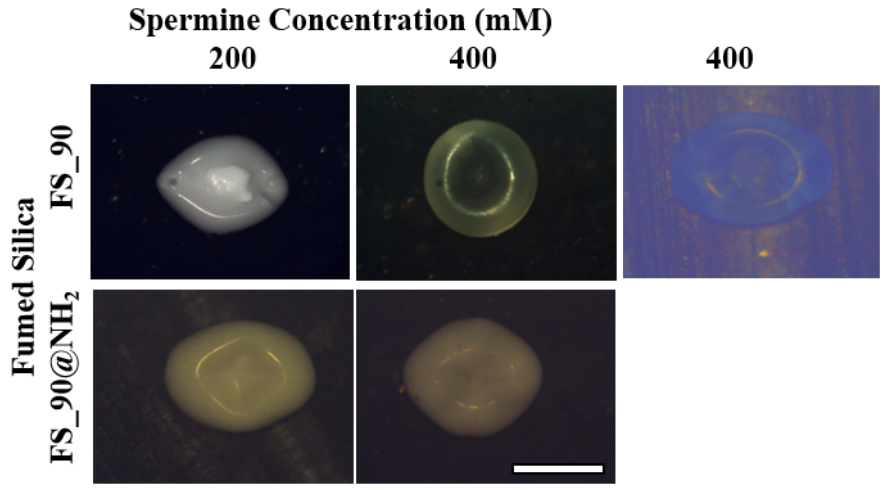

Figure 4.14: Microscope images of FS-Spermine based dried particles (scale bar: 1mm)

In Figure 4.14 the particles prepared with FS_90 and FS_90@NH_2 were put together for the comparison. Anisometry values of the particles prepared with 200 and 400 mM spermine did not show a dramatic difference however the appearance of the particles with FS_90 and FS_90@NH_2 were quite different as it is easily in the figure above. FS_90 and FS_90@NH_2-spermine particles are yellowish white opaque whereas FS_90-spermine particles look white opaque at 200 mM and transparent or bluish transparent at 400 mM.

Looking at the all particles in the series one by one, it was observed that neither FS_90 based particles nor FS_90@NH_2 based ones show systematic properties with respect to shape and appearance. Another interesting outcome was the bluish color and transparency of all particles prepared with FS_90 and 400 mM spermine solution. Half of the particles were transparent, and the other half was bluish transparent elliptic particles (both are shown in the Figure 4.14). This phenomenon was not observed in any other combinations of FS and spermine (for the concentrations of 400 mM and less) and same phenomenon was not observed in the particles prepared with amino-functionalized FS_90.

As it was briefly mentioned above, the particles prepared with FS_90& FS_90@NH_2 and spermine do not show a systematic fashion with respect to anisometry of the particles. Up to 50 mM spermine concentration, FS_90 based particles did not show any anisometry and mentioned previously, they were all spherical and kind of sticky. That`s why we investigated the particles prepared with more concentrated spermine and functionalized FS_90. The results of the anisometry measurements of the particles were illustrated with the graph below in Figure 4.15. Anisometry of the FS_90 based particles were calculated as 1.18 and 1.17 for 200 and 400 mM initial spermine solutions respectively. For the FS_90@NH_2 based particles, anisometry values were found as 1.24 and 1.2 at 200 and 400 mM initial spermine solutions respectively. To talk about a trend arises from the effect of spermine, one should scan a wider range. However, it could be concluded that between 0.4 mM-400 mM spermine concentrations, we could not address to a noticeable tendency with respect to anisometry, morphology and optical properties of the supraparticles independently of FS type (FS_90 and FS_90@NH_2).

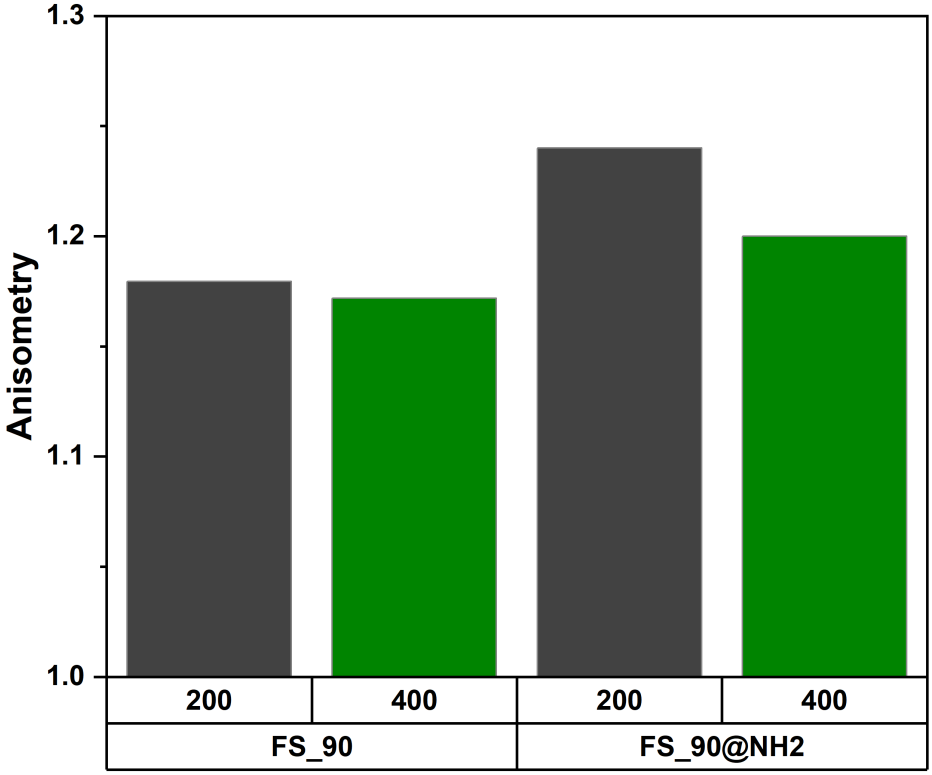

Figure 4.15: Anisometry bars of the FS_90 and FS_90@NH_2-Spermine particles

4.4 Conclusions

This chapter is based on 4 systems with FS and 4 different components as electrolyte to investigate the effect of different electrolytes on the anisometry of FS-based supraparticles. To do that we used NaCl, NaF, Spermine and PEG to mix with three types of commercial FS suspensions provided from Evonik in order to get millimeter sized anisometric supraparticles.

In the first system, NaCl was used as an electrolyte. By mixing 50:50 of NaCl (0.02-50 mM) with FS_90, FS_200 and FS_300 (all 7% wt/v) suspensions, we obtained a system of supraparticles having anisometry directly proportional with NaCl concentration. In this system, we observe two properties: effect of electrolyte concentration and effect of surface area of FS. It was observed that anisometry increases as both electrolyte concentration and surface area of fumed silica increase. Talking about NaCl concentration, the study showed that below 0.02 mM NaCl (final concentration), there is not any significant effect on anisometry, and above 50

mM NaCl (final concentration) dried particles become fragile. Besides endpoints, within the series, anisometry values were calculated in between 1.20 and 1.90 with a regular increase as electrolyte concentration increases. In addition, at the same electrolyte concentration, dried particles of high S.A. value showed higher anisometry. This trend was observed for all electrolyte concentrations and in agreement for all type all FS dispersions. FS_300 particles showed the highest anisometry values, it was followed by FS_200 and FS_90 particles showed the lowest anisometry values in the set.

The second system was based of NaF as electrolyte. The concentration of NaF to be added to FS suspensions was kept between 0.002-200 mM (initial concentration). As in NaCl case, we did not observe any effect of electrolyte on anisometry below 0.02 mM; however, different from the NaCl case, with NaF we were able to use higher concentrations of NaF as we did not notice any fragility above 50 mM. Like in the NaCl series, anisometry of NaF based supraparticles increases with increasing electrolyte concentration, but to a much lesser extent. However, there is a sharp increase seen at 25 mM NaF for the particles with FS_300 and above 25 mM, FS_300 based particles show anisometry values between 1.6 and 2.0 while anisometry values are changing between 1.2 and 1.4 for FS_90&FS_200 based particles. In the complete series, anisometry values of FS_90 and FS_200 based particles are seen closer to each other with smooth increases as NaF concentration increases. All in all, we did not observe a consistent increase in anisometry for the three systems based on different fumed silica suspensions as NaF concentration and surface area of FS increase.

PEG was another additive used in this study in order to get anisometric fumed silica-based particles. By being a hydrophilic, biocompatible low-density polymer, PEG is a good candidate to be used in the preparation of anisometric patchy supraparticles for self-propulsion experiments which take place in further steps in this thesis. For this purpose, we prepared 0.35, 0.035 and 0.0035 % wt PEG solutions with average molecular weights between 400 to $2x10^6$. The particles prepared with PEG400 showed anisometry at low PEG concentrations (0.035 and 0.0035 % wt), the ones prepared with 0.35% wt PEG400 dried as spheres. For the particles prepared with PEG6000, at all concentrations dried particles look like spheres and anisometry values were calculated between 1.0-1.04, which means regardless of the concentration, PEG6000 based particles do not show anisometric tendency compared to the ones with

PEG400 with anisometry values between 1.0-1.30. A brief conclusion on these preliminary experiments showed that as molecular weight of PEG solution increases, the tendency of forming dense agglomerates increases which hinders elongation of the particles during drying and results in spherical particles. This phenomenon is caused by higher viscosity and lower mobility of PEG solution prepared with higher molecular weight. In addition, except the opacity of the resultant particles (observed in all sub-sections), surface area of fumed silica does not bring any significant difference.

With the data obtained from PEG400-FS and PEG-6000 FS based particles, we decided to investigate the effect of the addition of salt to PEG-FS mixtures on the resultant particles as we already know that NaCl has a significant and regular effect on anisometry. To do that 0.02, 0.04, 1.4 and 2.8 % wt PEG400 solutions were prepared and mixed with FS and 100 mM NaCl solutions (PEG:NaCl:FS 1:1:2). As observed in the previous case (PEG:FS) at high PEG concentrations,1.4 and 2.8 % wt, dried particles were formed as spheres. At low concentrations, 0.02 and 0.04 % wt, dried particles showed anisometry increasing with surface area of fumed silica. At the lowest concentration, anisometry of the particles were calculated as 1.46, 1.53 and 1.90 for the particles prepared with FS_90, FS_200 and FS_300 respectively. Another observation with PEG:NaCl:FS particles was their appearance. The formation of small agglomerates of PEG400 was clearly visible in the particles even for some of the spherical ones-FS_300 based particles due to their low opacity. To sum up, PEG:FS based particles show higher anisometry in the presence of NaCl. We might express that anisometry increases with decreasing concentration of PEG solution which is in agreement with the results obtained in the previous section. Another interesting outcome was the appearance of the dried particles with small PEG agglomerations dispersed quite homogeneously in the particles. We observed that these small agglomerations appear in the presence of NaCl.

By knowing that spermine is a tetravalent material in a wide pH range, we decided to investigate the effects of spermine on the anisometry of the FS-based particles. 0.4, 1.0, 50, 100, 200 and 400 mM spermine solutions were prepared and mixed with 7 % wt/v FS solutions. Up to 50 mM, we did not observe any anisometry in the dried particles. That's why, we decided to focus on higher concentrations, 100-400 mM. On the other hand, as functionality of spermine depends on the pH of the medium, amine functionalized FS_90 was also prepared to

see whether FS_90 and FS_90@NH_2 based particles show differences or not. pH of FS_90@NH_2 suspension was found as 7.0 while it is 5.7 for FS_90 suspension. Spermine may appear as tetravalent, trivalent or divalent electrolyte depending on the pH, so it would be easier to observe the functionality of spermine by using FS suspensions with different pH values to ensure having spermine as tetravalent electrolyte. By having a neutral pH, FS_90@NH_2 ensures that spermine would be a tetravalent electrolyte as it is known that at physiological conditions (pH=7.4) spermine was found as tetravalent.

The anisometry values of FS_90-Spermine series were calculated in the range of 1.01-1.18. Anisometry stays around 1.01 for low concentrations, 0.4, 1.0 and 50 mM; and it rises to 1.18 suddenly at 100 mM spermine. For 200 and 400 mM of spermine, it was observed that anisometry values stay nearly constant with 1.18 and 1.17 values respectively. With the particles made up of amine functionalized FS_90, anisometry values are calculated as 1.24 and 1.20 for 200 and 400 mM spermine respectively. Anisometry values of the particles with FS_90@NH_2 were found a little higher than the ones prepared with FS_90 but this difference is not a significant difference to talk about a systematic. In addition, for both FS_90 and FS_90@NH_2 based particles, we observed that there is a light decrease from 200 mM based to 400 mM-based particles unexpectedly. However, this decrease could not be defined as a noticeable change as the ratio of the decrease was calculated as 1.6 % for both FS_90 and FS_90@NH_2. As a conclusion of spermine subsection, there is a critical concentration of spermine at which it contributes the anisometry of the particles, and above this critical concentration there is a tendency of formation of anisometric particles. To talk about a systematic, one should scan higher concentrations than 400 mM, which could be another issue in this part as above 1 M, it is difficult to prepare well-dissolved spermine solution.

Herein, we showed 4 different series of fumed silica-based mm sized particles. The aim was to obtain anisometric particles with a systematic fashion to be further developed for patchy particle preparation. The series of NaCl-FS was found as well-defined by having a systematic fashion in the change of anisometry values with respect to the concentration of NaCl. NaF based system could be also useful for further modification but much lower anisometry values were observed in NaF series compared to NaCl series. In addition, we could not talk about a regular change in anisometry with respect to surface area of fumed silica in NaF series as seen

in NaCl series. PEG could be a very advantageous choice to be used in FS-based supraparticles by being biocompatible and low-density polymer. It was observed that PEG400 and PEG600 agglomerate during evaporation at 0.35 % wt/v. At 10- and 100-times diluted solutions, particles show anisometry by resulting in doughnut like elliptic particles for PEG400 based samples. All PEG6000 droplets dried as spheres due to higher agglomeration caused by higher molecular weight (/chain length) of the polyethylene glycol solution. With this guiding information, we combined NaCl, FS and PEG to obtain anisometric supraparticles. NaCl concentration was fixed to 100 mM and PEG400 solutions prepared for previous subsection were preferred due to low crowd compared to PEG6000 and the ratio of the components were fixed to 1:1:2 for NaCl:PEG400:FS. Anisometry values of NaCl:PEG400:FS were calculated between 1.01 and 1.89 while they were found in between 1.00-1.30 for PEG400:FS series. The highest anisometry values were obtained at low PEG400 concentrations as in previous case. The contribution of NaCl on PEG-FS based particles was seen not only in the elongation of the particles, but also in the appearance of the particles. NaCl:PEG400:FS based particles at low PEG concentrations dried as elliptic opaque particles with clearly seen small agglomerates. NaCl:PEG:FS based particles look opaque and patterned elliptic particles while PEG:FS based particles were looking slightly elongated homogeneously transparent doughnuts. Besides these outcomes, the inverse relationship of surface area of fumed silica and anisometry of the resultant particles is also clear for NaCl:PEG:FS based particles. In summary, to involve PEG for the modification of the FS-based particles, concentration is the critical property to be adjusted. In addition, small agglomerates appeared in the particles in the presence of NaCl could hinder the diffusion of the catalyst which would be an obstacle for further applications.

To conclude, it could be inferred that all 4 additives -NaCl, NaF, Spermine and PEG-, gave very interesting and useful results. Depending on the potential application area or desired functionality of the resultant particles, all additives seem convenient. However, our priority was to obtain mm sized FS-based particles with tunable anisometry. Based on our studies conducted for this aim, we concluded that NaCl is the best additive to obtain anisometric particles by showing a systematic fashion. Therefore, we decided to use NaCl-FS based supraparticles to be further modified for the preparation of patchy particles.

4.5 References

(1) Xia, Y.; Nguyen, T. D.; Yang, M.; Lee, B.; Santos, A.; Podsiadlo, P.; Tang, Z.; Glotzer, S. C.; Kotov, N. A. Erratum: Self-Assembly of Self-Limiting Monodisperse Supraparticles from Polydisperse Nanoparticles. *Nat. Nanotechnol.* **2012**, *7* (7), 479–479. https://doi.org/10.1038/nnano.2012.106.

(2) Velev, O. D.; Gupta, S. Materials Fabricated by Micro- and Nanoparticle Assembly - The Challenging Path from Science to Engineering. *Adv. Mater.* **2009**, *21* (19), 1897–1905. https://doi.org/10.1002/adma.200801837.

(3) Feng, X.; Jiang, L. Design and Creation of Superwetting/Antiwetting Surfaces. *Adv. Mater.* **2006**, *18* (23), 3063–3078. https://doi.org/10.1002/adma.200501961.

(4) Li, F.; Josephson, D. P.; Stein, A. Colloidal Assembly: The Road from Particles to Colloidal Molecules and Crystals. *Angew. Chemie - Int. Ed.* **2011**, *50* (2), 360–388. https://doi.org/10.1002/anie.201001451.

(5) Goesmann, H.; Feldmann, C. Nanoparticulate Functional Materials. *Angew. Chemie - Int. Ed.* **2010**, *49* (8), 1362–1395. https://doi.org/10.1002/anie.200903053.

(6) Galisteo-Lõpez, J. F.; Ibisate, M.; Sapienza, R.; Froufe-Pérez, L. S.; Blanco, Ú.; Lõpez, C. Self-Assembled Photonic Structures. *Adv. Mater.* **2011**, *23* (1), 30–69. https://doi.org/10.1002/adma.201000356.

(7) Rolison, D. R. Catalytic Nanoarchitectures--the Importance of Nothing and the Unimportance of Periodicity. *Science.* **2003**, *299* (5613), 1698–1701. https://doi.org/10.1126/science.1082332.

(8) Cho, A. Connecting the Dots to Custom Catalysts. *Science.* **2003**, *299* (March), 1684–1685. https://doi.org/10.1126/science.299.5613.1684.

(9) Lu, Z.; Yin, Y.; Kim, H.; Kwon, S.; Lee, H.; Ge, J.; Goebl, J.; He, L.; Kim, J. Magnetochromatic Microspheres: Rotating Photonic Crystals. *J. Am. Chem. Soc.* **2009**, *131* (43), 15687–15694. https://doi.org/10.1021/ja903626h.

(10) Kim, J.; Song, Y.; He, L.; Kim, H.; Lee, H.; Park, W.; Yin, Y.; Kwon, S. Real-Time Optofluidic Synthesis of Magnetochromatic Microspheres for Reversible Structural Color Patterning. *Small* **2011**, *7* (9), 1163–1168. https://doi.org/10.1002/smll.201001822.

(11) Weitz, D. A.; Kanai, T.; Lee, D.; Shum, H. C.; Shah, R. K. Gel-Immobilized Colloidal Crystal Shell with Enhanced Thermal Sensitivity at Photonic Wavelengths. *Adv. Mater.* **2010**, *22* (44), 4998–5002. https://doi.org/10.1002/adma.201002055.

(12) Vogel, N.; Weiss, C. K.; Landfester, K. From Soft to Hard: The Generation of Functional and Complex Colloidal Monolayers for Nanolithography. *Soft Matter* **2012**, *8* (15), 4044–4061. https://doi.org/10.1039/c1sm06650a.

(13) Isa, L.; Kumar, K.; Müller, M.; Grolig, J.; Textor, M.; Reimhult, E. Particle Lithography from Colloidal Self-Assembly at Liquid-Liquid Interfaces. *ACS Nano* **2010**, *4* (10), 5665–5670. https://doi.org/10.1021/nn101260f.

(14) Xiao, Z.; Wang, A.; Perumal, J.; Kim, D. P. Facile Fabrication of Monolithic 3D Porous Silica Microstructures and a Microfluidic System Embedded with the Microstructure. *Adv. Funct. Mater.* **2010**, *20* (9), 1473–1479. https://doi.org/10.1002/adfm.200902164.

(15) Rastogi, V.; Velikov, K. P.; Velev, O. D. Microfluidic Characterization of Sustained Solute Release from Porous Supraparticles. *Phys. Chem. Chem. Phys.* **2010**, *12* (38), 11975–11983. https://doi.org/10.1039/c0cp00119h.

(16) Yin, S. N.; Wang, C. F.; Yu, Z. Y.; Wang, J.; Liu, S. S.; Chen, S. Versatile Bifunctional Magnetic-Fluorescent Responsive Janus Supraballs towards the Flexible Bead Display. *Adv. Mater.* **2011**, *23* (26), 2915–2919. https://doi.org/10.1002/adma.201100203.

(17) Yang, S.-M.; Pine, D. J.; Yi, G.-R.; Moon, J. H.; Park, S. B. Electrospray-Assisted Fabrication of Uniform Photonic Balls. *Adv. Mater.* **2004**, *16* (7), 605–609. https://doi.org/10.1002/adma.200305446.

(18) Shen, Z.; Zhu, Y.; Wu, L.; You, B.; Zi, J. Fabrication of Robust Crystal Balls from the Electrospray of Soft Polymer Spheres/Silica Dispersion. *Langmuir* **2010**, *26* (9), 6604–6609. https://doi.org/10.1021/la903938s.

(19) Yu, Z.; Chen, L.; Chen, S. Uniform Fluorescent Photonic Crystal Supraballs Generated from Nanocrystal-Loaded Hydrogel Microspheres. *J. Mater. Chem.* **2010**, *20* (29), 6182–6188. https://doi.org/10.1039/c0jm00400f.

(20) Jonas, U.; Knoll, W.; Burkert, K.; Wang, J.; Ottleben, H.; Neumann, T. Automated Preparation Method for Colloidal Crystal Arrays of Monodisperse and Binary Colloid Mixtures by Contact Printing with a Pintool Plotter. *Langmuir* **2007**, *23* (6), 3478–3484. https://doi.org/10.1021/la063122z.

(21) Rastogi, V.; Velev, O. D. Development and Evaluation of Realistic Microbioassays in Freely Suspended Droplets on a Chip. *Biomicrofluidics* **2007**, *1* (1), 1–17. https://doi.org/10.1063/1.2714185.

(22) Wang, J. T.; Wang, J.; Han, J. J. Fabrication of Advanced Particles and Particle-Based Materials Assisted by Droplet-Based Microfluidics. *Small* **2011**, *7* (13), 1728–1754. https://doi.org/10.1002/smll.201001913.

(23) Yu, Z.; Wang, C. F.; Ling, L.; Chen, L.; Chen, S. Triphase Microfluidic-Directed Self-Assembly: Anisotropic Colloidal Photonic Crystal Supraparticles and Multicolor Patterns Made Easy. *Angew. Chemie - Int. Ed.* **2012**, *51* (10), 2375–2378. https://doi.org/10.1002/anie.201107126.

(24) Cho, Y. S.; Kim, S. H.; Yi, G. R.; Yang, S. M. Self-Organization of Colloidal Nanospheres inside Emulsion Droplets: Higher-Order Clusters, Supraparticles, and Supraballs. *Colloids Surfaces A Physicochem. Eng. Asp.* **2009**, *345* (1–3), 237–245. https://doi.org/10.1016/j.colsurfa.2009.05.014.

(25) Cho, Y.-S.; Yi, G.-R.; Kim, S.-H.; Elsesser, M. T.; Breed, D. R.; Yang, S.-M. Homogeneous and Heterogeneous Binary Colloidal Clusters Formed by Evaporation-Induced Self-Assembly inside Droplets. *J. Colloid Interface Sci.* **2008**, *318* (1), 124–

133. https://doi.org/10.1016/j.jcis.2007.10.010.

(26) G. Whitesides, M. B. G. Self-Assembly at All Scales. *Science (80-.).* **2002**, *295* (5564), 2418–2421. https://doi.org/10.1126/science.1070821.

(27) Brinker, C. J.; Lu, Y.; Sellinger, A.; Fan, H. Evaporation-Induced Self-Assembly: Nanostructures Made Easy. *Adv. Mater.* **1999**, *11* (7), 579–585. https://doi.org/10.1002/(SICI)1521-4095(199905)11:7<579::AID-ADMA579>3.0.CO;2-R.

(28) Lee, D.-W.; Jin, M.-H.; Lee, C.-B.; Oh, D.; Ryi, S.-K.; Park, J.-S.; Bae, J.-S.; Lee, Y.-J.; Park, S.-J.; Choi, Y.-C. Facile Synthesis of Mesoporous Silica and Titania Supraparticles by a Meniscus Templating Route on a Superhydrophobic Surface and Their Application to Adsorbents. *Nanoscale* **2014**, *6* (7), 3483. https://doi.org/10.1039/c3nr05501a.

(29) Rastogi, V.; Melle, S.; Calderón, O. G.; García, A. A.; Marquez, M.; Velev, O. D. Synthesis of Light-Diffracting Assemblies from Microspheres and Nanoparticles in Droplets on a Superhydrophobic Surface. *Adv. Mater.* **2008**, *20* (22), 4263–4268. https://doi.org/10.1002/adma.200703008.

(30) Rastogi, V.; Garcia, A. A.; Marquez, M.; Velev, O. D. Anisotropie Particle Synthesis inside Droplet Templates on Superhydrophobic Surfaces. *Macromol. Rapid Commun.* **2010**, *31* (2), 190–195. https://doi.org/10.1002/marc.200900587.

(31) Sperling, M.; Velev, O. D.; Gradzielski, M. Controlling the Shape of Evaporating Droplets by Ionic Strength: Formation of Highly Anisometric Silica Supraparticles. *Angew. Chemie - Int. Ed.* **2014**, *53* (2), 586–590. https://doi.org/10.1002/anie.201307401.

(32) Velev, O. D.; Lenhoff, A. M.; Kaler, E. W. A Class of Microstructured Particles through Colloidal Crystallization. *Science (80-.).* **2000**, *287* (5461), 2240–2243. https://doi.org/10.1126/science.287.5461.2240.

(33) R. D. Deegan; O. Bakajin; T. F. Dupont; G. Huber; S. R. Nagel; T. A. Witten.

Capillary Flow as the Cause of Ring Stains from Dried Liquid Drops. *Nature* **1997**, *389*, 827–829.

(34) Still, T.; Yunker, P. J.; Yodh, A. G. Surfactant-Induced Marangoni Eddies Alter the Coffee-Rings of Evaporating Colloidal Drops. *Langmuir* **2012**, *28* (11), 4984–4988. https://doi.org/10.1021/la204928m.

(35) von Lospichl, B. Structural Investigation of C12 Endcapped Star Shaped Thermoresponsive Polymers in Aqueous Solutions, Technische Universität Berlin, **2015**.

(36) Schneider, C. A.; Rasband, W. S.; Eliceiri, K. W. NIH Image to ImageJ: 25 Years of Image Analysis. *Nat. Methods* **2012**, *9* (7), 671–675. https://doi.org/10.1038/nmeth.2089.

(37) Kurtulus, I. Synthesis of Amine Containing Well - Defined Polymers Via Reversible Addition-Fragmentation Chain Transfer (Raft) Polymerization and Their Characterization, Izmir Institute of Technology, **2013**.

(38) Weisell, J. M. Structure and Function of Charge Deficient Polyamines, University of Eastern Finland: Kuopio, **2012**.

CHAPTER 5: PREPARATION of PATCHY PARTICLES[1]

Scope of the Chapter

As the continuation of Chapter 4, Chapter 5 is based on the improvement of the previously obtained particles for potential application areas. In the previous chapter, the preparation of anisometric FS-NaCl based particles was illustrated. Here, the preparation of FS-NaCl based anisometric patchy particles will be given in detail. To end up with stable patchy particles, we made some modifications including impartment of different components like PS, Na_2SiO_3 and MFC. Additionally, for the stability of the particles during self-propulsion experiments, we focused on the improvement of the hydrophobicity of the particles. Anisometry was ensured by NaCl and catalytic property of the patchy particles was achieved by incorporating Fe_3O_4@Pt core-shell nanoparticles.

5.1 Introduction

Symmetric and asymmetric colloidal building blocks have been studied for the last few decades. These supraparticles are then improved by making structural and internal architecture. One of these modifications was reported in 2008 by Rastogi et. Al.[1] They obtained highly light-diffracting spherical supraparticles from colloidal suspensions of gold nanoparticles and polystyrene (PS) latex microspheres. The reason of the gold particles' gathering inhomogeneously at the top surface of the droplet is the evaporation flux inside the droplet.

Here, we present a supraparticle system consisting of FS as a base component, NaCl to ensure the anisometry of the particles, a catalytic active patch formed with Fe_3O_4@Pt core-shell nanoparticles to provide self-propulsion ability to the particles and lastly PS, Na_2SiO_3 and MFC for the stability. Four different colloidal mixtures including these components were used to obtain stable patchy particles and the preparation pathway is shown in the Figure 5.1 below.

[1] Similar content has been published in H. Esra Oguztürk, Leona J. Bauer, Ioanna Mantouvalou, Birgit Kanngieβer, Orlin D. Velev, Michael Gradzielski, Preparation of Reinforced Anisometric Patchy Supraparticles for Self-Propulsion, Particle & Particle Systems Characterization (Part. Part. Syst. Charact.), 2000328, Published: May 2021 (doi: 10.1002/ppsc.202000328)

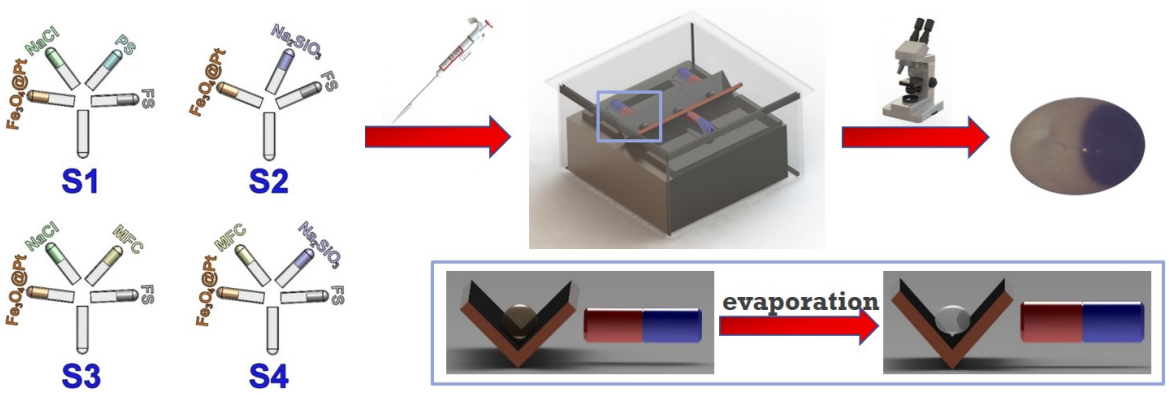

Figure 5.1: Schematic illustration of the preparation of patchy particles

PS and silica have been widely used in self-assembled supraparticle systems. However, to improve the stability of the particles, i.e. prevent disintegration during self-propulsion experiment, additional solutions were sought out. Na_2SiO_3 (waterglass) is a good candidate to improve the stability of the particles with suitable properties. It has been used in the industry as sealant, binder, deflocculant, emulsifier and buffer.[2] The property of binding of Na_2SiO_3 would bring the compactness to the particles and prevent disintegration during self- propulsion. In addition to Na_2SiO_3, MFC was imparted to the colloidal mixture both with and without Na_2SiO_3. MFC's contribution to the particles comes from its unique properties like high surface area, high viscosity and at low temperatures, being extremely robust to pH and temperature. However, its fibrillary internal structure which is the most important property for our system to improve the stability of the particles.[3]

5.2 Experimental

5.2.1 Materials

Materials	Specifications	Supplier
Fumed silica (FS) AEROSIL® 90	surface area=90 ± 15 m^2/g	Evonik
PS-latex	d = 0.96 μm, ρ_{solid} = 1.05 g/ml c_{solid} = 10%w/v	Bangs-Labs
NaCl	synthesis-grade, ≥ 99.9%	ChemSolute
Na_2SiO_3	≥18% Na (as Na_2O) basis, ≥60% Si (as SiO_2) basis	Sigma-Aldrich
MFC	grade HP-55, Mw 84 000 g/mol, Mn 21 000 g/mol	Shin Etsu Chemical Co.
MiliQ water	≥ 18 MΩ/cm	
H_2O_2	30% wt	Sigma Aldrich
$NaBH_4$	≥96%	Sigma-Aldrich
$H_2PtCl_6 \cdot 6H_2O$	≥37.5% Pt basis	Sigma-Aldrich
Sodium Citrate Tribasic Hydrate	ACS reagent, ≥99.0%	Sigma-Aldrich
HCl	aqueous, 37%w/w	Merck
NaOH	ACS-grade, ≥ 98%, pellets	Fluka
$FeCl_2 \cdot 4H_2O$	≥ 98%	Sigma-Aldrich
$FeCl_3 \cdot 6H_2O$	ACS-grade, ≥ 98%	Sigma-Aldrich

5.2.2 Preparation of Patchy Particles

5.2.2.1 Preparation of Fe_3O_4@Pt nanoparticles

As a starting point in the preparation of catalytic patches, the synthesis of Fe_3O_4 nanoparticles was done. The synthesis was done based on the procedure given by Kang and coworkers.[4] 5.2 g $FeCl_3 \cdot 6H_2O$ and 2.0 g $FeCl_2 \cdot 4H_2O$ (molar ratio: Fe(II)/Fe(III)=0.5) were dissolved in 25 ml of deoxygenated water and combined with 0.85 ml of 12 M HCl added under stirring at room temperature. The resultant solution was added to 250 mL of 1.5 M NaOH solution to be neutralized under vigorous stirring. Instant black precipitate appearance was the proof of Fe_3O_4 nanoparticle formation. Formed nanoparticles were then separated from the rest of the

suspension easily with the help of a magnet and purification was performed with simple decantation.

Afterwards, Fe_3O_4@Pt synthesis was performed with $H_2PtCl_6 \cdot 6H_2O$ at room temperature by using the conventional reduction method with $NaBH_4$ in the presence of sodium citrate tribasic hydrate. 114 µl $H_2PtCl_6 \cdot 6H_2O$ solution was added dropwise to 95 mL of the previously synthesized stirred Fe_3O_4 solution (0.02 %w) in 1 minute. After waiting for 2 min, 1.5 mL of ice-chilled 0.01 M $NaBH_4$ solution was added dropwise in 1.5 min. Then 1 ml of 0.5 M sodium citrate solution was added at once 1 min after $NaBH_4$ addition. After all components were added, the solution was stirrer for 3-5 min more at 7200 rpm speed with ultraturrax. The resultant solution was taken to be centrifuged for 15 min at 4000 rpm 3 times to remove the impurities and to be concentrated. Weight percent determination of Fe and Pt in the catalyst was performed with ICP-OES [Varian ICP-OES 715 ES] measurement by Astrid Mueller-Klauke in TU Berlin. Before ICP-OES, microwave was used to dissolve Pt in Fe_3O_4 in presence of aqua regia. For microwave treatment, 8 ml aqua regia was prepared and mixed with 200 mg of Fe_3O_4@Pt and the mixture was left for at least 2-3 hours in quartz sample holder. Then the sample was put into a microwave and heated up to 160° at 18 bar pressure with 4 min ramp and 10 min hold temperature. After microwave, sample was diluted to 20 ml volumetric flask and given for ICP measurement with 5 standard solutions of Fe and Pt.

The data obtained from ICP-OES demonstrated that, Fe^{3+} and Pt concentrations in 200 mg sample were 11.79 mg/l and 0.69 mg/l respectively. With this information in hand, the Fe_3O_4@Pt concentration with respect to the sample, was calculated as 0.17 %wt.

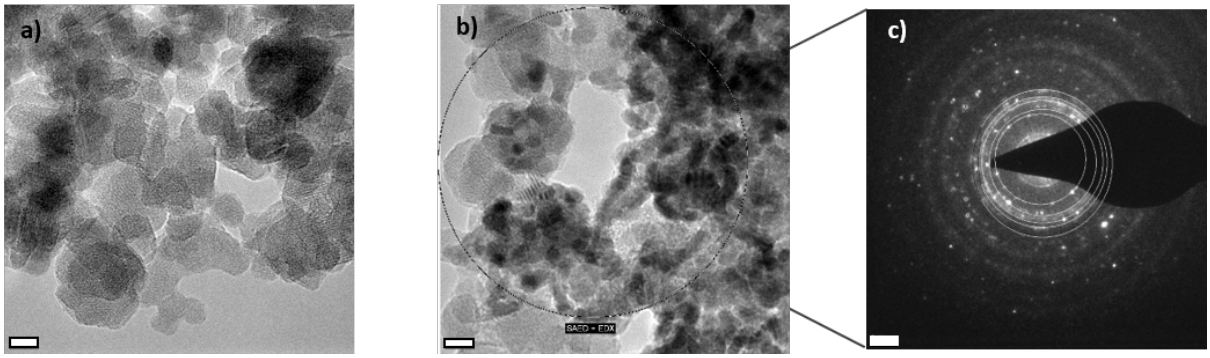

Figure 5.2: TEM images of a) Fe_3O_4, b) Fe_3O_4@Pt and c) SAED pattern (130 nm area was chosen in diameter) Scale bar: 5 nm for a and b; 21 nm^{-1} for c.

TEM measurement was done to obtain structural information about the synthesized nanoparticles. The measurement was performed by Jan Simke in ZELMI TU Berlin and images collected with a FEI Tecnai G^2 20 S-TWIN Transmission Electron Microscope. In the Figure 5.2 above, electron micrographs of Fe_3O_4 and Fe_3O_4@Pt samples are illustrated. Figure 5.2c shows a SAED (Selected Area Electron Diffraction) pattern from the indicated region (in Figure 5.2b) of the Fe_3O_4@Pt sample which proves the presence of Fe_3O_4 (spots) and Pt (rings) by comparison to the database of The International Centre for Diffraction Data.[5,6] Dark colored agglomerates in the Figure 5.2b is the evidence of randomly distributed Pt on the Fe_3O_4 nanoparticles. The size of the Fe_3O_4@Pt nanoparticles lies between 8-12 nm.

5.2.2.2 Preparation of patchy supraparticles

7% wt/v pre-prepared FS suspensions, electrolyte (NaCl) solutions and a dispersion of 0.017% wt/v magnetic/catalytic nanoparticles (Fe_3O_4@Pt) were mixed to make patchy supraparticles. The long-term purpose was to obtain stable patchy particles of variable shape for self-propulsion; therefore, final shape of the dried particles has the priority. To obtain patchy particles of well-defined shape, we decided to use 10 mM-50 mM NaCl solutions based on the observations on the previous chapter. To do that, a 100 mM NaCl stock solution was prepared and diluted as needed.

For the improvement of the stability/compactness of the particles, polystyrene (PS), sodium trisilicate (Na_2SiO_3), or microfibrillated cellulose (MFC) were added to the colloidal dispersion separate and/or combined. 10 wt% PS latex, 1.5 wt% MFC dispersions and 0.1 M Na_2SiO_3

solution were added in different ratios to the colloidal mixture to make a droplet which was subsequently evaporated into supraparticle.

Table 5.1: Concentrations of the stock solutions used in the recipes and the amounts (in volume) of the components added to the colloidal mixtures ([*]Fixed in all compositions; [≠]Variable components)

Components	wt/v% of the stock solution	v% in the mixture
Fumed Silica[*]	7.00	50
NaCl[≠]	0.58	20-25
Fe3O4@Pt [*]	0.17	25
Polystyrene[≠]	10.00	5
Na_2SiO_3[≠]	0.242	10-25
MFC[≠]	1.50	15-20

As seen in the Table 5.1, the volumes of FS and Pt catalyst were fixed in the recipe; NaCl, PS, Na_2SiO_3 and MFC amounts were changed to obtain particles with different properties to be investigated. We ended up with 4 type of particles and named as: Sample 1 (S1) containing PS, Sample 1^a & Sample 1^b ($S1^a$ and $S1^b$; have the same composition as S1, the only difference is the additional heat treatment and hydrophobization agent applied to $S1^a$ and $S1^b$ respectively after drying), Sample 2 (S2) with added Na_2SiO_3, Sample 3 (S3) containing MFC and Sample 4 (S4) containing MFC and Na_2SiO_3. The final compositions of all particles are given in detail in Table 5.2 below.

Table 5.2: Final compositions of the different samples prepared and investigated.

Samples / Components wt %	Class 1 (S1&S1[a]&S1[b])	Class 2 (S2)	Class 3 (S3)	Class 4 (S4)
Fumed Silica	86.33	84.37	97.09	91.12
NaCl	0.29		0.12	
Fe_3O_4@Pt	1.05	1.03	0.71	1.11
Polystyrene	12.33			
Na_2SiO_3		14.60		6.38
MFC			2.08	1.47

To obtain catalytically active supraparticles; FS, electrolyte, Fe_3O_4@Pt, and a potential additive for stabilization were mixed to a homogeneous dispersion by Vortex stirring in a vial. Then 3 µl droplets of this colloidal mixture was template on previously prepared 90° superhydrophobic surfaces. The patch made of Fe_3O_4@Pt nanoparticles was directed by the attractive magnetic forces formed by NdFeB cylinder magnets with Nickel coating (with flux density inside: 1.37 Tesla & flux density on the surface: 0.5856 Tesla[7]). As the magnets were fixed on a pre-determined side of the superhydrophobic surface, the patch of Fe_3O_4@Pt was localized to desired spot (see Figure 5.3).

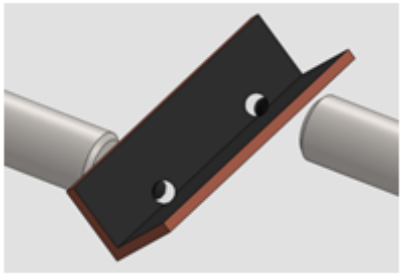

Figure 5.3: Constructed set-up to obtain patchy particles

In Figure 5.3, optical micrographs of the prepared samples S1, S2, S3 and S4 are shown. S1, S3 and S4 are yellowish white with a well-defined distinction of patch. S2 was also expected to be nicely patched, however due to the internal alignment of ingredients catalyst was trapped

inside the particle during evaporation of the droplet. This phenomenon will be explained in the following sections.

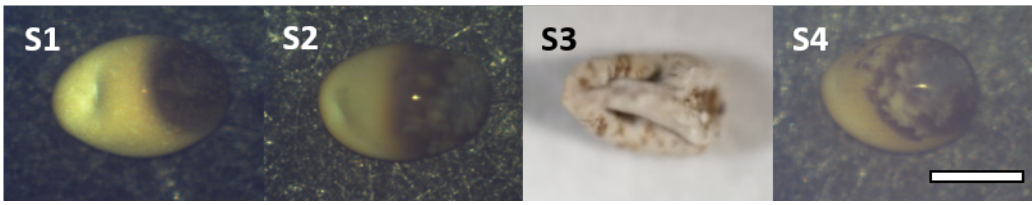

Figure 5.4: Optical micrographs of the supraparticles prepared with different colloidal compositions (scale bar: 500 µm and same for all images)

The colloidal mixture first templated on the surfaces as a droplet, has a brownish color due to the catalyst. As time passes during evaporation, with the help of attractive forces, catalytic nanoparticles were pulled to the pre-determined location and this brings the slow color change from homogeneous brownish to yellowish white anisometric particle with a dark brown "eye-like" patch. The animation (prepared in Autodesk Maya software[8]) of patch formation is illustrated in Figure 5.5 to clarify the description above.

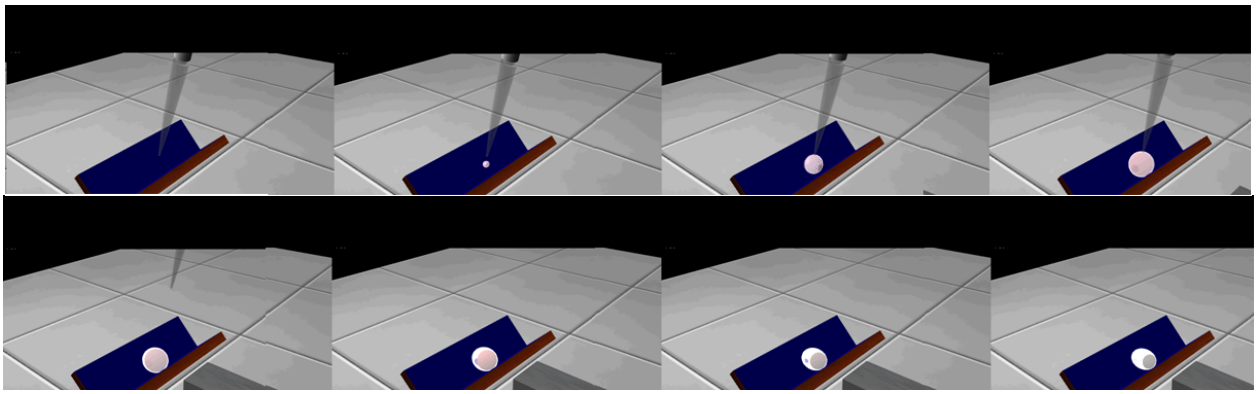

Figure 5.5: Step-wise patch formation (Blue color was chosen to get a better contrast)

5.2.2.3 Self-Propulsion experiments and stability experiments in H_2O_2 solution

To test the stability of the particles, we conducted preliminary self-propulsion experiments on H_2O_2 solution. The particles were put on a plastic petri dish (diameter of 9 cm) filled with 5% H_2O_2. When wetting of the particle occurs, catalyst and H_2O_2 contacts and decomposition of H_2O_2 into H_2O and oxygen gas starts. Oxygen bubbles are formed on the patchy side of the

particle and when the oxygen is relieved from the particles' surface, particles start moving through the opposite direction due to conservation of momentum[9]. The experimental procedure was recorded by a camera (CANON EOS 5D MARK II).

The details on self-propulsion experiments will be given in the next chapter with the data handled and evaluated.

5.3 Results and Discussion

The patchy particles containing Fe_3O_4@Pt nanoparticles were prepared in order to be employed for self-propulsion. The proposed mechanism for self-propulsion is based on decomposition reaction of H_2O_2, which is the fuel, and the motion is defined as "away from the catalyst" under the title of bubble propulsion. The preparation procedure was achieved successfully, however one should ensure to end up with structurally long-lived particles able to sustain catalytic performance. Therefore, the mechanical stability and integrity of these patchy anisometric supraparticles is of central importance for using them subsequently in self-propulsion.

5.3.1 Disintegration of Pure FS/Fe_3O_4@Pt Supraparticles during Self-Propulsion

The supraparticles, the whole composition of which were given in the previous sections, contain hydrophilic components and the major part is made up of FS. Accordingly, when the particles were put into H_2O_2 solution, water permeable pores of the FS were fully wetted. When the decomposition of H_2O_2 into H_2O and oxygen gas starts, oxygen bubble formation also occurs in the pores and the capillary pressure leads to a substantial mechanical strain within the pores. This O_2 buildup can cause the disintegration of the patchy supraparticles after being immersed with H_2O_2 solution, as experimentally observed. At the same time, the full wetting of the supraparticle raises its probability of sinking into the solution and not swimming on its surface, as desired for such particles. This phenomenon brings the challenge of making a reliable self-propelling system. That's why we investigated the stability of the patchy supraparticles in H_2O_2 solution. We observed that the first prepared patchy particles disintegrate within few seconds after being placed into the 5 wt% H_2O_2 solution, as shown in the images given in Figure 5.6 (The images are taken from the videos of self-propulsion

experiments). Row a and row b represent two different particles with same composition and appearance.

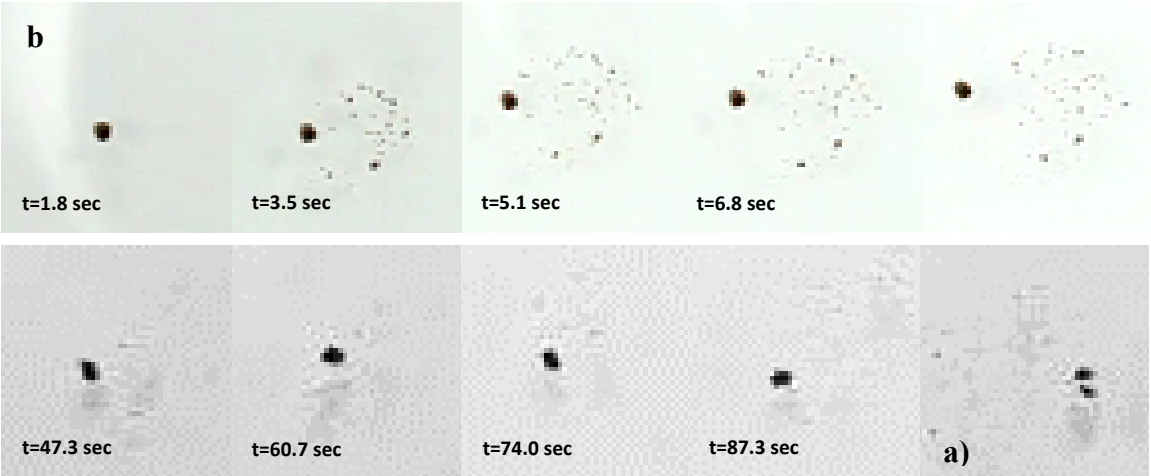

Figure 5.6: Examples of breakdown of two S1 type supraparticles (S1-a & S1-b). (Frames were picked from the recorded videos of self-propulsion experiments, t=0 refers to the time at which the particle is placed on the aqueous H_2O_2 solution) [Visual cross-section area: 8.2x8.2 cm^2].

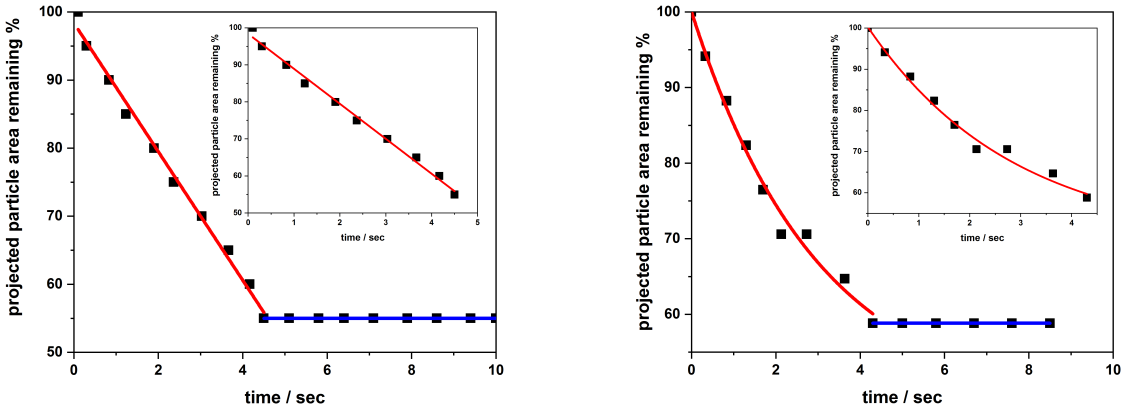

Figure 5.7: Disintegration profiles of S1-a & S1-b with time (t=0 refers to the time at which wetting occurs; lines are guides to the eye)

To quantify the degree of disintegration, the pixels of the particles in the frames captured at certain time slots were counted and evaluation was made based on the visible area decrease during self-propulsion experiments. The percent decomposition of the particles (S1-a and S1-

b) previously mentioned in Figure 5.6 were calculated and drawn in Figure 5.7. As illustrated in the graphs above, disintegration of the 40-50 % of the particles' projected area occurs in about 4-5 seconds. Rarely, for some particles this time may reach to minutes. After losing around 40-50 % of their projected area, particles were long-term stable and further disintegration was not observed.

This observation showed that the supraparticles have high tendency to disintegrate in a few seconds. Therefore, some modifications were necessary to be applied to enhance the stability of the particles for self-propulsion.

5.3.2. Modifications for Enhancing the Stability of FS/Fe_3O_4@Pt Supraparticles

There are two main problems affecting the stability of the supraparticles. The first problem is their hydrophilicity, which results in gas formation within their pores due to wetting, and the build-up of capillary pressure within them. The second problem is the brittleness and the fragility as the systems including dry silicate causes cracking and rapid disintegration. In order to figure out particle disintegration, various solutions were considered, which were based on both reducing hydrophilicity and impartment of new materials to increase mechanical strength.

5.3.2.1 Supraparticles' Heat Treatment (Sample 1[a])

Heat treatment is another approach to reduce the number of free Si-OH groups by a condensation reaction in which more hydrophobic Si-O-Si bridges are formed by eliminating H_2O.[10] With heat treatment, in general it is possible to obtain more compact particles with less porosity. Main control parameters in this treatment are temperature and time of heating.

After the particles had been dried on superhydrophobic surfaces, they were put into an oven at around 110-120 °C for 4 to 20 hours. It was observed that the efficiency of hydrophobization was changing depending on the heating time. When the particles were heated for a few hours hydrophobization was not sufficient and disintegration could not be prevented (same case with Figure 5.5 and 5.6). However, when the heating time was longer, i.e. 16-20 hours, particles became overhydrophobized similarly to in the CH_3Cl_3Si case, which results in the inactivation of the catalytic activity.

5.3.2.2 Supraparticles' Treatment with Hydrophobization Agent (Sample 1[b])

To decrease the hydrophilicity of the particles, one approach could be hydrophobization of the particles with a hydrophobization agent, which was trichloro methyl silane (CH_3Cl_3Si) in our case. We performed hydrophobization via chemical vapor deposition (CVD) of trichloro methyl silane (CH_3Cl_3Si) on the particle. The reason of intrinsic hydrophilicity are the free Si-OH groups on the surface of the supraparticles. CH_3Cl_3Si reacts with the free Si-OH groups due to its high reactivity and decrease the particle's hydrophilicity (see Scheme 5.1). CVD was performed by simply putting the particle and few µl (5-10 µl) of CH_3Cl_3Si in separate petri dishes close together (2 cm distance) in a closed chamber at controlled humidity for a few seconds.

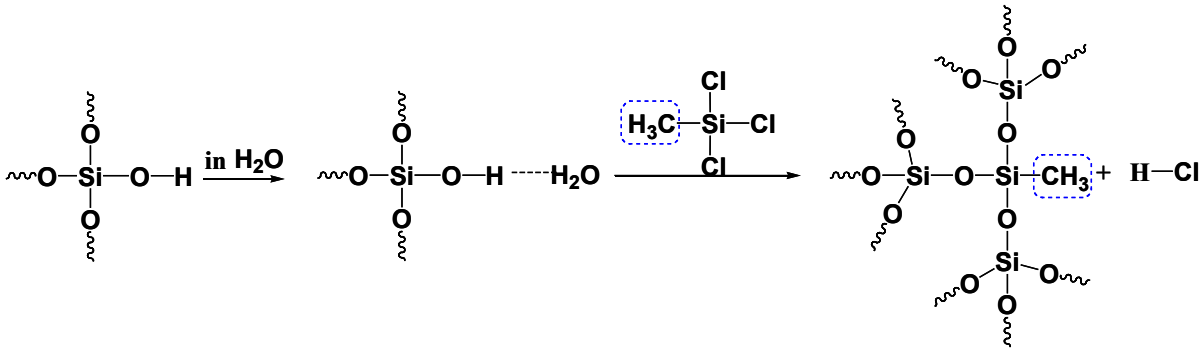

Scheme 5.1: Proposed mechanism of hydrophobization of patchy particles with CH_3Cl_3Si treatment

Although the time for CVD with CH_3Cl_3Si was kept very short (~10 seconds), the reaction went too fast resulting in over-hydrophobization of the particles. In other words, CVD with CH_3Cl_3Si was successful to prevent disintegration of the particles, however in the meantime the catalytically active sites were covered and inactivated as well. Consequently, these modified supraparticles failed to sustain self-propulsion.

On the contrary, to prevent inactivation of the catalyst, when CVD was performed for shorter times (3-5 seconds), partial hydrophobization occurred which could not prevent disintegration during self-propulsion. In conclusion, the results showed that it was not possible to adjust an appropriate contacting time that allowed to achieve reproducible results and to have good control over the hydrophobization process.

5.3.2.3 Incorporation of Polystyrene (PS) Latex Particles (Sample 1)

As another approach for the modification of the particles, PS was added into the colloidal mixture to improve the stability of the particles by forming composite/polymer particles. PS was used as a multifunctional component in the particles, both being a gluing and softening agent, and improving the swimming ability of the particles due to having a lower density (1.05 g/cm^3) than the supraparticles (densities of the components in the colloidal mixture of FS, Fe_3O_4, Pt and NaCl are: 2.2, ~5.17, 21.45 and 2.16 g/cm^3, respectively).

For the modification of the particles with PS, we added 10.0 wt% PS solution into the colloidal mixture. PS functions as an internal binding agent and at the same time it glues together the FS network effectively. The amount of PS in the colloidal mixture is the most important parameter to be adjusted carefully. When we added small amounts of PS (below 5 v% relative to the dry supraparticles), no significant effect was observed on the stability of the particles. Accordingly, higher amounts of PS (10 v% with respect to the dry supraparticles) were employed to optimize the procedure. However, in the latter case, we observed that particles became brittle and were breaking into several pieces during the drying process.

As the amount of PS is too sensitive, we decided to combine PS addition and heat treatment to obtain both stable and functional supraparticles. The glass transition temperature of PS is around 100 °C and by heating the samples above 100 °C, we could ensure softening/melting of the PS nanoparticles so they can form a much more homogeneous and interconnected matrix with the FS, as showed in the Figure 5.8 below. Therefore, we added 5 v% of PS from 10 wt/v% stock (12.33 wt% in dry particle) into the colloidal mixture and as soon as particles started to become dry, they were put into an oven for few (3-4) hours at around 100-120 °C. In the Figure 5.8 below, it is clearly seen that randomly distributed PS spheres in the unheated particle (left) have disappeared in the sintered particle (right) and a relatively homogeneous material is formed. Having these SEM images in hand, more compact particles are expected to be prepared with PS' contribution as a binding/bridging agent for the FS.

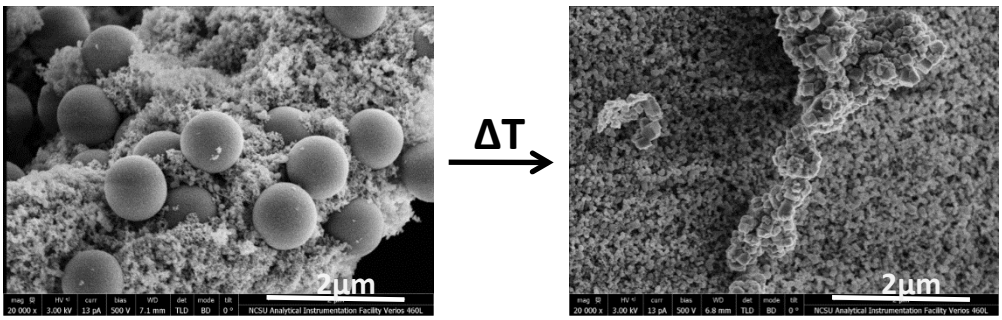

Figure 5.8: SEM images for the sintering process of PS under heat treatment, left: before heat treatment and right: after heating above the glass transition temperature (S1[a]). (The SEM images were taken in NCSU)

5.3.2.4 Incorporation of Sodium Trisilicate Na_2SiO_3 (Sample 2)

Sodium silicate, or more commonly in the industry "water glass", has been used in various fields as an adhesive agent to keep silica based components together.[11] By knowing the functionality, we also used Na_2SiO_3 in order to enhance the mechanical stability of our FS based supraparticles as an alternative to PS&heat method. Based on our observations, below 0.1 M, Na_2SiO_3 does not have a significant effect on anisometry of the particles, however above 0.5 M particle shapes become irregular (see Figure 5.9).

Figure 5.9: Optical microscopy images of 3 examples of 0.5 M Na_2SiO_3 incorporated FS based particles. Irregular shape and inhomogeneity formation occurred due to high concentration/amount of Na_2SiO_3 (scale bar: 0.5 mm)

Therefore, to make an efficient modification with Na_2SiO_3, 0.1 M and 0.2 M solutions (10-20 v% in droplet) were added to the colloidal mixture and 3 µl droplets of this mixture were templated on superhydrophobic surfaces to obtain patchy particles. Microscopy images of these particles are given in the figure below (Figure 5.10). It was observed in the self-

propulsion experiments that Na_2SiO_3 imparted particles did not disintegrate in H_2O_2 solution (see Figure 5.14); therefore, one could conclude that with Na_2SiO_3 it is possible to ensure completely stable particles for self-propulsion purposes.

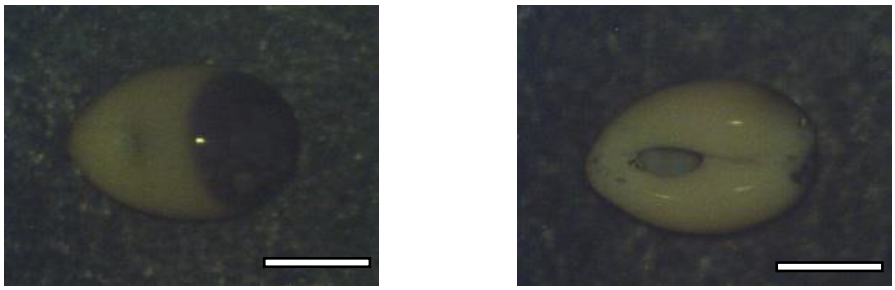

Figure 5.10: 4x microscopy images of a Na_2SiO_3 associated FS based particle (front and back side of the same particle, scale bar: 0.5 mm) (S2, for composition see Table 5.2). Clear separation of the patch was achieved for Na_2SiO_3 associated FS based particle

5.3.2.5 Incorporation of Microfibrillated Cellulose MFC (Sample 3 and 4)

Microfibrillated cellulose (MFC) was another good candidate for further modifications of the particles. It could contribute to improve the structural integrity and by its lower density also to the buoyancy of the prepared particles. Imparting MFC to the patchy particles may be interesting as MFC has unique properties (high surface area, high aspect ratio, high viscosity at low temperatures, being extremely robust to pH and temperature, ability to form strong microfiber films with excellent barrier properties etc.[3]) and highly porous internal structure. As a result, we decided to use MFC to improve the mechanical properties of the patchy particles and introduce additional functionality (for instance higher meso- and microporosity) to the systems.

For MFC-imparted patchy particles, we prepared 1.5 %wt/v MFC (2.08 wt% of the final dry supraparticle). When we took SEM images of these particles, we clearly observed that MFC brings its characteristic fibrillated structure to the system as shown in Figure 5.11. To get a better insight, the central part of the particle is shown 5x magnified on the right side.

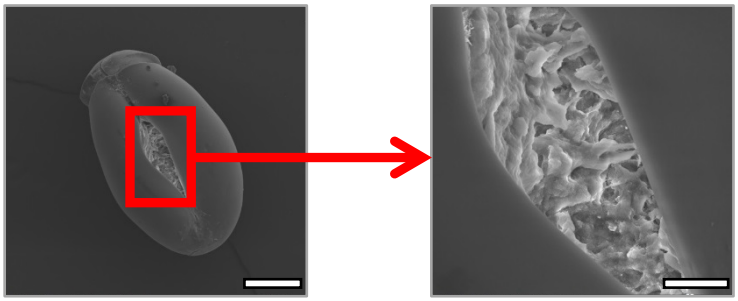

Figure 5.11: SEM image of an MFC-containing FS based particle (S4; for composition see Table 5.2) (Scale bar: left: 300 and right: 60 µm). MFC associated particles are internally more compact with the advantage of fibrillated structure of MFC.

With MFC, we achieved a homogeneously distributed network structure for the internal alignment of the particles with a relatively smoother surface as the evaporation flow occurs from outside to inside. However, due to high viscosity of MFC, the concentration to be added must be adjusted carefully. When we employed MFC with high concentrations (i.e. 10 wt% relative to dry particle and higher), it was observed that the diffusion of the catalytic nanoparticles to the magnet is hindered, apparently due to the crowded internal media and/or binding to MFC. This blocking effect of high concentrated MFC in the particles is clearly visible with both internal and surface inhomogeneity and shown here with the optical microscopy images in Figure 5.12 below.

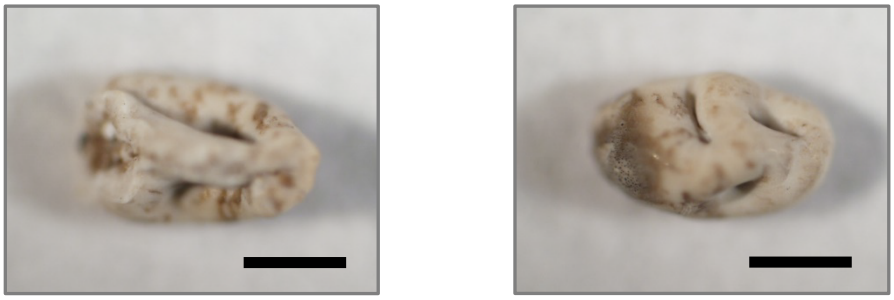

Figure 5.12: Microscope images of MFC-associated FS based particles scale bar: 0.5 mm (S3; MFC content 2.08 wt%).

After observation of irregularities, the MFC amount was decreased and Na_2SiO_3 was additionally imparted (S4) to the particles to obtain more regularly shaped MFC modified particles. In Figure 5.12, optical microscopy images of prepared S4 type particles are illustrated. It was observed that S4 type particles exhibit more clear and homogeneously looking localization of the catalyst when compared to the particles with higher MFC amount (2.08 wt%).

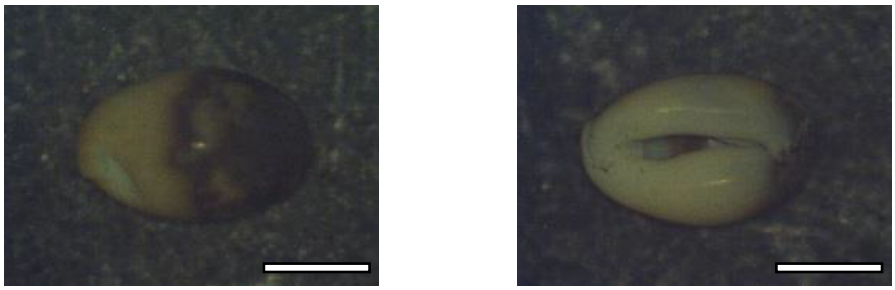

Figure 5.13: Microscope images of MFC & Na_2SiO_3-associated FS based particles (S4) scale bar: 0.5 mm.

5.3.3 Comparison of the Different Particle Types

We have evaluated the outcome from different types of modifications with respect to the stability and performance of the supraparticles under conditions of self-propulsion and summarized in the Figure 5.14. Additionally, we tabulated the results in Table 5.3. Based on the stability, the joint usage of Na_2SiO_3 and MFC (S4) seems to be the best approach to fabricate long-term stable particles that maintain the catalytic activity required for self-propulsion. PS & heat treatment ($S1^a$) is also a proper method by ensuring robust particles with good catalytic activity. Lastly, the results of the particles treated with CH_3Cl_3Si ($S1^b$) shows that this method provides the most stable particles; however, by being over-hydrophobized, these particles does not show any movement due to the lack of contact between the catalytically active parts of the supraparticles and H_2O_2.

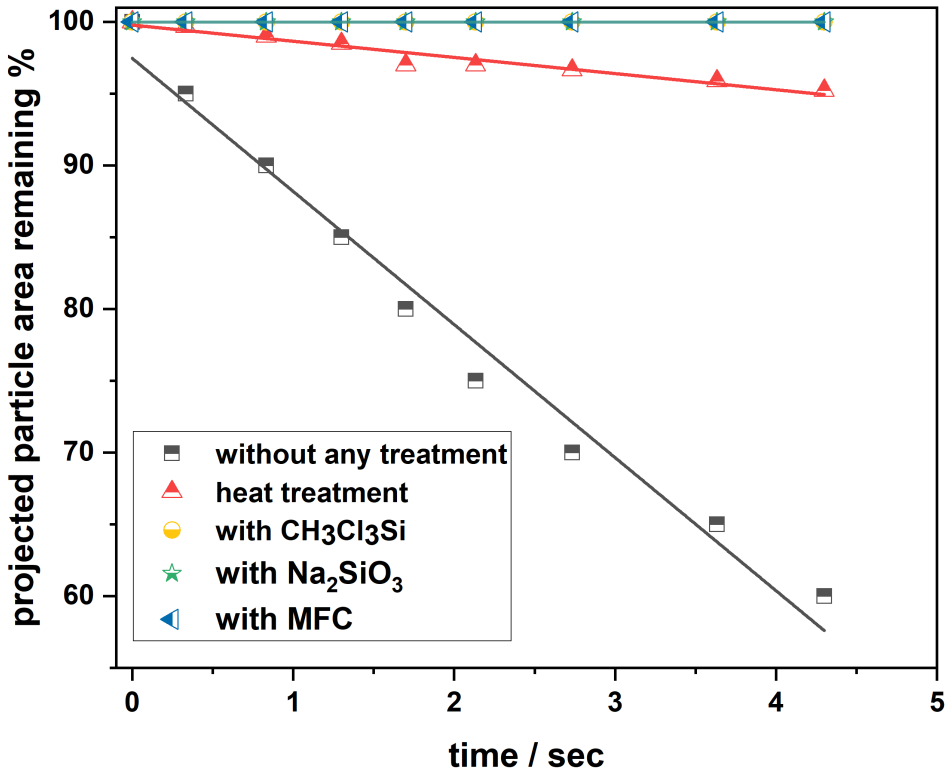

Figure 5.14: Disintegration tendency in 5 wt% H_2O_2 of differently treated supraparticles to provide hydrophobicity. Fast disintegration is observed for the particles without any treatment, slow disintegration is observed for the particles treated with heat and lastly for the particles treated with CH_3Cl_3Si and Na_2SiO_3 no disintegration is observed.

We investigated disintegration behavior of the particles when they were placed in 5 % H_2O_2 solution. The quantification of disintegration was done with the same technique performed for Figure 5.7 as explained in that section. As explained earlier, S1 type particles, the particles without any treatment, start to disintegrate as soon as they are placed in H_2O_2 solution and loose about 50% within 4-5 seconds. The particles modified with heat treatment could provide much more stable particles with moderate heating conditions (8 hours at 115 °C) when compared to the particles without any treatment, but they still disintegrate to some extent. On the contrary, the particles sintered with CH_3Cl_3Si ($S1^b$) or modified with Na_2SiO_3 & MFC (S4) showed long-time stability and they could be good candidates for self-propulsion purposes.

Table 5.3: Stability and motion performance comparison of the particles (+++: very good; +: poor; -: no motion was observed)

Method	Stability	Motion
PS+Heat	+/++	++/+++
CH_3Cl_3Si	+++	-
Na_2SiO_3	+++	++/+++
MFC	+++	+/++
Na_2SiO_3+MFC	+++	+++

5.3.4 Visualization of the Internal Structure of the Particles

To investigate the properties of the supraparticles prepared, structural characterization is very important. Accordingly, all particles were analyzed with optical microscope to investigate surface characteristics and to evaluate anisometry and body length. However, a deep understanding of the internal structure of the particles is necessary to be discovered for the alignment of the catalytically active Fe_3O_4@Pt nanoparticles and optical microcopy only allow to image the surface. Optical microscopy images were not enough to give detailed information about the internal structure of the supraparticles, indeed it gives very little information on the distribution of the catalytically active Fe_3O_4@Pt nanoparticles, which bears the highest importance for their potential usage as self-propelling particles. From the optical microscopy images, it is clear that the particles have nicely elliptical shape with an “eye-like” dark patch on one side (see Figure 5.3). But still there are open questions: How deep this catalytically active nanoparticles go into the supraparticle, Does the shape of the patch depend on the composition of the supraparticles, and how does the catalytically active nanoparticles align within the particles.

As a potential technique, scanning electron microscopy (SEM) could be a good candidate to address that questions, however in that case one has to cut the particles to investigate the internal structure for the measurement which risks changing the particles’ internal structure. Accordingly, a much less invasive investigation tool, confocal micro-X-ray fluorescence

spectroscopy (CMXRF) was chosen. CMXRF enables us to make elemental imaging of specimen in three dimensions, for our particles with a resolution of roughly 30 µm.[12–14] In addition to higher resolution compared to other techniques, the measurement of the localization of Fe and Pt in the whole particles can be performed without need for sectioning in CMXRF due to the low density of the particles.

For the internal structural analyses of the patchy supraparticles, particles were attached to a carbon tape and multiple experiments on all classes of the supraparticles were performed by means of CMXRF.

The visualized shown here are the virtual slices through the particle with 30 µm distance between the slices and the pixel size is also 30 µm. Intensity distributions of Fe, Pt and the whole particle are collected by visualizing the particle slice by slice in xy and yz projections. With a full XRF spectrum for each pixel, elements can be imaged simultaneously and to obtain net peak intensities, fluorescence peaks were deconvoluted.

5.3.4.1 Localization of the Patch

Localization of the patch for patchy particle preparation with the help of magnetic attraction forces was described in detail in the section 5.2.2.2. We handled two particles with same composition (S2 type) and let one of them dry with magnetic force and the other without magnetic force (Figure 5.15). MSc physicist Leona Bauer (Kanngießer Group-TU Berlin) conducted the CMXRF analyses of the particles and evaluated the data obtained in terms of the intensity distribution of Fe, Pt and the density of the particles.

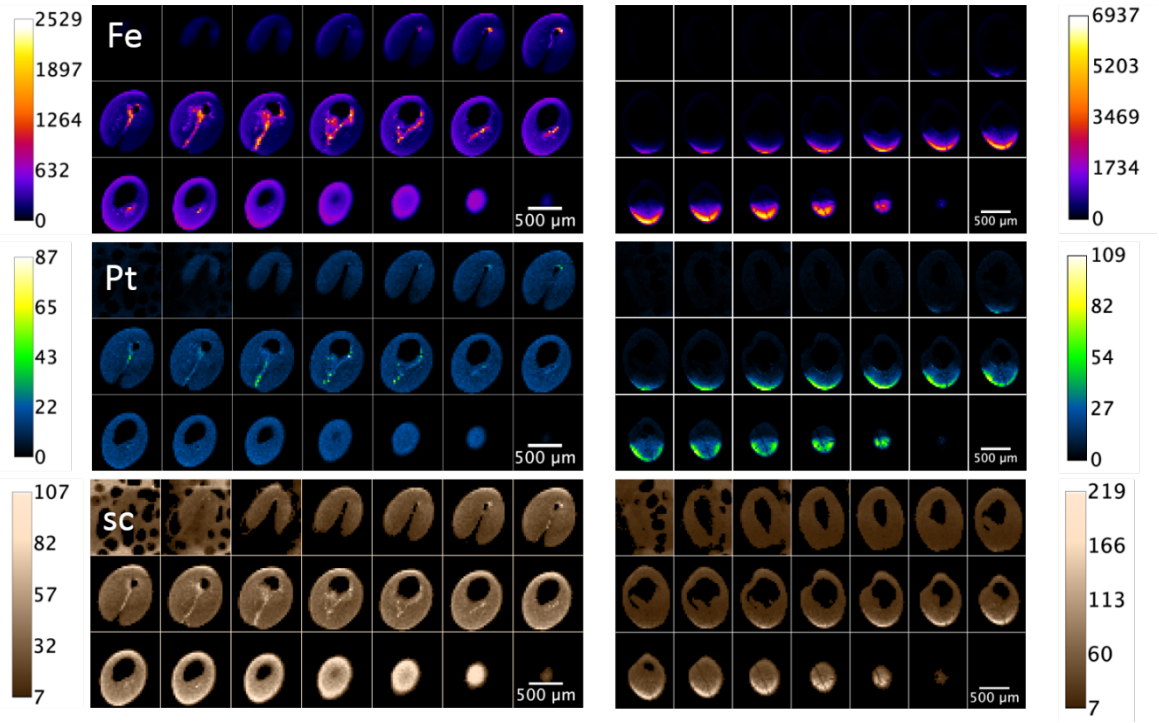

Figure 5.15: Distribution of Fe (top) and Pt (middle) inside a particle of type S2 (Na_2SiO_3) obtained in the absence of a magnetic field (left), and in the presence of a magnetic field (right). The bottom images show the distribution of the density of the particle through the analysis of scattered radiation.

The results are all in agreement with the statements previously mentioned. Without magnetic force, catalytically active nanoparticles are distributed randomly in the particle as seen in the Figure 5.15 on the left. Whereas, in the figure lying on the right, it is clearly seen that Fe_3O_4@Pt nanoparticles are localized in a smaller and predetermined volume in the particle.

5.3.4.2 Heat Treatment of S1 Type Particles

To improve the stability of the particles, as mentioned before, several methods were employed one of which was heat treatment of S1 type supraparticles (PS imparted supraparticles). For the sake of mechanical instability of the particles during self-propulsion, dried PS imparted particles were kept in the oven at 100-120 ˚C for a few hours. This approach served well for the particles' stability and compactness during self-propulsion, however there was not any evidence on the probability of any other structural changes happening besides PS's binding the components inside. Accordingly, an S1 type particle was prepared and CMXRF measurements were taken both before and after heating process (see Figure 5.16).

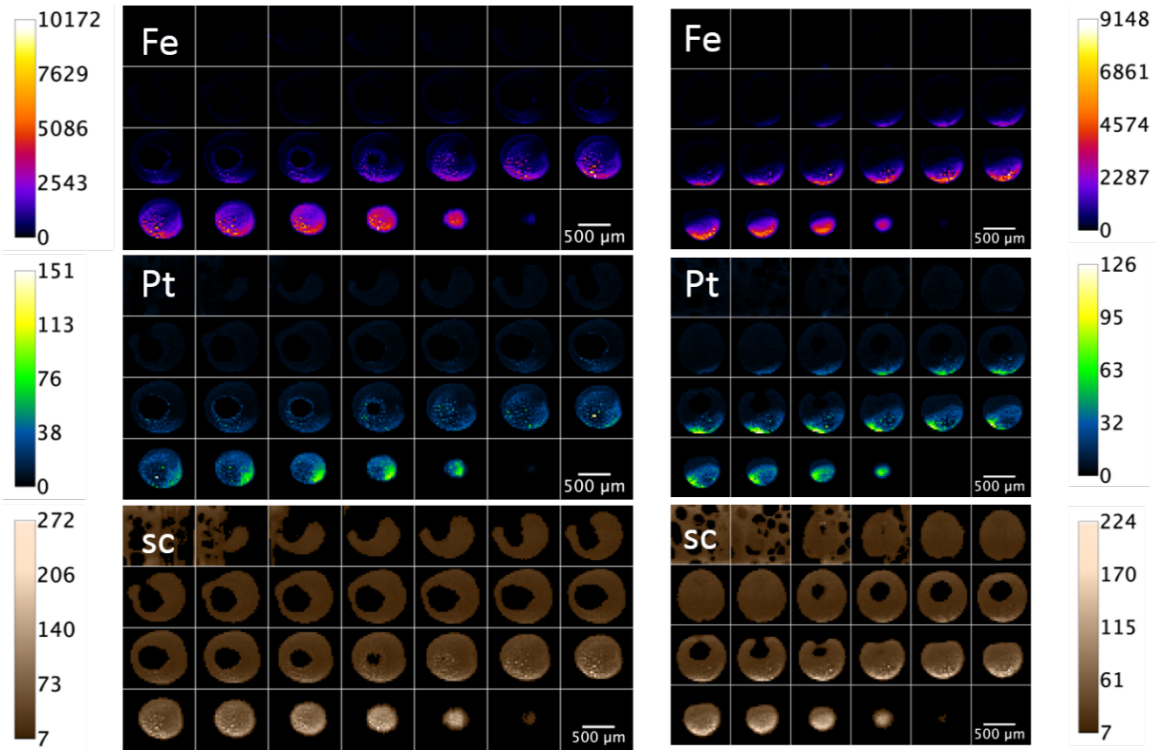

Figure 5.16: Distribution of Fe (top) and Pt (middle) inside a particle of type S1 (PS) before heat treatment (left), and after heat treatment (right). The bottom images show the distribution of the density of the particle through the analysis of scattered radiation.

The spectra of the particle taken before (on the left) and after (on the right) heat treatment were given in Figure 5.16. It was observed that the alignment of the Fe_3O_4@Pt nanoparticles did not change inside the particle after heat treatment, i.e. position of the patch remained stable. This result confirms that the approach based on heating of the particles in order to improve the mechanical stability of the particle, is a totally reliable method.

5.3.4.3 Visualization of the Stable Anisometric Patchy Particles

For the structural investigations of the stable patchy particles prepared for self-propulsion purposes, twelve particles from all suitable classes (S1, S2 and S4) were chosen for CMXRF measurements and one representative result is shown here in Figure 5.17.

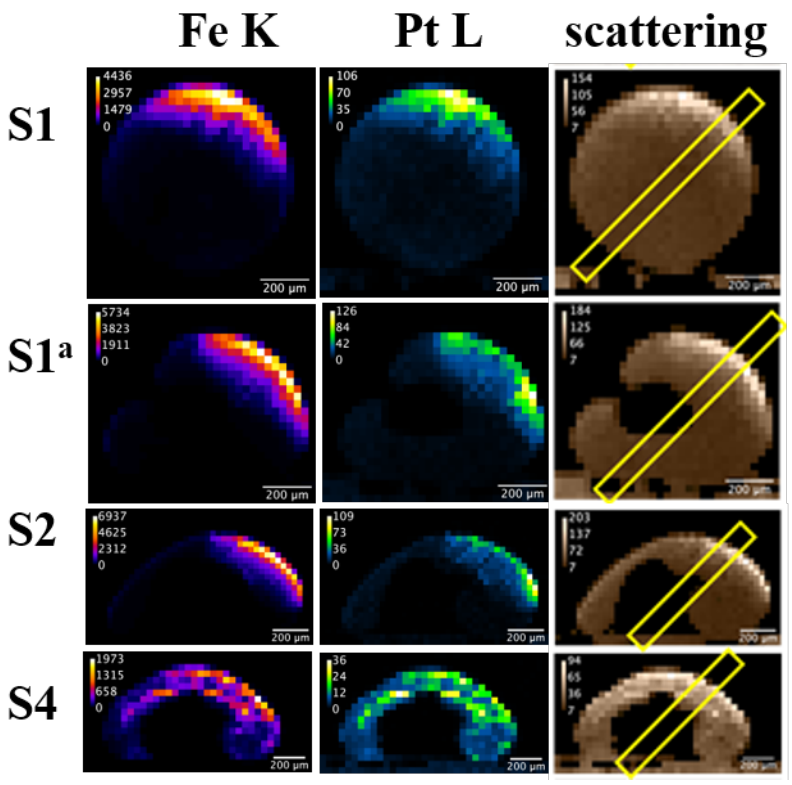

Figure 5.17: Comparison of the typical shape and patch localization (via the localization of the different metals) for the different classes of supraparticles

For S1 type, in PS imparted supraparticles, a well-defined patch localization is seen. In addition, as it was mentioned previously in section 5.3.4.2, heat treatment does not change any further diffusion of Fe_3O_4@Pt nanoparticles so as the self-propulsion properties. The particles modified with Na_2SiO_3 (S2) shows a clear patch separation. Finally, in S4 type particles, modified with Na_2SiO_3 and MFC, patch formation does not seem to be localized well-defined as diffusion of Fe_3O_4@Pt nanoparticles is partially blocked due to the network characteristics of MFC.

From CMXRF analyses on patchy supraparticles, we were able to evaluate the internal alignment of the patch in addition to surface localization. The measurements show that Fe_3O_4@Pt nanoparticles are placed not only on the surface but also up to 200 µm deep, and it is illustrated in Figure 5.18 below. For that purpose, the intensities evaluated from the data are plotted over the relative distance from the surface (position 0 µm).

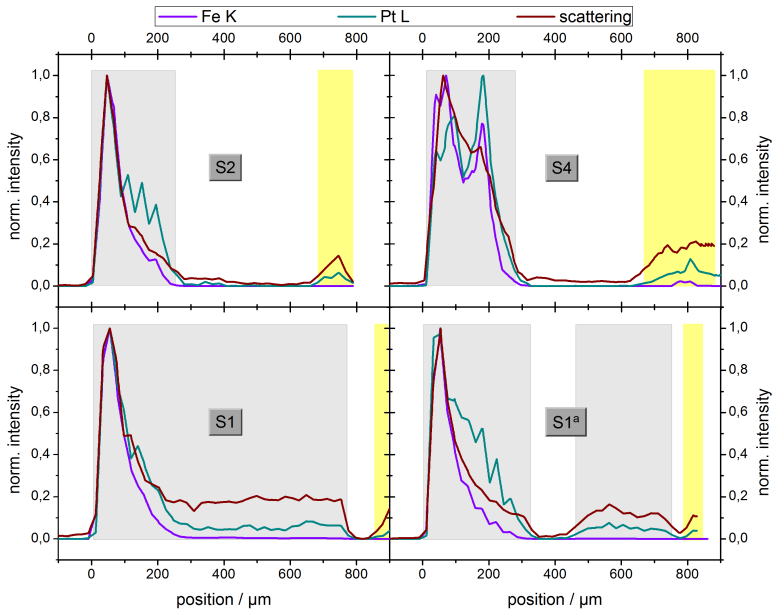

Figure 5.18: Line profiles along the marked paths of Figure 5.17. The intensities are plotted as a function of position with the surface at 0 µm.

Line profiles of the marked paths showed in Figure 5.17 are illustrated in the Figure 5.18 above. There are three regions where the probing volume is inside the particle (grey boxes), the regions without material and the regions where the volume enters or inside the carbon tape that carriers the sample are (yellow boxes).

For S1 and S2 type particles, intensive distribution of Fe_3O_4@Pt nanoparticles is seen on the surface of the particles and distribution gradually decreases as going deeper. The reason of this decrease is the absorption inside the particle as well as the distribution of the elements. First, the attenuation differs from element to element due to the energy dependency of the linear mass absorption coefficient[15]. As Pt is less attenuated than Fe, the decrease in Pt signal is less than the decrease in Fe signal. Second reason is the fact that the signal of Pt is overall much less intense than Fe signal (see Figure 5.17). These two reasons lead to detection of Pt signal at depths while Fe signal is already very low at depths compared to the signal at the surface. For S4 type particles, as it was clearly seen in Figure 5.17 too, the distribution of Fe_3O_4@Pt nanoparticles are seen both on the surface and inside the particle and it was observed that

internal distribution of the nanoparticles are more intense compared to other class of the particles due to the network characteristics of MFC.

5.4 Conclusions

In this chapter, the preparation of the FS-based stable patchy particles was explained in detail. Fumed silica-based mm sized particles were obtained on bent superhydrophobic surfaces by templating 3 µl droplets of the colloidal mixtures via evaporation induced self-assembly. To obtain patchy particles, we synthesized catalytically active patches of Fe_3O_4@Pt nanoparticles (that decompose H_2O_2 and thereby lead to self-propulsion), added to the colloidal mixture and with the help of a magnetic field, the catalytically active nanoparticles were located on a pre-determined side of the particles. However, the main obstacle for these supraparticles is their fragility during self-propulsion experiments in the presence of H_2O_2 as fuel.

Due to hydrophilicity of the particles and the fuel, it was necessary to improve the mechanical stability of the particles to inhibit their disintegration during self-propulsion. To do that, we focused on two methods: Lower hydrophilicity of the particles, and addition of other components. To lower the hydrophilicity, we employed CH_3Cl_3Si by chemical vapor deposition as hydrophobization agent in order to get long-time stable particles. However, even with very small amounts of CH_3Cl_3Si (5-10µl) and very short application times of 3-5 seconds, the particles were over-hydrophobized and they did not show any motion during self-propulsion experiments. Heating was another approach for lowering hydrophilicity as it reduces the number of Si-OH groups. However, this method also brings the deactivation of the catalytic activity as in the previous method resulting in no motion.

As another approach, PS nanoparticles were used to improve the stability of the patchy particles due to its low density PS would contribute to swimming of the particles by decreasing the density of the particles. It was observed that only the addition of PS did not work for stability of the particles during self-propulsion. Therefore, we decided to combine 2 methods: addition of PS and heating. It was observed that above the glass transition temperature of PS, obtained particles were rather homogeneous supraparticles with enhanced stability which are able to self-propel on H_2O_2 solution by being long time stable.

As an alternative approach to improve the stability of the particles, Na_2SiO_3 addition was done. Na_2SiO_3 is a multifunctional material for our system by contributing the stability and eliminating the necessity of NaCl which brings fragility to the particles by dissolving in aqueous solution as Na_2SiO_3 would be used as a control agent for anisometry of the particles instead of NaCl.

In addition to the just described approaches, we also employed microfibrillated cellulose (MFC) as an additive to control the mechanical properties and provide additional functionality. MFC has a significant contribution to the mechanical stability of the particles by aligning inside and binding the components due to its network structure. However, usage of MFC in such a system is tricky as the properties of MFC which bring a notable advantage to the stability becomes a disadvantage for the diffusion of the catalyst in the procedure of preparation of the particles. Due to high network structure, MFC partially blocks the diffusion of the catalytical nanoparticles, hence obtaining patchy particles with clear separation of the patch and the rest of the particle becomes difficult in the presence of MFC. To overcome this obstacle in the presence of MFC, we decided to combine the usage of MFC and Na_2SiO_3. With this combination one could obtain well-defined patch formation and stable particles which are very suitable for self-propulsion.

While making the structural modifications mentioned above, we used confocal micro-X-ray fluorescence spectroscopy (CMXRF) for the visualization of the particles. Compared to optical microscopy and scanning electron microscopy, CMXRF is a very advantageous method with 30µm resolution for our particles as it enables us to visualize not only the surface of the particles but also 30 µm resolution without the necessity of cutting them. The results obtained from CMXRF showed that the Fe_3O_4@Pt nanoparticles are contained rather deeply in MFC-modified particles due to hindered free motion of the Fe_3O_4@Pt by MFC. This phenomenon results in larger patch formation with the distribution of Fe_3O_4@Pt nanoparticles both on the surface and inside of the particles.

In conclusion, the studies in this chapter were pointing to improve the stability of the patchy particles by varying the components to obtain suitable candidates for self-propulsion experiments. With different modification techniques, we achieved to obtain stable particles useful for self-propulsion. With respect to the stability, MFC/Na_2SiO_3 modified particles seem

to be most promising ones. Conducted self-propulsion experiments with the modified particles are given in the following chapter.

5.5 References

(1) Rastogi, V.; Melle, S.; Calderón, O. G.; García, A. A.; Marquez, M.; Velev, O. D. Synthesis of Light-Diffracting Assemblies from Microspheres and Nanoparticles in Droplets on a Superhydrophobic Surface. *Adv. Mater.* **2008**, *20* (22), 4263–4268. https://doi.org/10.1002/adma.200703008.

(2) Ismail, G. A.; Abd El-Salam, M. M.; Arafa, A. K. Wastewater Reuse in Liquid Sodium Silicate Manufacturing in Alexandria, Egypt. *J. Egypt. Public Health Assoc.* **2009**, *84* (1–2), 33–49.

(3) Lavoine, N.; Desloges, I.; Dufresne, A.; Bras, J. Microfibrillated Cellulose – Its Barrier Properties and Applications in Cellulosic Materials_ A Review - 1-S2.0-S014486171200447X-Main.Pdf. **2012**, *90*, 735–764.

(4) Kang, Y. S.; Risbud, S.; Rabolt, J. F.; Stroeve, P. Synthesis and Characterization of Nanometer-Size Fe 3 O 4 and γ-Fe 2 O 3 Particles. *Chem. Mater.* **1996**, *8* (9), 2209-2(1) Kang, Y. S.; Risbud, S.; Rabolt, J. F.; https://doi.org/10.1021/cm960157j.

(5) ICDD. PDF 04-0802, 1997.

(6) ICDD. PDF 11-0614, 1997.

(7) www.hkcm.de https://www.hkcm.de/desk.php/?l=en&fav=61871id (accessed Mar 12, 2019).

(8) Kushwaha, R. Procedure of Animation in 3D Autodesk MAYA: Tools & Techniques. *Int. J. Comput. Graph. Animat.* **2015**, *5* (4), 15–27. https://doi.org/10.5121/ijcga.2015.5402.

(9) Li, L.; Wang, J.; Li, T.; Song, W.; Zhang, G. Hydrodynamics and Propulsion Mechanism of Self-Propelled Catalytic Micromotors: Model and Experiment. *Soft Matter* **2014**, *10* (38), 7511–7518. https://doi.org/10.1039/c4sm01070a.

(10) Czerwinski, F. *Heat Treatment - Conventional and Novel Applications*; Czerwinski, F., Ed.; InTech, 2012. https://doi.org/10.5772/2798.

(11) Wang, J.; Fan, Z.; Wang, H. An Improved Sodium Silicate Binder Modified by Ultra-Fine Powder Materials. *China Foundry* **2007**, *4* (1).

(12) Conti, C.; Botteon, A.; Colombo, C.; Realini, M.; Matousek, P.; Vandenabeele, P.; Laforce, B.; Vekemans, B.; Vincze, L. Contrasting Confocal XRF with Micro-SORS: A Deep View within Micrometric Painted Stratigraphy. *Anal. Methods* **2018**, *10* (31), 3837–3844. https://doi.org/10.1039/c8ay00957k.

(13) McIntosh, K. G.; Cordes, N. L.; Patterson, B. M.; Havrilla, G. J. Laboratory-Based Characterization of Plutonium in Soil Particles Using Micro-XRF and 3D Confocal XRF. *J. Anal. At. Spectrom.* **2015**, *30* (7), 1511–1517. https://doi.org/10.1039/c5ja00068h.

(14) Lachmann, T.; Van Der Snickt, G.; Haschke, M.; Mantouvalou, I. Combined 1D, 2D and 3D Micro-XRF Techniques for the Analysis of Illuminated Manuscripts. *J. Anal. At. Spectrom.* **2016**, *31* (10), 1989–1997. https://doi.org/10.1039/c6ja00220j.

(15) Mantouvalou, I.; Lachmann, T.; Singh, S. P.; Vogel-Mikuš, K.; Kanngießer, B. Advanced Absorption Correction for 3D Elemental Images Applied to the Analysis of Pearl Millet Seeds Obtained with a Laboratory Confocal Micro X-Ray Fluorescence Spectrometer. *Anal. Chem.* **2017**, *89* (10), 5453–5460. https://doi.org/10.1021/acs.analchem.7b00373.

(16) Liu, P.; Ptacek, C. J.; Blowes, D. W.; Finfrock, Y. Z. A Beam Path-Based Method for Attenuation Correction of Confocal Micro-X-Ray Fluorescence Imaging Data. *J. Anal. At. Spectrom.* **2017**, *32* (8), 1582–1589. https://doi.org/10.1039/c7ja00148g.

CHAPTER 6: SELF-PROPULSION of the PATCHY PARTICLES

Scope of the Chapter:

In this chapter, we analyze the self-propulsion of the patchy particles previously obtained. Our purpose was to construct a system consisting of compositionally different particles and to make a correlation between the composition and the motion behavior. For self-propelling systems there are many parameters to be adjusted carefully. As it was mentioned in the previous chapters, for a stable anisometric patchy particle, ionic strength and hydrophobization are the most important parameters. Besides these primary parameters, fuel concentration (H_2O_2 in our case) is another parameter affecting the motion of the patchy particles. Therefore, in addition to investigate the correlation between the composition and the trajectories, we studied the effect of fuel concentration on the average speed of the particles.

6.1 Introduction

In the last few decades, nonbiological micro- and nano-particles performing translational motion by converting chemical energy, have been widely investigated.[1] Starting with the difference between passive motion and active motion, self-propulsion could be explained in a more clear way. Passive motion is the motion caused by any type of flow due to a chemical potential gradient formed by external fields. Active motion, self-propulsion, is defined as the motion generated by the conversion of chemical or external energy into mechanical energy. In other words, self-propelling micro/nano particles could overcome the chemical potential gradient which is responsible for passive motion, leading to active motion.[2]

As it was mentioned in the first chapter, 4 main mechanisms could be discussed for Janus particles: Self-Diffusiophoresis, Bubble Propulsion, Self-electrophoresis and Interfacial Tension Motion Induced Propulsion[3,4]. However, the shape has a crucial effect on the mechanism of the Janus particles. For example, talking about the same mechanism, self-electrophoresis, Janus rods move towards the catalyst[3] while Janus spheres move away from the catalyst[2].

For the systems in which H_2O_2 is used as a fuel to drive the motion, theoretically there are two options; either bubble propulsion or self-diffusiophoresis. Microtubular particles coated with platinum in the interior concave surfaces, generate bubbles from one side and this brings bubble propulsion mechanism; while convex Janus particles show self-diffusiophoresis as they do not generate any visible bubbles in general[5].

6.2 Experimental

6.2.1 Materials

Materials	Specifications	Supplier
Fumed silica (FS) AEROSIL® 90	surface area=90 ± 15 m^2/g	Evonik
PS-latex	d = 0.96 μm, ρ_{solid} = 1.05 g/ml c_{solid} = 10%w/v	Bangs-Labs
NaCl	synthesis-grade, ≥ 99.9%	ChemSolute
Na_2SiO_3	≥18% Na (as Na_2O) basis, ≥60% Si (as SiO_2) basis	Sigma-Aldrich
MFC	grade HP-55, Mw 84 000 g/mol, Mn 21 000 g/mol	Shin Etsu Chemical Co.
MiliQ water	≥ 18 MΩ/cm	
H_2O_2	30% wt	Sigma Aldrich
$NaBH_4$	≥96%	Sigma-Aldrich
$H_2PtCl_6 \cdot 6H_2O$	≥37.5% Pt basis	Sigma-Aldrich
Sodium Citrate Tribasic Hydrate	ACS reagent, ≥99.0%	Sigma-Aldrich
HCl	aqueous, 37%w/w	Merck
NaOH	ACS-grade, ≥ 98%, pellets	Fluka
$FeCl_2 \cdot 4H_2O$	≥ 98%	Sigma-Aldrich
$FeCl_3 \cdot 6H_2O$	ACS-grade, ≥ 98%	Sigma-Aldrich

6.2.2 Experimental Set-Up

Patchy supraparticles prepared previously, described in detail in Chapter 5, were put onto an aqueous 5% H_2O_2 solution in a petri dish (9cm diameter) for self-propulsion one-by-one

(Scheme 6.1). After few seconds, wetting occurred and catalytic patch and H_2O_2 solution came into contact which gives rise to decomposition of H_2O_2 into H_2O (liq) and O_2 (gas). Oxygen gas formation occurred on the patchy side of the particle and when bubbles burst or detached from the particle, the particle started to move in the opposite direction of bubble formation due to conservation of momentum.[6]

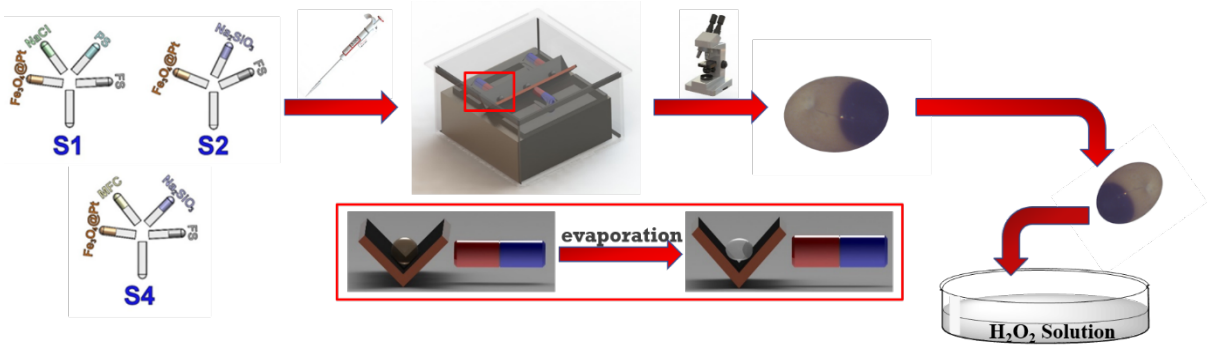

Scheme 6.1: Experimental route in the investigation of self-propelling patchy particles on an aqueous H_2O_2 solution

Observation of the self-propulsion experiments was done with a digital camera (CANON EOS 5D MARK II) and the recorded videos were transferred to a computer to be analyzed. The videos were analyzed with Image J Software.[7,8] The frame rate of the videos was constant (25 frames/sec), and the software gave the trajectories of the supraparticle's motion in pixel units (1088x1920) with the help of Multi Tracker plugin. Frame numbers were converted directly into the time. Trajectories given by the software were evaluated in x- and y- Cartesian coordinates in pixel units. Knowing the diameter of the petri dish, the units of the trajectories were converted into real length (mm scale) by calculating the conversion factor in the software. With all these data in hand, we were able to draw the speed and root mean square displacement graphs of the particles. To make the correlation between the composition and the movement, the particles with similar appearance and dimensions form different classes were chosen.

6.3 Results and Discussion

FS-based structurally modified supraparticles (see Chapter 5) were employed for self-propulsion experiments. Three type of particles with different composition (S1[a], S2 and S4) were used in self-propulsion experiments and the evaluated data is given here with the graphs

in the following sections. Particles from different classes were first analyzed in between in separate sections (6.3.1.1-6.3.1.3). Then we took 3 particles with different composition (from different classes) but same appearance and dimensions and analyzed the motion of these particles to observe the effect of composition on the motion (6.3.2). An important question was the availability of the particles for multiple experiments. In other words, the main concern is that "These particles were suitable to be used in multiple experiments without any damage or not?". To answer this crucial question, three particles from different classes were used for self-propulsion experiments twice (6.3.3) and CMXRF analyses were conducted before and after the experiments (6.3.4). In addition to these studies, self-propulsion experiments of three particles from the same class (S1 type) with similar appearance and dimensions were conducted with 0%, 5% and 10% H_2O_2 solutions to investigate the effect of fuel concentration (6.3.5).

Compositions of the particles belonging different classes are given in the table below.

Table 6.1: Final composition of the different samples prepared and investigated.

Samples / Components wt %	**Class 1 (S1&S1[a]&S1[b])**	**Class 2 (S2)**	**Class 3 (S3)**	**Class 4 (S4)**
Fumed Silica	86.33	84.37	97.09	91.12
NaCl	0.29		0.12	
Fe_3O_4@Pt	1.05	1.03	0.71	1.11
Polystyrene	12.33			
Na_2SiO_3		14.60		6.38
MFC			2.08	1.47

6.3.1 Motion Analyses of S1, S2 and S4 Type Particles

In Chapter 5, stability and motion ability of the particles were explained in detail while preparation of the patchy supraparticles was described. More than 300 particles in each class were prepared and around 100 of them for each class were used for self-propulsion

experiments. The reason why we chose only 1/3 of the particles prepared for self-propulsion experiments was the necessity of a well-defined systematic shape and appearance of the particles to describe and allocate the motion behaviors of the particles more accurate. In the following subsections, the motion behavior of the particles from different classes will be explained separately.

Table 6.2: Properties of S1, S2 and S4 type particles chosen to be illustrated

Particle/ Properties	**Anisometry/ (unitless)**	**Body Length (mm)**	**Average Speed ($mm.sec^{-1}$)**
$S1^{1-4}$	1.24-1.63	1.08-1.20	0.60
$S2^{1-4}$	1.18-1.29	0.84-1.06	0.41
$S4^{1-4}$	1.35-1.62	1.02-1.19	0.32

6.3.1.1 Motion Analyses of S1 Type Particles

Herein, the particles in a certain range of dimensions from Class 1 were picked to be reported to characterize the motion of this class. The properties of the particles chosen to be reported in this section is given below in the Table 6.2. Average speed of the particles from Class 1 was calculated as 0.60 mm/sec and obtained by evaluating more than 20 data set, however 4 particles ($S1^{1-4}$) were chosen to be shown here to represent this class.

S1 type particles, as it was mentioned in the previous chapter, have a clearer separation between the patchy part and the rest, due to the internal alignments of the components. The localization of the patch has a prominent effect on the motion abilities and the trajectories of the particles as expected. With a well-defined boundary of the patch, S1 type particles show smoother translational motion when compared to S2 and S4, which will be explained in detail in the following subsections. The trajectories, obtained from the data of the videos with the help of the software, of 4 particles are shown below (see Figure 6.1). Once decomposition of H_2O_2 starts after wetting, bubble formation may occur at different spots on patchy side. With a clear boundary of the patch mainly localized on the surface rather than inside, bubbles formed

at different spots contribute the motion together as the distance between the spots are not too long to inhibit each other. This prevents chaos during motion resulting in a smoother trajectory without many oscillations and circling tendency.

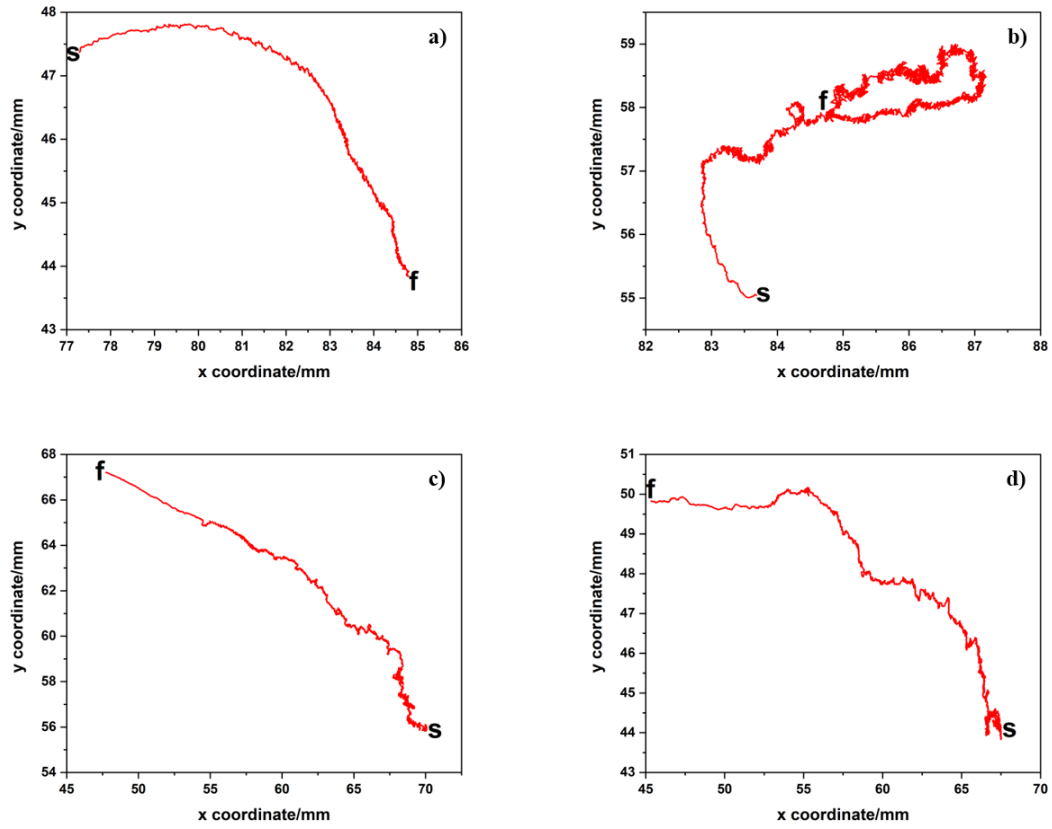

Figure 6.1: Separate trajectories of the patchy particles swimming on 5% H_2O_2 a) $S1^1$, b) $S1^2$, c) $S1^3$ and d) $S1^4$. S and F represent starting and finishing point of the trajectories respectively.

With the evaluated data, instantaneous average speed distribution (between each frame, which is 0.04 s) histograms were drawn (see Figure 6.2). The average speeds of the particles during the whole motion were also calculated and marked with red in the histograms. Based on the histograms, the average speeds of the particles were found as 0.52, 0.64, 0.66 and 0.54 mm/sec for $S1^1$, $S1^2$, $S1^3$ $S1^4$ respectively. Average speed distributions of the particles from Class 1 show similar tendency as it is seen in the figure. The columns concentrate in between 0.2 and 0.8 mm/sec with a mutual peak at 0.2 mm/sec and a steady decrease right after the peak.

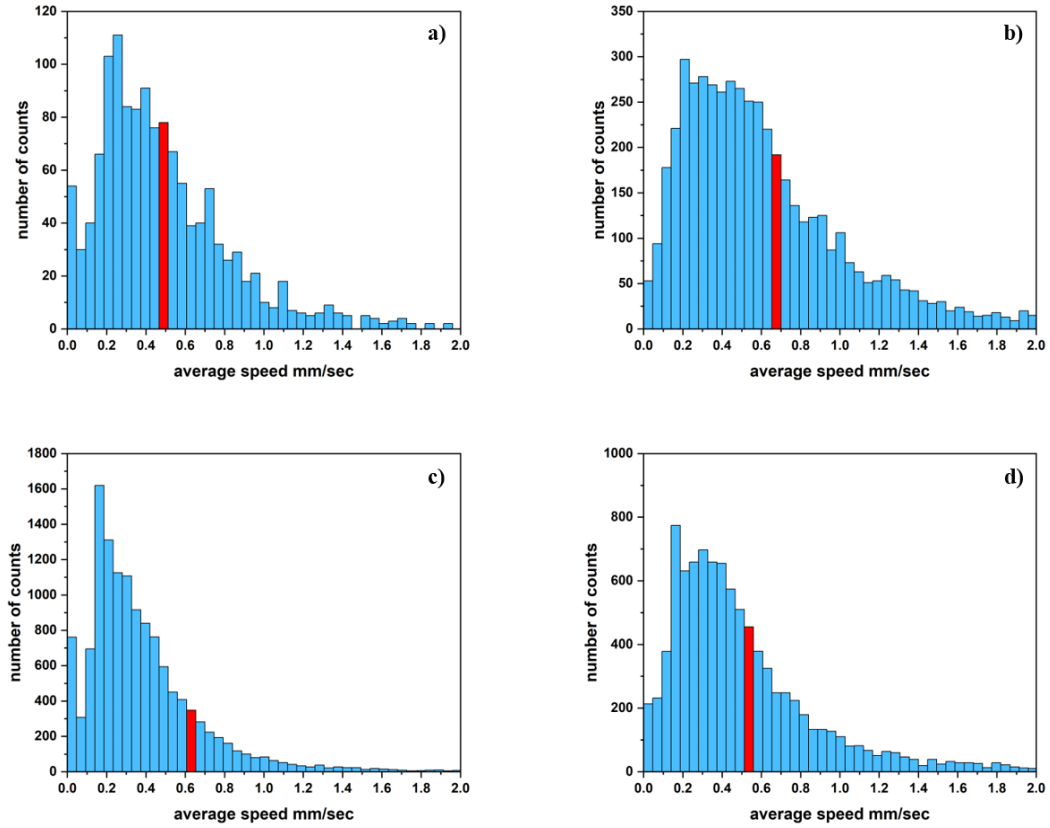

Figure 6.2: Speed distributions of the patchy particles swimming on 5% H_2O_2 a) S1[1], b) S1[2], c) S1[3] and d) S1[4]. (Red columns represent average speed.)

6.3.1.2 Motion Analyses of S2 Type Particles

In this section, the particles belonging to Class 2 were handled to investigate the motion characterizations. Due to the composition of this class, prepared particles were lower in anisometry when compared to Class 1 (see Table 6.2). By having 14.60 % wt (in the dried particle) Na_2SiO_3, S2 type particles have very compact and dense alignment inside which causes difficulties in elongation during evaporation of the H_2O in the droplet in the preparation process. That`s why, the particles from Class 2 show lower anisometry and body length compared to S1 and S4. Anisometry values of the analyzed particles to be shown here change in between 1.18 and 1.29 with 0.9 mm body length at average (see Table 6.2) while they were found as in between 1.24-1.63 with 1.15 mm average body length in Class 1 particles. Average speed of all S2 type particles prepared for this study was calculated as 0.41 mm/sec.

S2 type particles have porous internal structure as it was described in the previous chapter. Being porous and compact, the localization of the patch is not as well-defined as in the Class 1. Internal complexity of the S2 type particles inhibits the diffusion of the catalyst (Fe_3O_4@Pt) nanoparticles to some extent during the evaporation of the droplet which results in some of the nanoparticles are being trapped inside the particle. Therefore, catalytic nanoparticles are localized not only on the surface but also inside the particle which is proven with CMXRF studies in previous chapter. This localization of the catalytic nanoparticles brings a bubble crowd surrounding the particle during self-propulsion. Bubble formation occurs at different spots as in S1, but these spots are further to each other in S2. The bubbles formed at different spots in Class 2 particles, cross other`s paths which breaks a smooth translational motion and ends up with a little chaos during movement. This chaos appears as oscillation like zigzags and small circles in the trajectories (see Figure 6.3).

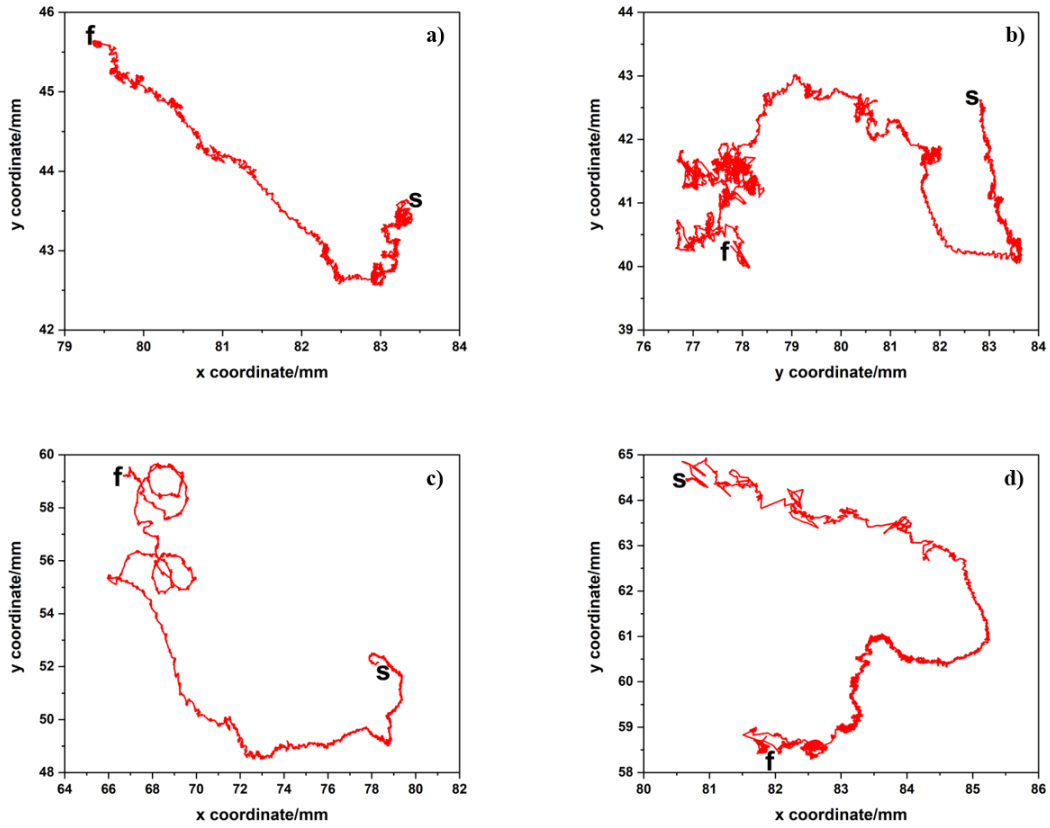

Figure 6.3: Separate trajectories of the patchy particles swimming on 5% H_2O_2 a) S2[1], b) S2[2], c) S2[3] and d) S2[4]. S and F represent starting and finishing point of the trajectories respectively

With the data obtained from the analyses of the trajectories, average speed distribution (between each frame, which is 0.04 s) histograms were drawn (see Figure 6.4). Red columns represent the average speed during the whole motion of the particles and calculated as 0.41, 0.55, 0.37 and 0.47 mm/sec for S2^{1}, S2^{2}, S2^{3} S2^{4} respectively. The histograms show similarities with the ones obtained for Class 1 particles. The concentration of the columns is observed in the area between 0.2 and 0.8 mm/sec. The highest speed values are seen in between 0.2 and 0.4 mm/sec and the decrease after the hill is detected as an exponential decrease. As expressed before, average speed of the self-propelling particles of this class was found as 0.41 mm/sec, lower than Class 1 due to the differences in internal alignment of the particles, as expected.

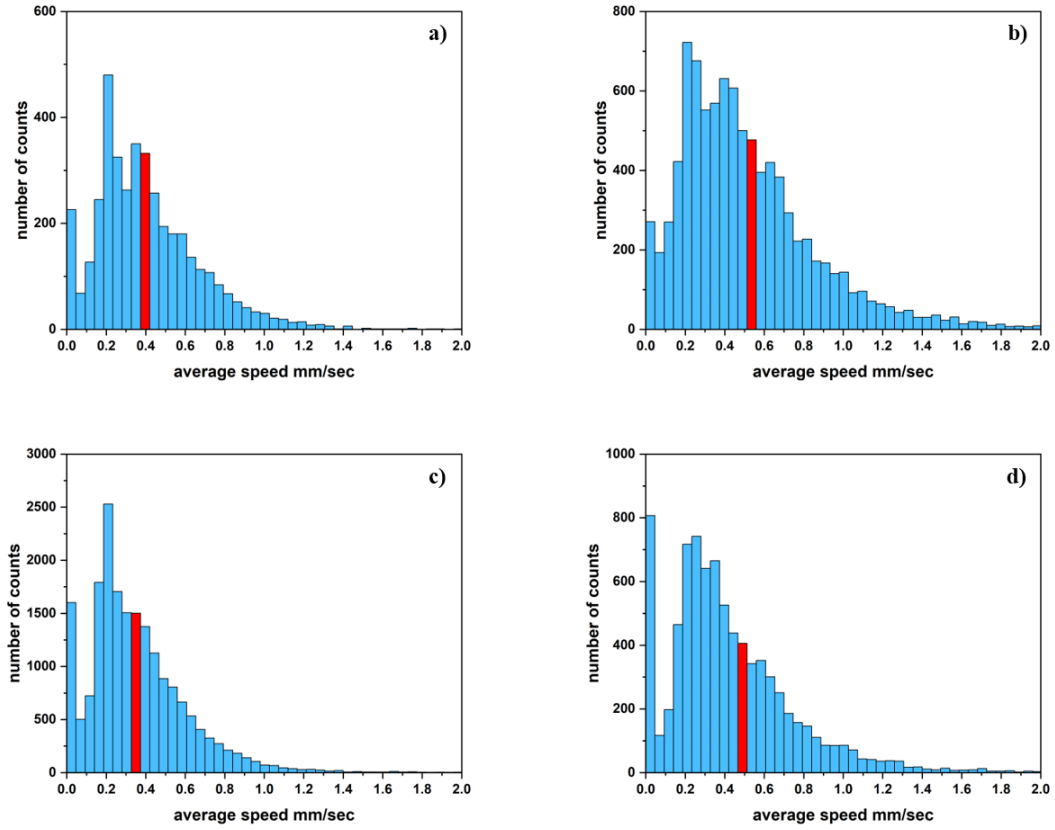

Figure 6.4: Speed distributions of the patchy particles swimming on 5% H_2O_2 a) S2^{1}, b) S2^{2}, c) S2^{3} and d) S2^{4}. (Red columns represent average speed.)

In the previous chapter, 4 modification techniques to obtain stable patchy particles suitable for self-propulsion were explained in detail. However, S3 type particles (Class 3) were not

discussed here due to irregular distribution of catalytic nanoparticles caused by high network structure of MFC (see Figure 5.11). As there is not a clear separation of the patch and the rest of the particle seen in S3 type particles, they are not considered for self-propulsion experiments and further analyses.

6.3.1.3 Motion Analyses of S4 Type Particles

As in the cases of S1 and S2 type particles, S4 type particles were handled for self-propulsion for the investigation of the motion analyses. Experiments were done under same conditions and analyses were done by using the same method. After encountering with the problem of bubble crowd resulting in drowning of the particles in Class 2 and disordered localization of the patch in Class 3, the necessity of the combination of these two classes has arisen. Class 4 was formed by decreasing the weight percentages of Na_2SiO_3 and MFC (in dried particle) used in Class 2 and Class 3 to eliminate the disadvantages caused by crowded internal media.

The particles taken to be analyzed in this section were selected similar to the Class 1 particles with respect to dimensions (see Table 6.2). Average speed of all particles in this class was calculated as 0.32 mm/sec.

To represent Class 4, 4 particles were chosen to be shown here. By combining Na_2SiO_3 and MFC, prepared particles showed excellent stability. Particles` being stable is a necessity to prevent disintegration during self-propulsion, however as it was seen in Class 2 it might become a disadvantage for the localization of the patch. The boundary of the patchy part and the rest in Class 4 is not as clear as in Class 1. The contribution of Na_2SiO_3 and MFC bring the particle a very nice porous and network internal structure. However, this results in difficulties in the diffusion of the catalytic nanoparticles during evaporation of the droplet. It was observed and proven that catalytic nanoparticles were localized not only on the surface but also inside the particle as in Class 2 with more nanoparticles trapped inside when compared to Class 2. This phenomenon causes chaos like in Class 2 particles during self-propulsion and this chaos is clearly seen in the trajectories of the particles (see Figure 6.5). Class 4 particles have a high tendency to make oscillations/ zigzags and small and big circles while swimming on H_2O_2 solution. During self-propulsion experiment, bubble crowds surrounding the particles for Class 4 were not often observed as in Class 2. There are two reasons decreasing this confusion in

Class 4 particles: less Na_2SiO_3 compared to Class 2 and the benefit of the network structure of MFC. Although being very compact and dense, particles inhibit H_2O_2 and the bubbles` fluctuations and contribute in balancing hydrodynamic instabilities to some extent by having a network structure inside.

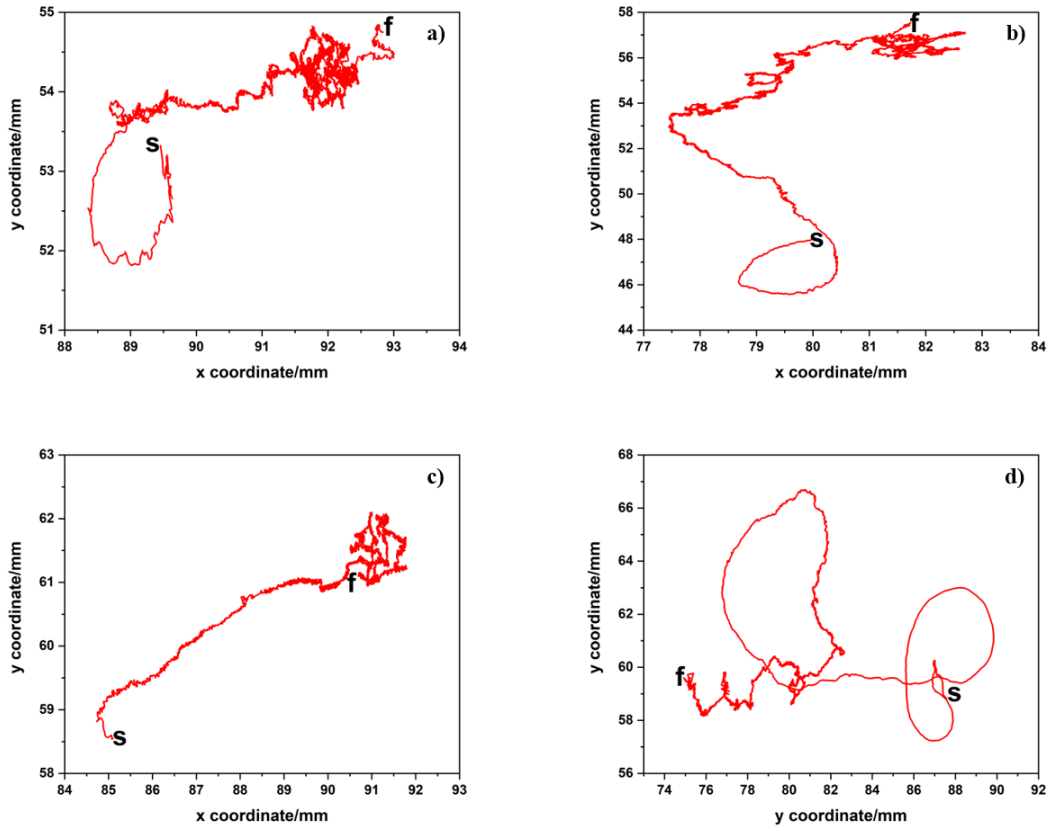

Figure 6.5: Separate trajectories of the patchy particles swimming on 5% H_2O_2 a) $S4^1$, b) $S4^2$, c) $S4^3$ and d) $S4^4$. S and F represent starting and finishing point of the trajectories respectively

As it was mentioned above, the average speed of the particles in Class 4 was found as 0.32 mm/sec. Instantaneous speed distributions of the 4 particles shown here were drawn with histograms and showed in below (see Figure 6.6). Average speeds of the particles were calculated as 0.27, 0.29, 0.3 and 0.4 mm/sec for $S4^1$, $S4^2$, $S4^3$ $S4^4$ respectively and marked with red color in histograms. It is seen that columns concentrate in the area between 0.2 and 0.6 mm/sec and the highest speeds were observed at 0.2 mm/sec as in the previous cases. The

prevalence of the speeds above 0.2 mm/sec is at least 2 or 3 times lower than the prevalence of 0.2 mm/sec unlike other classes.

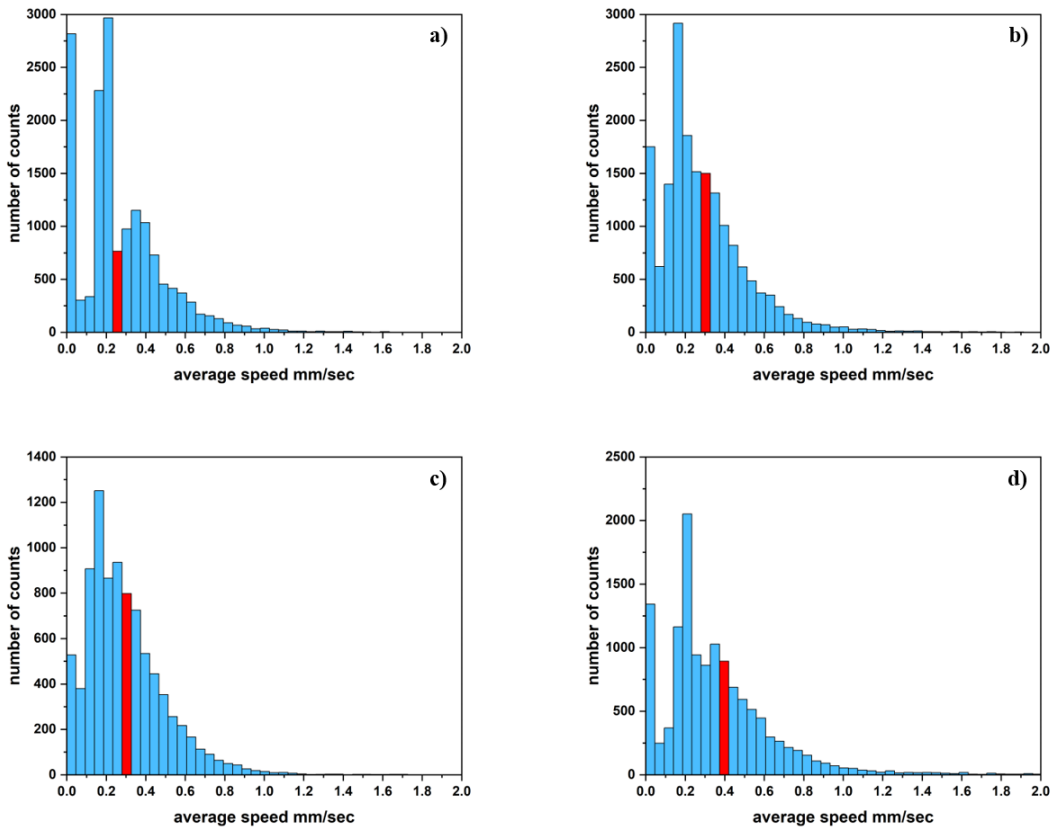

Figure 6.6: Speed distributions of the patchy particles swimming on 5% H_2O_2 a) S4[1], b) S4[2], c) S4[3] and d) S4[4]. (Red columns represent average speed.)

6.3.1.4 Comparison of all Particles Belonging to Different Classes

This study was based on 5 hoops each connected: obtaining anisometric supraparticles, making stable anisometric patchy supraparticles, modifying the particles to be stable for self-propulsion, motion analyses of the self-propelling particles and finding the correlation between the composition and the motion characteristics of the particles. After analyzing different classes separately in previous sections (6.3.1.1, 6.3.3.2 and 6.3.3.3), these 12 particles were taken to investigate the correlation between the Classes (composition), anisometry and average speeds. To do that, anisometry versus average speed of the particles were drawn together (see Figure 6.7).

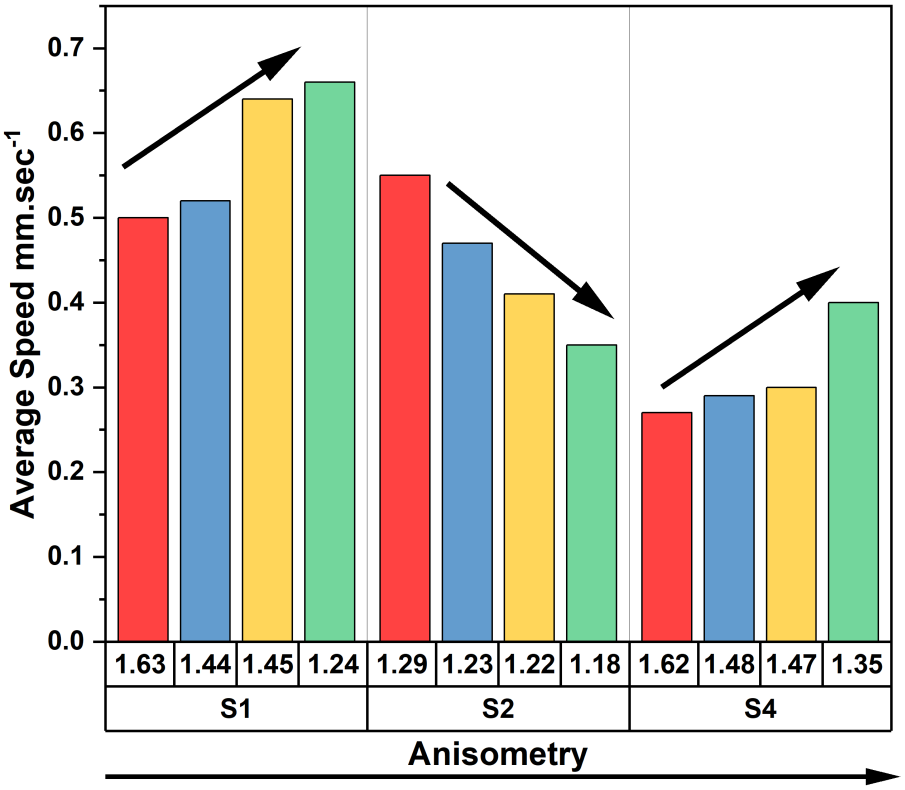

Figure 6.7: Speed distributions of the patchy particles swimming on 5% H_2O_2 from all Classes

As seen in the graph (Figure 6.7), the average speeds of the particles were highest in Class 1, followed by Class 2 particles and Class 4 particles having the lowest speeds which was already expressed in the sections above. The smoothness of the boundary of the patches in the particles determines the average speeds of the particles. Smoother patch localization leads to faster particles as the bubbles formed via decomposition reaction do not inhibit each other and do not blockade the particles. The smoothest patch localization was observed in Class 1 and the least was observed in Class 4, which is in total agreement with the data shown here (see Figure 6.12).

Another observation is, as mentioned previously, graph shows that S1 and S4 type particles could reach higher anisometry values while S2 type particles have less anisometry and look more spherical when compared to S1 and S4. In addition, it was observed that average speed

increases as anisometry decreases for Class 1 and Class 4 and the opposite occurs for Class 2 particles. These two observations stem from a single reason: composition of S2 type particles. Class 2 contains 14.6 %wt Na_2SiO_3 which makes the particles very compact. This compactness prevents elongation of the droplets during evaporation to some extent; therefore, dried particles appear less anisometric compared to other classes. For the anisometry and speed relation, one would expect to see higher speeds at lower anisometry values due to the increase in hydrodynamic instability for longer particles which is totally true for Class 1 and Class 4. However, for Class 2 particles, speed decreases with decrease in anisometry. During self-propulsion, all particles might be surrounded by the bubbles formed. The particles having higher anisometry are not stuck and continue motion while less anisometric particles may be trapped inside the bubble crowd. As a result, S1 and S4 type particles are able to continue motion in case of being surrounded by bubbles while S2 type particles have difficulty due to their shapes.

After analyzing the relationship between trajectory, average speed and anisometry of the particles with their composition, a very important question appears: How consistent are the average speeds of the particles during whole motion? To investigate the consistency of the average speeds of the particles, average speeds were calculated in certain time intervals: 1st 30, 60, 90, 120, 150, 180, 210, 240, 270, 300, 330 and 360 seconds. Evaluated data was drawn and represented with grouped columns separately for Class1, Class 2, Class 4 and all 12 particles together (see Figure 6.8).

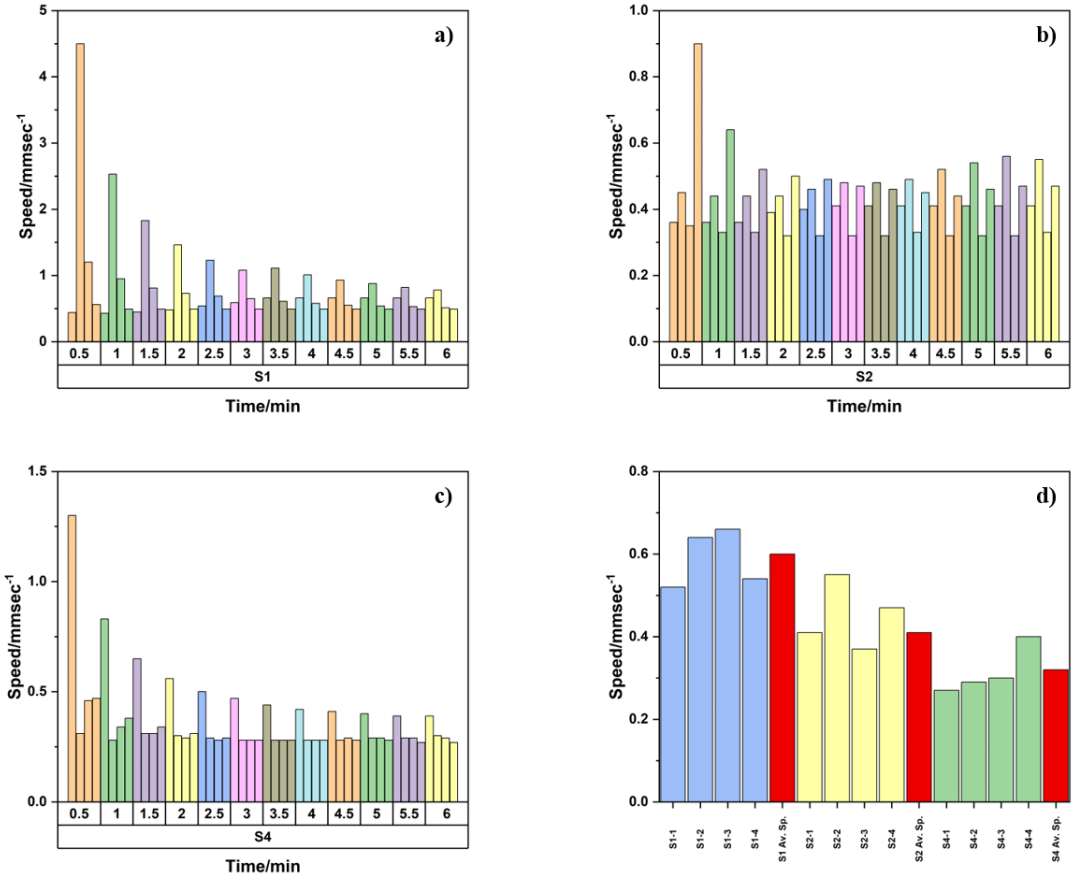

Figure 6.8: Average speed distributions of a) $S1^1$, $S1^2$, $S1^3$ and $S1^4$, b) $S2^1$, $S2^2$, $S2^3$ and $S2^4$, c) $S4^1$, $S4^2$, $S4^3$ and $S4^4$ and d) all 12 particles together

As it is clearly seen from the graphs above, average speeds of the particles are fixed right after 2-3 minutes and this outcome is in agreement for all 12 particles. These results prove that the motion analyses of the particles are definitely reliable for the particles moving at least for 3 minutes. It would not be accurate to describe a similar system moving for 1 or 2 minutes or less as these short time intervals are not enough for the particles to show a systematic behavior.

6.3.2 Motion Analyses of Self-Propelling Particles and the Correlation between the Composition and the Motion

By achieving successful self-propulsion experiments with stable patchy supraparticles, we investigated self-propulsion of the particles with same appearance and different compositions.

To do that, we chose S1[a], S2 and S4 class particles, due to their stability as it was mentioned in the previous chapter, to be investigated. Three particles with similar shape, dimensions and appearance were selected from each class (see Table 6.3).

Table 6.3: Properties of the particles selected from 1st, 2nd and 4th classes for correlation studies

Particle/ Properties	**Anisometry (unitless)**	**Body Length mm**
S1	1.46	1.21
S2	1.45	1.11
S4	1.48	1.10

S1 type particles having NaCl and PS, are more compact and the separation of the patchy part and the rest is more clear. S2 type particles containing Na_2SiO_3 have more porous internal structure, as consistent with CMXRF outcome in the previous chapter, giving rise to easier H_2O_2 intrusion during the experiment. Lastly, S4 type particles include MFC and Na_2SiO_3. Due to Na_2SiO_3 being porous, due to MFC having a network structure internally S4 type particles exhibit more curvature motion, i.e. have a higher tendency to turn more frequent due to internal structure, when compared to S1 and S2. H_2O_2 coming in and going out, has many locational options for S4 type particles due to the internal structure which results in different trajectory obtained from the experiments (see Figure 6.9).

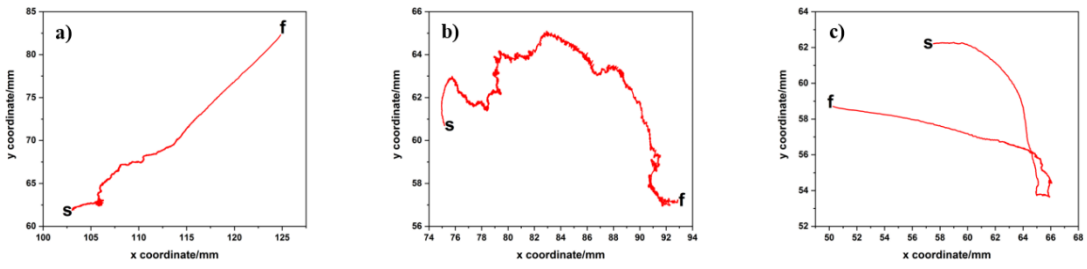

Figure 6.9: Trajectories of the patchy particles swimming on 5% H_2O_2 a) S1, b)S2 and c)S4. Due to more compact internal structure, S1 shows more directional behavior, S2 tends to make a circle in a long time period; S4 makes turning during swimming.

From the data evaluated, we also drew the cumulative distances travelled by the particles. S1, S2 and S4 travelled around 300, 400 and 60 mm in total. For S1, total moving time is 6.7, for S2 11.7 and S4 2.7 mins (Figure 6.10). Total time is not related with the particles' activity, but it is related with the particles' movement. More clearly, when the particles reach to the wall of the petri dish, it is not always easy for them to turn back to solution and continue motion as soon as they touch the wall. Accordingly, the experiments were stopped in case the particles did not turn back to the solution, so total time travelled for motion may be shorter for some particles.

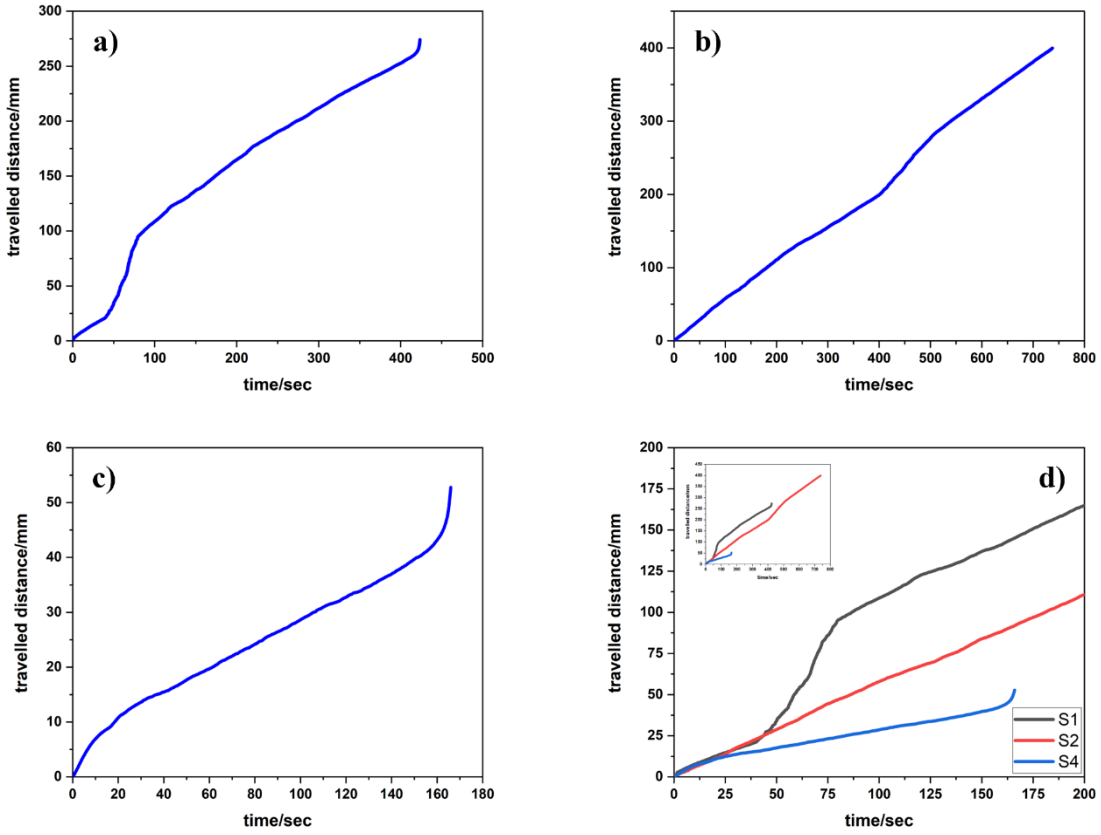

Figure 6.10: Total distances travelled by the particles with respect to time a) S1, b) S2, c) S4 and d) S1, S2 and S4 together [Inset: Total distances travelled by the particles with respect to travelled time specific to each one. (Total travelling time of the particles differ due to adhesion.)]

Average speeds of the particles were calculated by dividing the total distances travelled over total travelling time and found as 0.65, 0.54 and 0.32 mm/sec for S1, S2 and S4 respectively. For self-propelling particles, another term to define speed is body length. Average velocities with respect to body length were also calculated and found as 0.54, 0.49 and 0.29 BL/sec for S1, S2 and S4 respectively. All data evaluated for three particles is tabulated below.

Table 6.4: Properties and average speeds of the particles S1, S2 and S4

Particle/ Properties	**Anisometry (unitless)**	**Body Length (mm)**	**Average Speed ($mm.sec^{-1}$)**	**Average Speed ($BL.sec^{-1}$)**
S1	1.46	1.21	0.65	0.54
S2	1.45	1.11	0.54	0.49
S4	1.48	1.10	0.32	0.29

In addition to make average speed calculations, speed distributions of the particles per frame (0.04 sec) were obtained with the instantaneous speeds from the data evaluated and illustrated with a histogram (see Figure 6.11). Based on the histograms, the columns representing the speeds show a dense distribution between 0.2 and 0.6 mm/sec for all particles. However, for S1 the distribution looks more regular, whereas for S2 and S4 the distributions show some peaks at low speeds and the overall structure of the histograms do not show any defined trend, especially for S4.

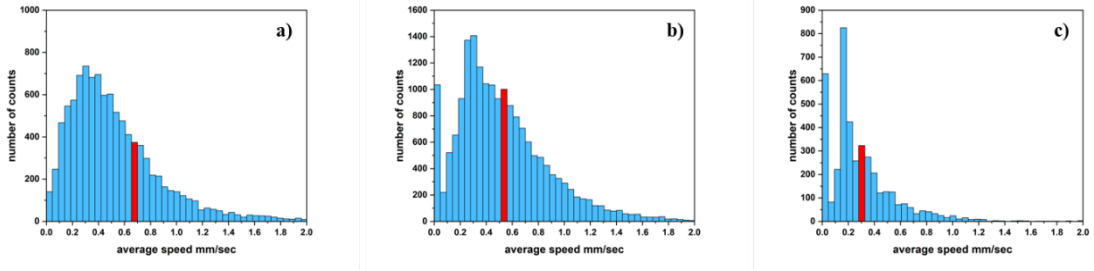

Figure 6.11: Speed distributions of the particles a) S1, b) S2 and c) S4. Columns concentrate at higher speeds for S1 and S2 when compared to S4, which consist of MFC. (Red columns represent average speed.)

In the Figure 6.11, instantaneous speed distributions of 3 particles from the 1st, 2nd and 4th Classes is shown together. Speed distributions of Class 1, 2 and 4 type particles were previously illustrated in the Figures 6.2, 6.4 and 6.6 respectively. Looking at the histograms here, it is clearly seen that the shapes of the histograms of S1 (Figure 6.11-a), S2 (Figure 6.11-b), and S4 (Figure 6.11-c) type particles resemble the ones illustrated in the Figures 6.2, 6.4 and 6.6 respectively. As mentioned before, the particles belonging to the same class show similar trend during self-propulsion while the particles from different classes show different trends due to the compositional differences; therefore, similar trajectories and similar speed distributions are expected to be seen by the particles from the same classes.

In this section, the comparison of the particles from classes S1, S2 and S4 were compared in terms of motion and we found the correlation between the composition and the motion behaviors. All particles belonging the same class have similar tendencies in the motion in terms of trajectories and speed distributions. Here in the figure below, there is an illustration schematically showing the overview of the particles and the area of the angle which includes all potential directions of the motion travelled by the particle. The area of the angle was produced by taking the location of the nanoparticles into consideration.

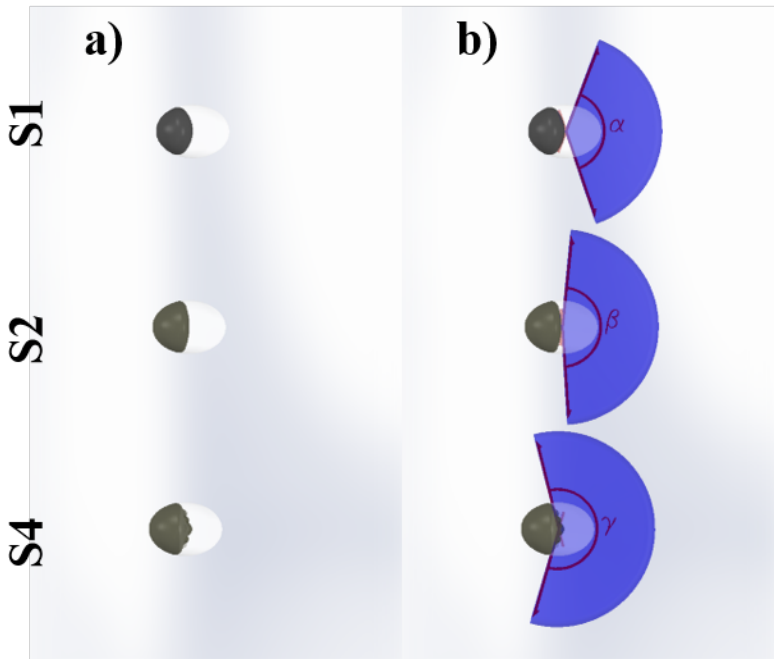

Figure 6.12: a) Schematic illustration of the patchy part boundaries b) Potential angle of the motion directions

As seen in the illustration above, due to the alignment of the nanoparticles, S1, S2 and S4 have different probabilities for the direction of motion. In other words, S4 has more options (potential movement area is wider) when compared to S1 and S2 lies in between S1 and S4, i.e. **α<β<γ**. By having the widest area, S4 has more directional options and especially in case of catalysis at different locations simultaneously, trajectory of the particle becomes more complex when compared to the particles belong to the other classes.

6.3.3 Reusability of the Particles

For the observation of the particles' availability for multiple reactions, self-propulsion experiments were repeated for the same particle. To do that, the particles used in the section 6.3.2 were chosen (see Table 6.3). After the self-propulsion experiments, particles were taken and gently rinsed with dI water. After they dried, they were taken to be used in other self-propulsion experiments. 1st and 2nd experiments were set with the same conditions. 5% H_2O_2 was used as the fuel, experiments were recorded by video camera and the videos were analyzed with the same parameters.

Based on the outcome, it was observed that particles showed similar tendency for the trajectories, which means the shape of the trajectories recorded in the first and the second experiments were very similar. In addition to trajectories, average speed distributions (Figure 6.14) also showed similar trend.

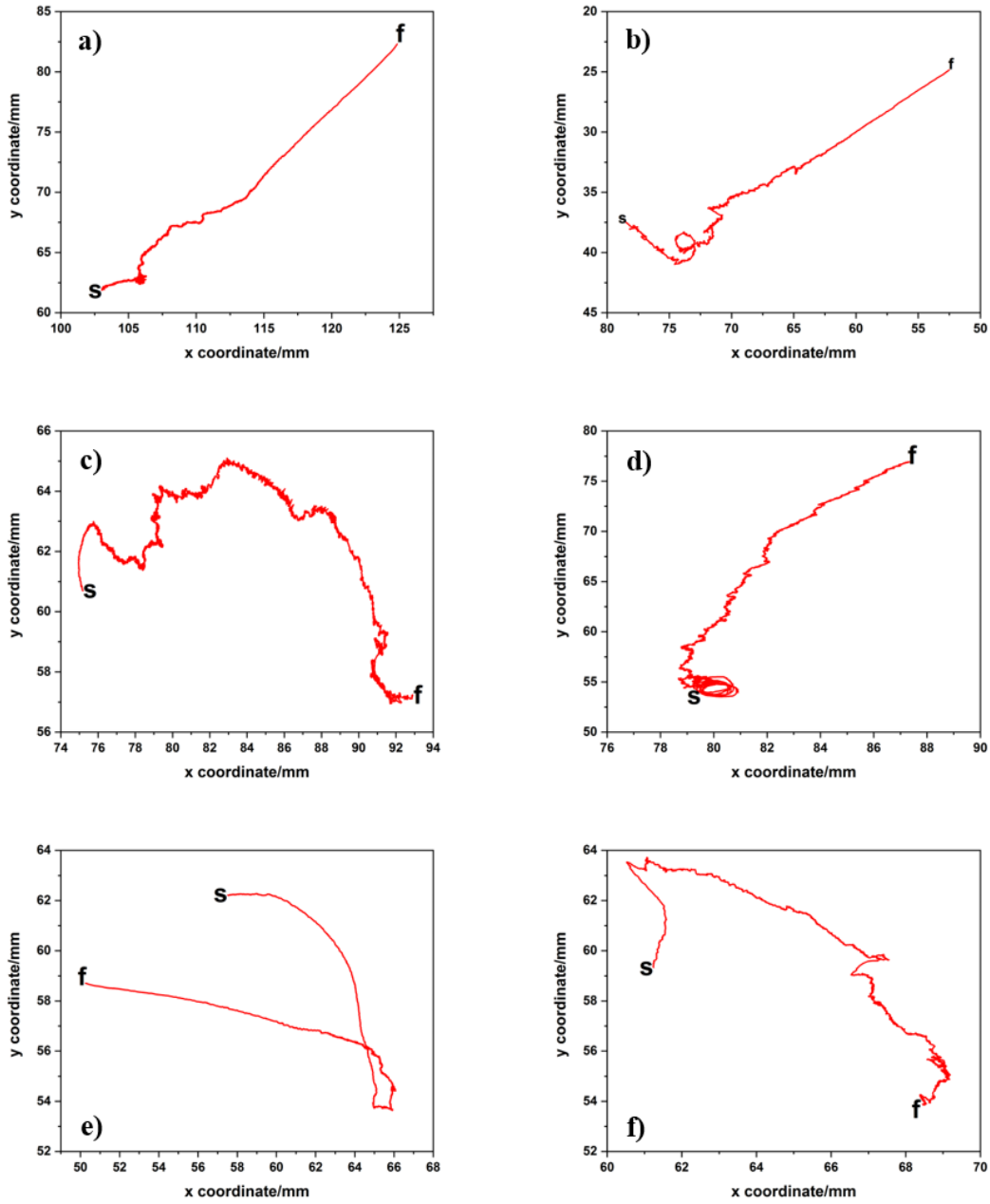

Figure 6.13: Trajectories of S1 (a&b), S2 (c&d) and S4 (e&f) 1st (left) and 2nd (right) self-propulsion experiments

The data obtained were analyzed and we ended up with an expected outcome about average speed of the particles. As it was mentioned before S1, S2 and S4 type particles have different compositions. To improve the stability of the particles, different modifications were taken into account and it was observed that these different modifications resulted in different characteristics in the internal alignment of the particles also in swimming features. In the 2nd experiments, particles moved with slower speeds in general. However, specifically, the average speed of the S1 type particles showed a highest decrease while S4 type particles showed the lowest decrease in the second self-propulsion experiments. The outcome is tabulated in the table below.

Table 6.5: Properties and average speeds of the particles S1, S2 and S4

Particle/ Properties	**Anisometry (unitless)**	**Body Length (mm)**	**Average Speed 1st experiment ($mm.sec^{-1}$)**	**Average Speed 2nd experiment ($mm.sec^{-1}$)**
S1	1.46	1.21	0.65	0.40
S2	1.45	1.11	0.54	0.38
S4	1.48	1.10	0.32	0.28

The decrease in the average speed of S1, S2 and S4 types were calculated around 38.5%, 29.6% and 12.5% respectively. Due to the ingredients, S4 type particles are more compact when compared S1 type and S2 type particles lie in between two. This high rigidity of S4 type is an advantage for the stability of the particles however, it is disadvantageous for the distribution of the components, i.e. difficult to obtain well-defined patch in the particles. Looking at the experimental outcome, the lowest decrease in the average speed of S4, when compared to others, is related with the rigidity and compactness of these particles. By being more compact and rigid, S4 type particles were nearly undamaged after the experiments and as expectedly did not loose too much efficiency.

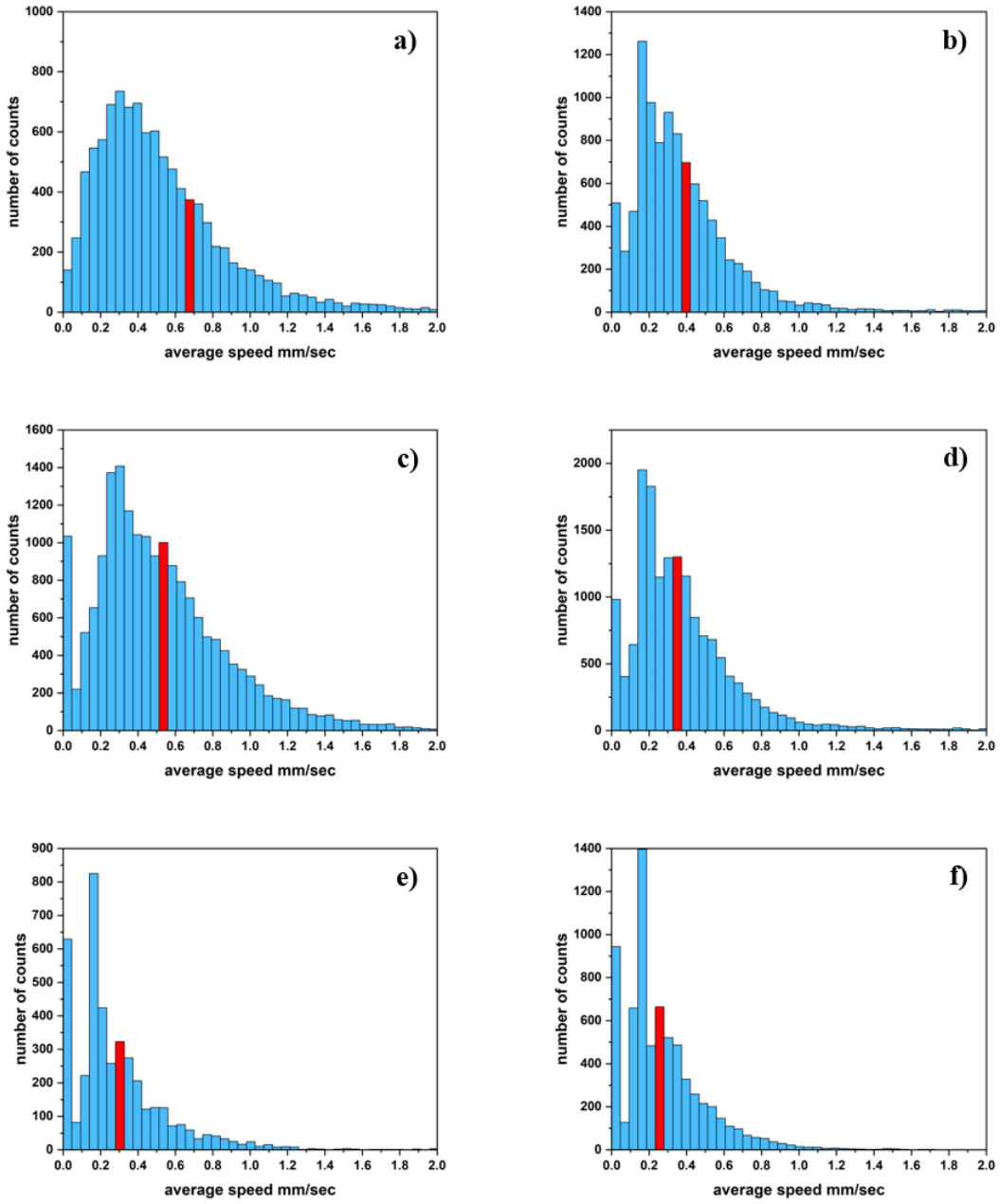

Figure 6.14: Speed distributions of S1 (a&b), S2 (c&d) and S4 (e&f) 1st (left) and 2nd (right) self-propulsion experiments. (Red columns represent average speed.)

When we investigated the instantaneous speeds of the particles for the 1st and 2nd experiments, we found that the speed distributions show the same shapes in between, i.e. the distributions for S1, S2 and S4 for each experiment are in consistency for each particle. For S1, columns concentrate in the interval of 0.2-1.0 and 0.2-0.8 mm/sec in the 1st and the 2nd experiment

respectively. In the histogram of S2, instantaneous speeds concentrate in the interval of 0.2-1.0 and 0.2-0.8 mm/sec in the 1st and the 2nd experiment respectively. Finally, for S4, columns concentrate in between 0.2 and 0.6 mm/sec for both 1st and the 2nd experiments. To look closer to the average speed distributions, 1st and 2nd experiments were drawn together in the Figure 6.15 below.

The decrease in the average speeds of the particles when they are used for second experiments were quantified above and calculated as 38.5%, 29.6% and 12.5% loss for S1, S2 and S4 respectively. The loss in average speed is seen clearly in the graphs below for the particles from Classes 1, 2 and 4. In addition, the graphs show that average speed distribution of the particles belonging to different classes show different characteristics as it was mentioned in previous sections too. Here, we observe that besides having different characteristics, all classes keep their characteristics of the speed distributions for the 1st and the 2nd experiments.

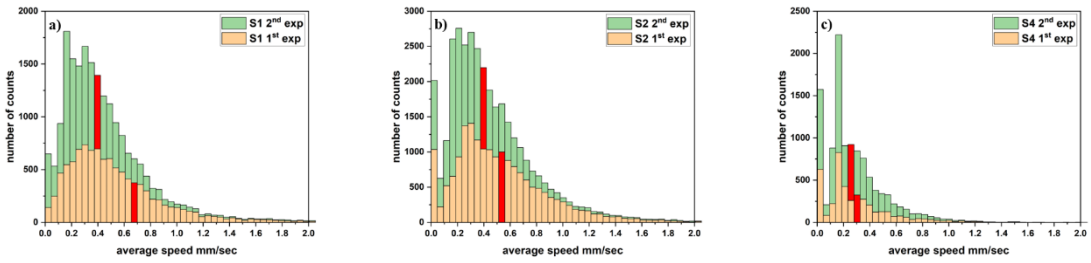

Figure 6.15: Speed distributions of a) S1, b) S2 and c) S4 1st (down-almond) and 2nd (up-green) self-propulsion experiments. (Red columns represent average speed.)

6.3.4 CMXRF Measurements before and after Self-propulsion Experiment for the Investigation of the Reusability of the Particles

For the investigation of the availability of the supraparticles for multiple self-propulsion experiments, CMXRF measurements were conducted for S1 type particle. After the preparation of the particle, it was taken for the measurement. All CMXRF measurements were performed by MSc Leona Bauer with a M4 Tornado with Rh anode material. As CMXRF sample preparation was done by fixing the particle gently between two foils, particle could be handled after the measurement without any damage. Then the particle was used for self-propulsion experiment with 5% H_2O_2. After self-propulsion experiment, particle was taken and

rinsed with dI water gently to eliminate any H_2O_2 residue on the surface. Then we let the particle dry and took CMXRF measurement again. With the data obtained from measurements, intensity vs energy graph was drawn (Figure 6.16).

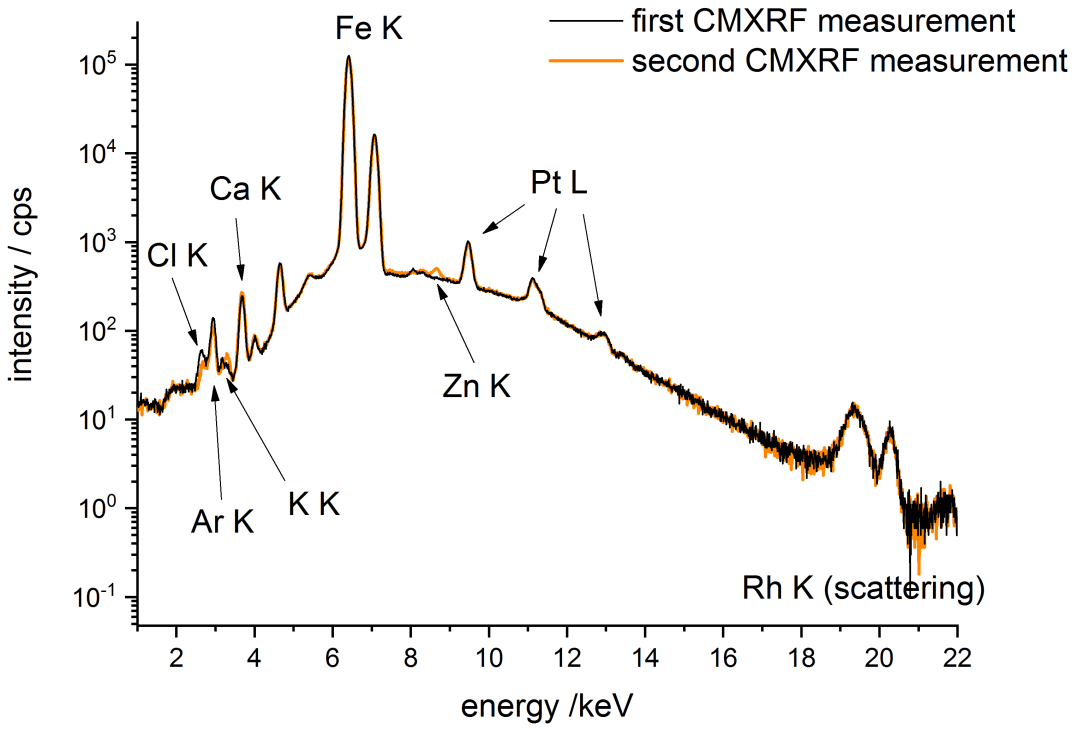

Figure 6.16: Intensity of the elements with respect to energy. Black and yellow line represent the measurement before and after self-propulsion experiment respectively. (The signals of Ca and K come from the foil to hold the particle during measurement.)

The particle (S1) contains FS, NaCl, PS and Fe_3O_4@Pt nanoparticles. Due to the sensitivity of the instrument, we were able to look at Cl, Fe and Pt. Based on the outcome, the intensity signals of Cl, Fe and Pt before the experiment and after the experiment overlap. This means, the distribution of the components of particle does not show any difference before and after self-propulsion experiment, which proves that the particles are definitely suitable for multiple usage in self-propulsion experiments.

6.3.5 Effect of Fuel Concentration

For the fuel dependent propulsions, the average speed of the particles is proportional to the concentration of the fuel. Ke and coworkers reported the results of their study on spherical Pt-Silica particles.[9] By conducting the experiments with these micro spherical half-coated Pt-Silica particles on 15% and 30% concentrated fuel, H_2O_2 in this case, they observed that average speed increases with increasing fuel concentration as in agreement with Howse et. Al.[10]

Here we wanted to investigate the effect of fuel concentration on the average speed of the particles. For that purpose, we chose three S1 type particles with very similar shape and appearance. We called the particles as "swimming particles" so named as SP0, SP1 and SP2. Anisometry and body length values of the particles were equal and calculated as 1.23 and 1.00 mm respectively. To make a control experiment, one of the particles was put on 0% H_2O_2 solution and as expected, it does not show any motion. The other particles were put on 5% and 10% H_2O_2 solutions and self-propulsion experiments were conducted to observe the motion behavior of the particles and to investigate the relationship between the fuel concentration and the average speed.

The trajectories while swimming on H_2O_2 solutions are generically similar, irrespective of the fuel concentration (Figure 6.17).

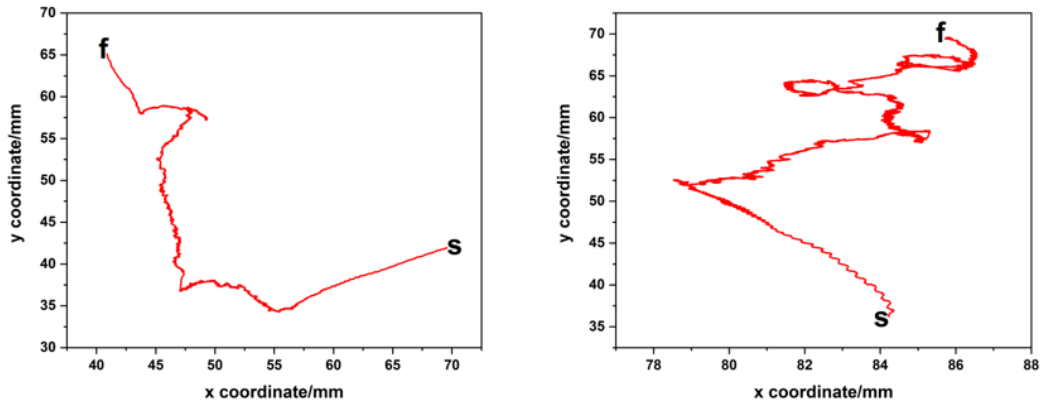

Figure 6.17: Trajectories of the particles put on 5% H_2O_2 (left) and 10% H_2O_2 (right) solutions. S and F represent starting and finishing point of the trajectories respectively.

Both particles move around 6.7 mins, but total distances travelled were 20 and 25 mms for the particles put on 5% H_2O_2 and 10% H_2O_2 solutions respectively (Figure 6.18). This means, as in consistency with the theory, the particle put on 10% H_2O_2 solution moved faster than the one put on 5% H_2O_2 solution.

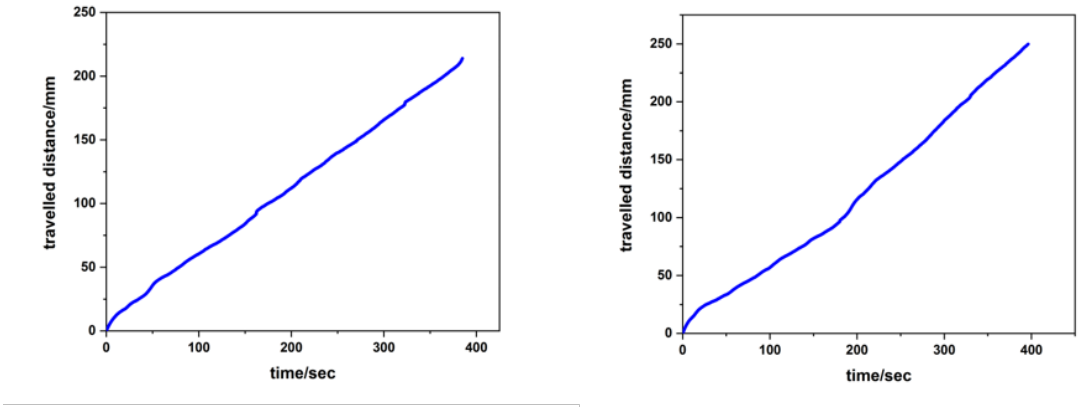

Figure 6.18: Cumulative distances travelled by the particles put on 5% H_2O_2 (left) and 10% H_2O_2 (right) solutions.

Average speeds of the particles were calculated by dividing the travelled distance by total time travelled and found as 0.56 and 0.63 mm/sec for the particles put on 5% H_2O_2 and 10% H_2O_2 solutions respectively. To see the instantaneous speeds of the particles, average speed distribution histograms were drawn (Figure 6.19).

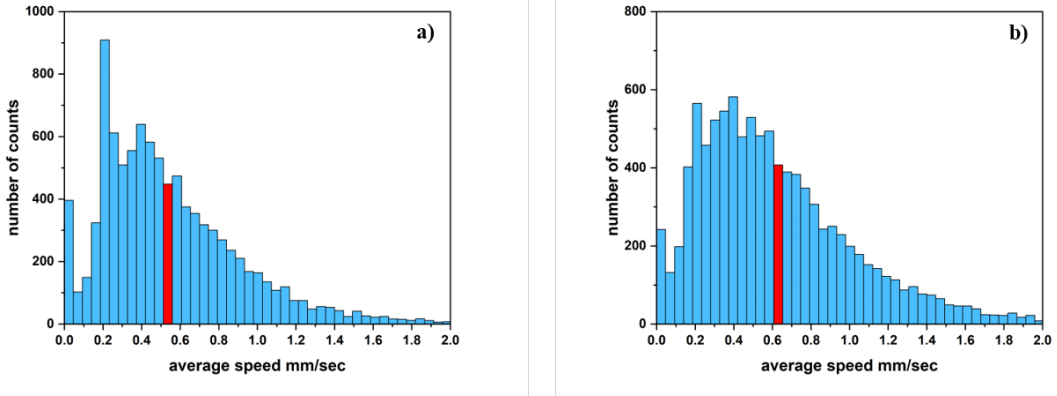

Figure 6.19: Average speed distributions of the particles put on a) 5% H_2O_2 and b) 10% H_2O_2 solutions. (Red columns represent average speed.)

As it is seen in the figure above, the speed columns for the particle put on 5% H_2O_2 solution concentrate at lower speeds when compared to the histogram belong to the particle put on 10% H_2O_2 solution. This result explains that, the particle swimming on more concentrated H_2O_2 solution was faster for both short and long term. However, the difference is relatively small, indicating that effectively one is already approaching an upper limit here and the conversion of H_2O_2 is less limited by the fuel than the available catalyst surface.

Average speeds of three particles, swimming on 0% H_2O_2 (control particle), 5% H_2O_2 and 10% H_2O_2 solution are illustrated in the figure below. As it was mentioned above, the control particle did not move at all, the particle put on 5% H_2O_2 moved with 0.56 mm/sec speed and the particle put on 10% H_2O_2 moved faster than others with 0.63 mm/sec speed.

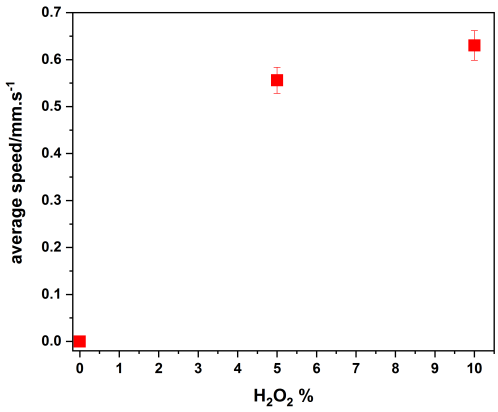

Figure 6.20: Average speed vs H_2O_2 concentration of the particles put on 0%, 5% and 10% H_2O_2 solutions.

The properties of the particles and the speeds are tabulated in the Table 6.6 below. By having the same anisometry and appearance but swam in different conditions, SP2 moved around 15% faster than SP1.

Table 6.6: Properties of the particles SP0, SP1 and SP2

Particle/ Properties	Anisometry/ (unitless)	Body Length mm	H_2O_2 Concentration	Average Speed $mm.sec^{-1}$
SP0	1.23	1.00	0.0	0.00
SP1	1.23	1.00	5.0	0.56
SP2	1.23	1.00	10.0	0.63

6.4 Conclusions

In Chapter 6, our focus was to make the analyses of self-propulsion experiments of previously prepared stable patchy supraparticles. For this purpose, we selected particles belonging to 3 different classes: S1, S2 and S4. S3 type particles were not preferred due to the disordered localization of the catalytic nanoparticles in the particles. Self-propulsion experiments were conducted for around 300 particles in total. We were interested in the differences in the motion behavior of the particles modified with different additives. To do that, first we took 4 particles from each class within a certain body length interval and compared motion behaviors within their own class. Then, 3 particles having same dimensions and appearance but different compositions (from different classes) were taken for comparison.

S1 type particles look like white opaque eye-like particles with a very clear separation of catalytic patch. This appearance brings us to expect smoother trajectories without many circles and zig-zag like oscillations. When we analyzed the motion of S1 type particles, we observed that overall trajectory of the particles show more rectilinear motion with little oscillations either at first (t=0 sec) or last parts of the motion. Rotational motion was not seen in the trajectories. Instantaneous and overall average speed of the particles were calculated and average speed of the particles in this class was found as 0.60 mm/sec. Instantaneous speed distribution histograms of the particles show Gaussian Curve like distribution.

The distribution of the catalytic nanoparticles for S2 type particles was a little less organized compared to S1 type particles, nonetheless the separation of the patch and the rest of the particle looks still clear. However due to this small disorganization in the particles, we ended

up with more complex trajectories when we analyzed the motion of S2 type particles. There are many zigzag-like instantaneous oscillations and a higher rotational motion tendency observed in the trajectories. This chaos was caused by the alignment of the catalytic nanoparticles. Motion in self-propulsion of the particles used was driven by the decomposition of H_2O_2 by catalytic nanoparticles via bubble propulsion. In this case, any disorder in the localization of the nanoparticles would cause confusion with respect to the direction of the particles as multiple bubbles are formed at distant spots simultaneously. Moreover, this crowded media results in deceleration due to the traffic jam of the bubbles. The average speed of S2 type particles were calculated as 0.41 mm/sec, as expected less than S1 type particles, approximately 70% of S1 type particles` average speed. When looking at the instantaneous speed distribution histograms, the effect of chaotic behavior in the trajectories is noticed. While the first parts standing left side of the peak (average speed) have sharp increases at certain time intervals, the right part of the histograms show exponential decreases.

S4 type particles, by bearing MFC in addition to Na_2SiO_3 different from S2 type, was expected to show the most complex behaviors during self-propulsion experiments. Both Na_2SiO_3 and MFC have partially blocking effects on the diffusion of Fe_3O_4@Pt nanoparticles, demonstrated with CMXRF images in Chapter 4, this brings more dispersed nanoparticles and less organized patch, i.e. least clear separation of the patch in all classes. We have already seen the effect of Na_2SiO_3 on the motion behavior of the particles in S2 class, here with the addition of MFC we obtain a more complex system for S4 class. Unclear separation of patch results in formation of multiple bubbles at different spots simultaneously and fibrillar contribution of MFC enables H_2O_2 comes in and out during self-propulsion. Combining these two phenomena, we ended up with the most complex trajectories with full of zigzag like oscillations and rotations. Expectedly, average speed of the particles was calculated as the lowest compared to S1 and S2 classes and found as 0.32 mm/sec (approximately 50% of S1 and 80% of S2). Instantaneous speed distribution histograms of S4 type particles were also shown and the overall shape of the histograms was found rather different than S1 and S2 types. The first part of the histograms shows sharp increases and decreases, and the second part of the histogram standing after the peak columns show exponential decreases with some occasional instantaneous increases.

To get a better understanding of all classes, 12 different particles with different dimensions belonging to the classes 1, 2 and 4 were taken and self-propulsion experiments were conducted. With a complete agreement in previous sections, it was observed that average speeds of the particles were decreasing with the increase in the complexity of the particles, in other words $V_1 > V_2 > V_4$. Another interesting observation was the relationship between the average speed and anisometry of the particles. Normally, one could expect that average speed decreases with increase in anisometry as once the particle gets longer and thinner, it could be more difficult to tolerate hydrodynamic instability formed during motion driven by bubble propulsion. This behavior was seen for S1 and S4 particles. However, for S2 type particles, as anisometry increases speed increases different from other classes. The reason for that is the bubble crowd surrounding the particles during self-propulsion. The particles with less anisometry are easy to be trapped by bubbles while longer and thinner particles are harder as they are better in getting rid of the bubble crowd by using the advantage of their length. In that case, by bearing Na_2SiO_3, S4 particles might be expected to show similar manner. However, as mentioned previously, MFC in the particles brings its network structure to the particles which turns to a big advantage during self-propulsion as fibrillar network helps to balance the hydrodynamic instability and prevents the particles from drawing into bubbles by enabling the fuel comes in and out during motion.

In order to have a closer look at the relationship between the composition and motion behavior of the particles, 3 particles with very similar dimensions but different compositions (one particle from each class: 1, 2 and 4) were taken and put on 5% H_2O_2 solutions for self-propulsion. The trajectories and instantaneous speed distribution histograms are found in a complete agreement with the examples from their classes separately. Average speed values of the particles were calculated as 0.65, 0.54 and 0.32 mm/sec for S1, S2 and S4 respectively.

Besides all those studies stated above, there was another important concern: Are these stable patchy particles available for multiple usages? In order to find an answer to this question, we took the same particles from the previous paragraph and let them self-propel one more time. We observed that obtained trajectories in the 2nd experiments resemble those obtained in the 1st experiments for all particles and these similarities were observed in instantaneous speed distribution histograms too. Average speeds of the particles in the 2nd experiments were 0.40,

0.38 and 0.28 mm/sec for S1, S2 and S4 respectively. The particles lose some efficiency after the 1st experiment by having lower speeds in the 2nd experiments. The losses in average speed of the particles were calculated as 38.5, 29.6 and 12.5 % for S1, S2 and S4 respectively. The reason for losing efficiency with different percentages is related to the rigidity of the particles. All particles are compact and stable, but rigidity and durability of the particles are different due to the components and S4 class is expected to have the highest rigidity while S1 class is expected to have the lowest rigidity. The observation of reusability of the particles was a very valuable outcome, nonetheless it had to be supported by internally visualization of the particles to ensure that particles do not change during self-propulsion experiments. To do that, we took an S1 type particle for CMXRF measurements before and after self-propulsion experiment. The CMXRF data reveal that the concentration of the elements in the particle is the same before and after the self-propulsion experiments, thereby showing that the particles were not harmed by the self-propulsion experiments and are suitable for multiple experiments.

Lastly, we conducted a preliminary study to see the effect of fuel concentration. To do that, we took 3 S1 type particles with same appearance and dimensions. These 3 particles were put on 0, 5 and 10% H_2O_2 solutions (namely SP0, SP1 and SP3 respectively) for self-propulsion experiments. As expected, of 0% no movement is seen, while for 5 and 10% similar trajectories are seen. However, by having a more concentrated fuel, the trajectory for 10% looks a little bit more complex with more frequent zigzags and circles. With the increase in the concentration of the fuel, we increase the interaction between the catalytic nanoparticles and the fuel by increasing the possibility of the number of collisions between them. Consistently, average speeds of the particles were found as 0.56 and 0.63 mm/sec for the particles swimming on 5 and 10% H_2O_2 solutions, respectively.

In summary, in this chapter we achieved to analyze the motion of the particles prepared and modified in previous chapter. It was observed that the manners of the particles seen in their trajectories and calculated average speeds are directly related with the compositions of the particles. With the help of CMXRF studies, we were able to prove the particles' reusability by conducting the measurements before and after self-propulsion experiments. Moreover, the effect of fuel concentration was also shown in the last section with the analyses of 3 identical particles swimming on 0, 5 and 10% H_2O_2 solutions.

6.5 References

(1) Crespi, V. H.; Sen, A.; Kistler, K. C.; Paxton, W. F.; Lammert, P. E.; Cao, Y.; St. Angelo, S. K.; Mallouk, T. E.; Olmeda, C. C. Catalytic Nanomotors: Autonomous Movement of Striped Nanorods. *J. Am. Chem. Soc.* **2004**, *126* (41), 13424–13431. https://doi.org/10.1021/ja047697z.

(2) Yamamoto, D.; Shioi, A. Self-Propelled Nano/Micromotors with a Chemical Reaction: Underlying Physics and Strategies of Motion Control. *KONA Powder Part. J.* **2015**, *32* (32), 2–22. https://doi.org/10.14356/kona.2015005.

(3) Abdelmohsen, L. K. E. A.; Peng, F.; Tu, Y.; Wilson, D. A. Micro- and Nano-Motors for Biomedical Applications. *J. Mater. Chem. B* **2014**, *2* (17), 2395–2408. https://doi.org/10.1039/c3tb21451f.

(4) Sanchez, S.; Soler, L.; Katuri, J. Chemically Powered Micro- and Nanomotors. *Angew. Chemie - Int. Ed.* **2015**, *54* (5), 1414–1444. https://doi.org/10.1002/anie.201406096.

(5) Wang, S.; Wu, N. Selecting the Swimming Mechanisms of Colloidal Particles: Bubble Propulsion versus Self-Diffusiophoresis. *Langmuir* **2014**, *30* (12), 3477–3486. https://doi.org/10.1021/la500182f.

(6) Li, L.; Wang, J.; Li, T.; Song, W.; Zhang, G. Hydrodynamics and Propulsion Mechanism of Self-Propelled Catalytic Micromotors: Model and Experiment. *Soft Matter* **2014**, *10* (38), 7511–7518. https://doi.org/10.1039/c4sm01070a.

(7) Schneider, C. A.; Rasband, W. S.; Eliceiri, K. W. NIH Image to ImageJ: 25 Years of Image Analysis. *Nat. Methods* **2012**, *9* (7), 671–675. https://doi.org/10.1038/nmeth.2089.

(8) Abràmoff, M. D.; Magalhães, P. J.; Ram, S. J. Image Processing with ImageJ Part II. *Biophotonics Int.* **2005**, *11* (7), 36–43. https://doi.org/10.1117/1.3589100.

(9) Ke, H.; Ye, S.; Carroll, R. L.; Showalter, K. Motion Analysis of Self-Propelled Ptsilica

Particles in Hydrogen Peroxide Solutions. *J. Phys. Chem. A* **2010**, *114* (17), 5462–5467. https://doi.org/10.1021/jp101193u.

(10) Howse, J. R.; Jones, R. A. L.; Ryan, A. J.; Gough, T.; Vafabakhsh, R.; Golestanian, R. Self-Motile Colloidal Particles: From Directed Propulsion to Random Walk. *Phys. Rev. Lett.* **2007**, *99* (4), 8–11. https://doi.org/10.1103/PhysRevLett.99.048102.

CHAPTER 7: GENERAL CONCLUSION

In the scope of this thesis, we started with the preparation of FS-based anisometric supraparticles with tunable anisometry. To do that, NaCl, NaF, PEG and Spermine were used as additives to obtain series with changing anisometric systematically. All additives gave remarkable results however to take one step further, we decided to continue with FS-NaCl series. The second step was to prepare FS-based patchy supraparticles for self-propulsion purposes. The mechanism of self-propulsion was bubble propulsion as a result of decomposition of H_2O_2. By knowing that decomposition of H_2O_2 is a metal catalyzed reaction, we synthesized Fe_3O_4@Pt nanoparticles to be used in FS-NaCl based patchy supraparticles. Fe_3O_4@Pt nanoparticles were successfully located on a predetermined side of FS-NaCl based supraparticles which brings us to the third step: self-propulsion experiments. However, we observed that the particles decompose when they are put on H_2O_2 solution for self-propulsion. This brings the necessity of modifications for the sake of stability of the particles during swimming on H_2O_2. To modify the particles hydrophobization (with an hydrophobization agent and heating) was the first method tried and it was figured out that hydrophobization could not be controlled easily. The particles might be partially hydrophobized which does not prevent disintegration, or they might be over-hydrophobized which results in immobile particles due to lack of interaction between the nanoparticles and the fuel. Therefore, we sought for new alternatives for the structural modifications of the particles: additives. The additives used for structural modifications of the particles were PS, Na_2SiO_3 and MFC. By combining PS and heat treatment, we obtained S1 type; by using Na_2SiO_3 we obtained S2 type and with the addition of MFC we obtained S3 type particles. After recognizing that the patch localization clearly for S3 type particles was problematic due to the structural properties of MFC, we decided to decrease the amount of MFC and combine it with Na_2SiO_3 to get S4 type particles. With this combination, obtained particles were more like S1 and S2 type particles with clear separation of the patch. These observations were supported with CMXRF measurements with the opportunity of visualizing the particles up to 30 μm depth. Then S1, S2 and S4 type particles were taken to be used for self-propulsion experiments on 5% H_2O_2 solution. Experiments were recorded by a video camera and the records were analyzed with Image J Software. With the evaluated data we were able to draw trajectories of the particles and calculate instantaneous and average speeds of the particles during their self-propulsion. With

all these data in hand, we could analyze all classes separately and together to find the correlation between the composition and the motion of the particles belonging to different classes. Besides these, we were able to ensure the availability of the particles for multiple self-propulsion experiments by conducting two self-propulsion experiments with same particles. CMXRF measurements before and after self-propulsion experiments prove that the particles are not exposed to be any changes during self-propulsion; therefore, they are reliable to be used for multiple self-propulsion experiments. Lastly, to investigate the effects of the concentration of fuel, 3 identical particles were picked to be put on 0, 5 and 10% H_2O_2 solution and we found out that the particle put on 0% H_2O_2 did not swim at all while the particle put on 10% H_2O_2 was the fastest swimmer as expectedly.

All in all, here we exhibit an accomplished study consists of preparation of anisometric FS-based supraparticles, preparation of FS-based patchy supraparticles with catalytic nanoparticles (Fe_3O_4@Pt), modifications of FS-based patchy supraparticles for the sake of mechanical stability of the particles, self-propulsion experiments of previously modified stable patchy particles and detailed motion analyses of the self-propulsion experiments.

CHAPTER 8: APPENDICES

8.1 Dynamic Light-Scattering Data of FS Suspensions

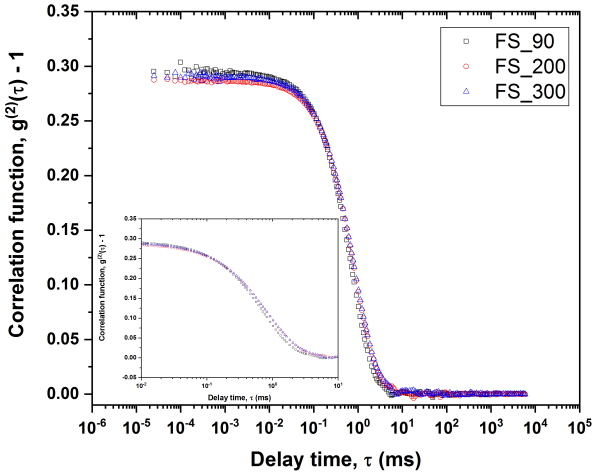

Figure 8.1: Correlation function versus delay time for FS suspensions taken at scattering angle of 90°. [Inset: Zoom into a specific time interval 10^{-2} to 10^{1} ms]

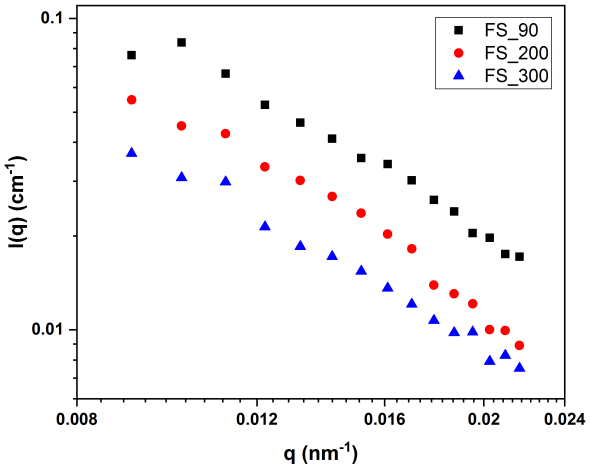

Figure 8.2: Intensity from static light scattering as a function of magnitude of the scattering vector q for FS suspensions

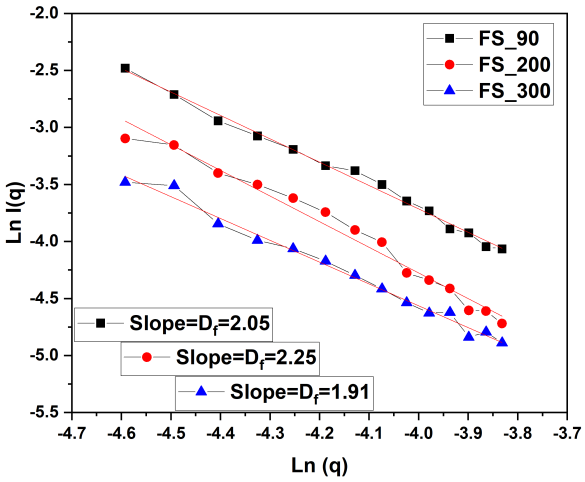

Figure 8.3: Fractal dimensions, D_f obtained from static light scattering data for FS suspensions

8.2 Zeta Potential and Conductivity Measurements of FS Suspensions

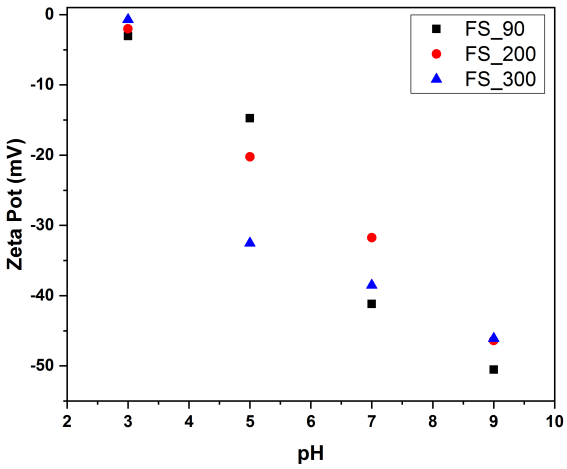

Figure 8.4: Zeta potential measurements of 0.07 % wt/v Fumed Silica suspensions

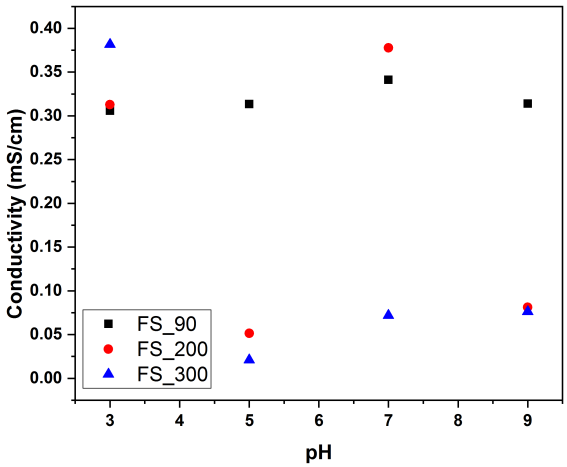

Figure 8.5: Conductivity measurements of 0.07 % wt/v Fumed Silica suspensions

8.3 Anisometry Calculation via CMXRF

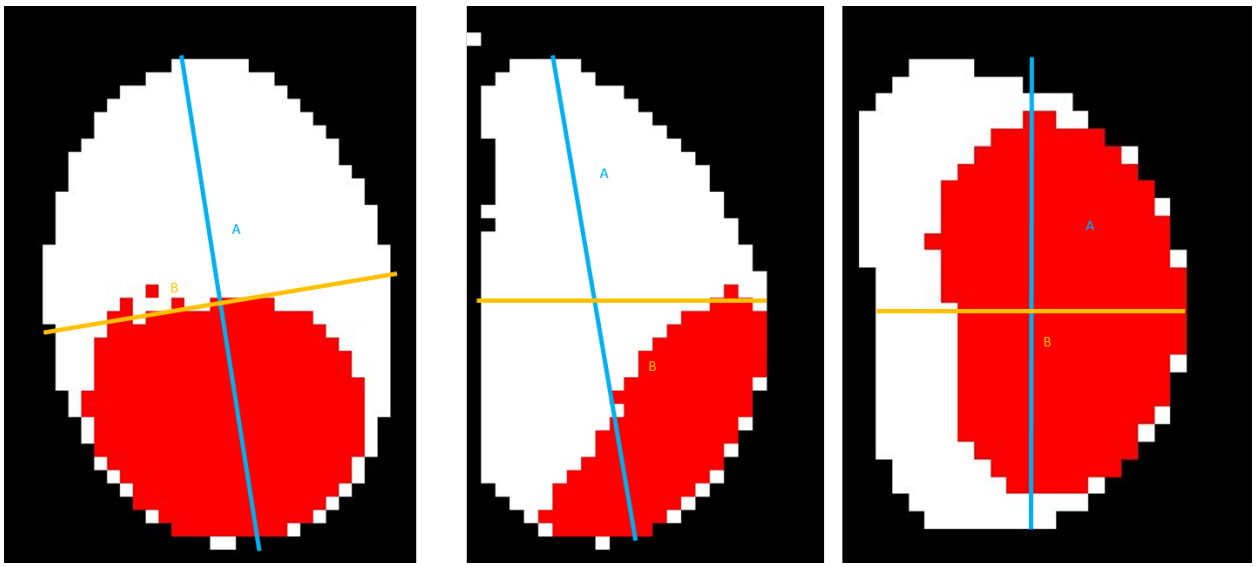

Figure 8.6: xy (left), yz (middle) and xz (right) slice schematics of a particle

Anisometry (A) is calculated as the ratio of A to B. Three anisometry values were calculated for all slices. xy, yz and xz represent length/width, length/height and width/height respectively. Anisometry values were found as A_{xy}=1.3±0.1, A_{yz}=1.9±0.1 and A_{xz}=1.5±0.1. By the definition of anisometry (ratio of length/width), A_{xy} is taken into consideration and anisometry

values calculated by optical microscope and CMXRF were very close to each other and found as 1.4 and 1.3±0.1 respectively.

8.4 TGA Outcome of a Patchy Particle

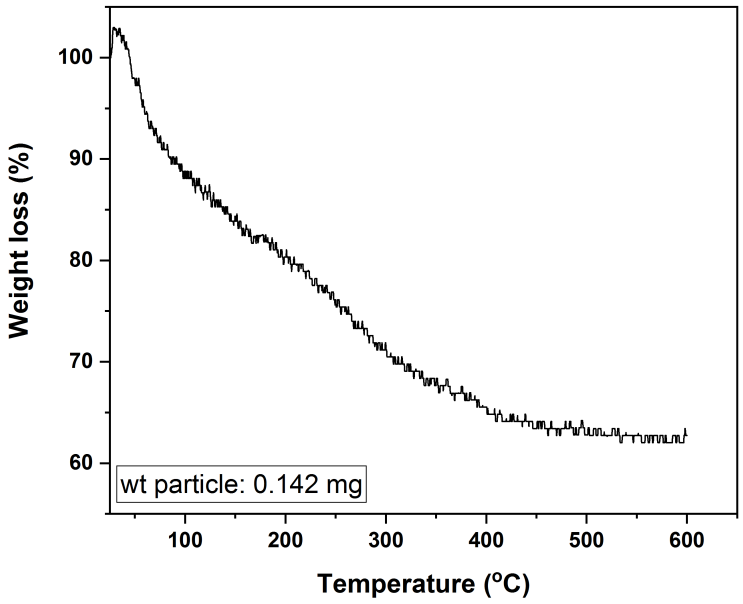

Figure 8.7: TGA outcome of a prepared patchy particle (For the preparation pathway, see Figure 5.1)

A particle, 0.142 mg, was taken for TGA measurement to investigate the evidence of water in the particle after evaporation. Particle was heated up to 600 °C and it lost about 35% in total.

8.5 CMXRF Results Before and After Self-Propulsion Experiment

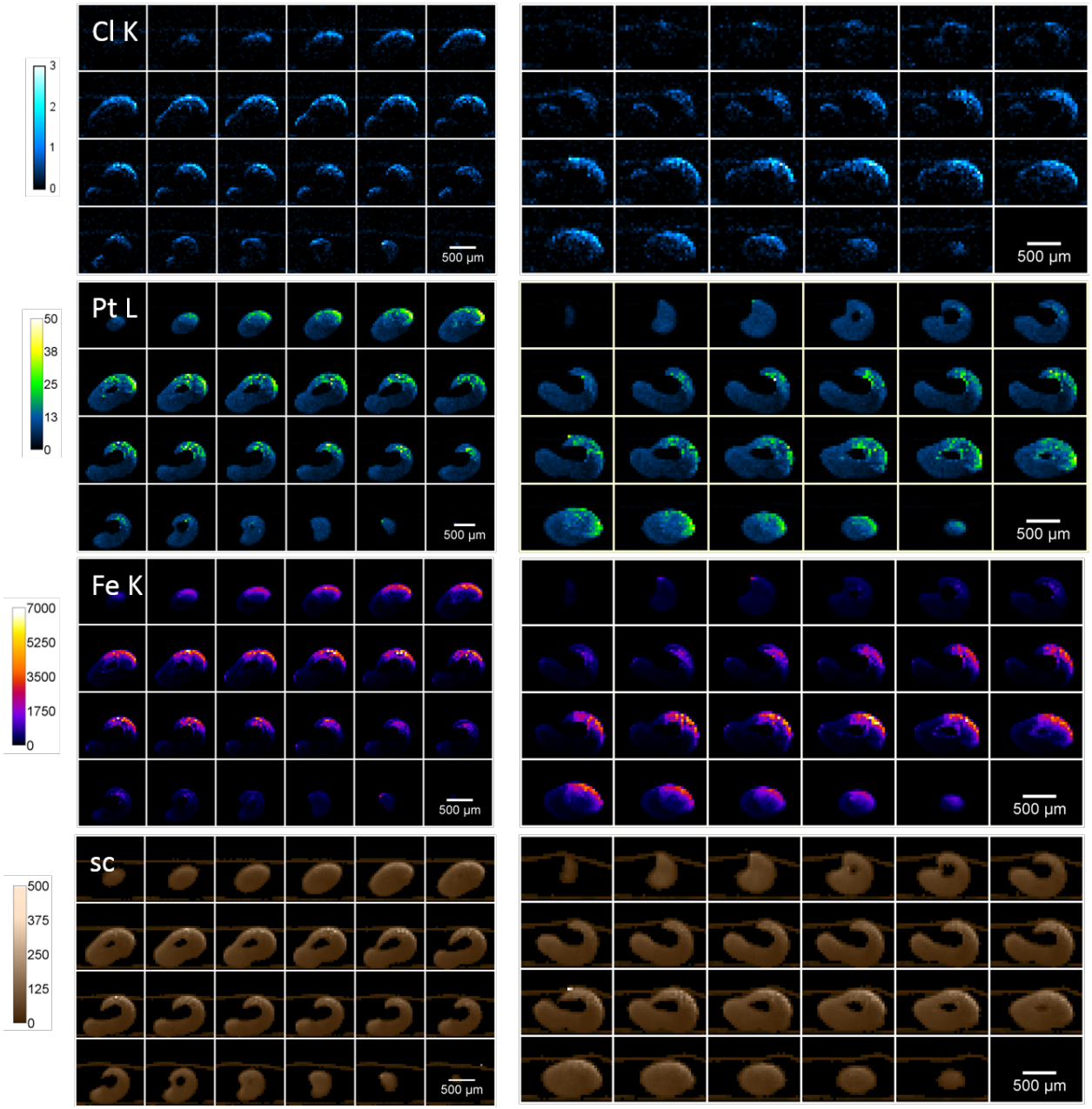

Figure 8.8: Distribution of Cl, Pt, Fe and the whole particle's scattering for Class 1. (Left images: 1st measurement/ before self-propulsion experiment; Right images: 2nd measurement/ after self-propulsion experiment)

8.6 Probability Density Distribution of Speeds of the Patchy Particles

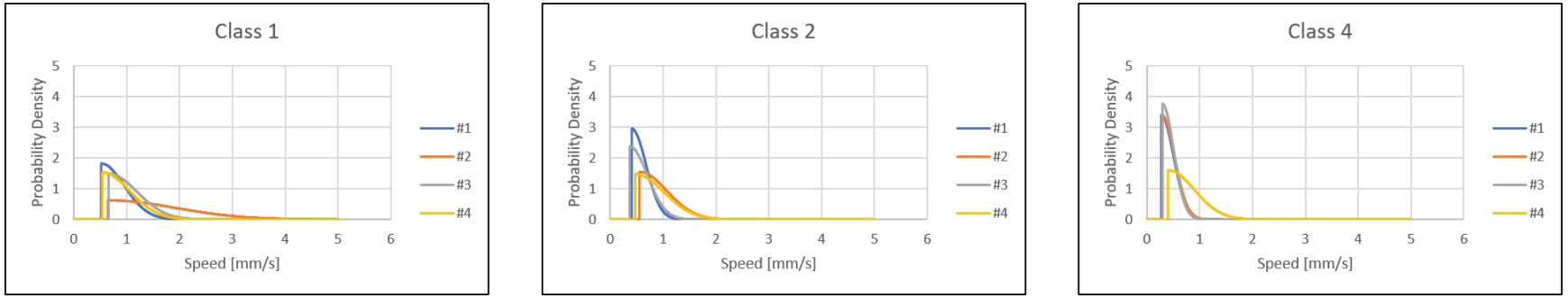

Figure 8.9: Probability density distribution of speeds of the particles from Class 1, Class 2 and Class 4 shown in the subsections 6.3.1.1, 6.3.1.2 and 6.3.1.3, respectively (For the instantaneous average speed distributions of the particles, see Figures 6.2, 6,4 and 6.6).

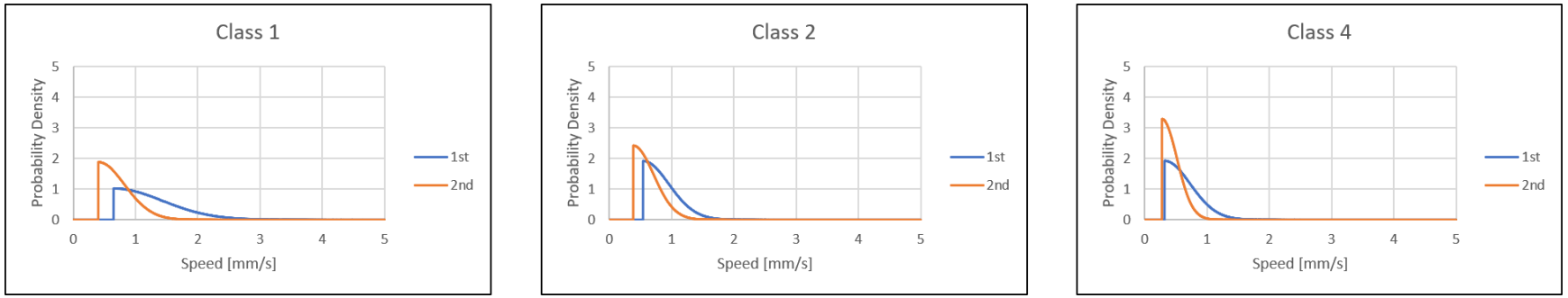

Figure 8.10: Probability density distribution of speeds of the particles from Class 1, Class 2 and Class 4 shown in the subsection 6.3.3 (For the instantaneous average speed distributions of the particles, see Figure 6